Structural study of the auriferous Santoy shear zone, northeastern Glennie domain, Saskatchewan

A Thesis

Submitted to the Faculty of Graduate Studies and Research

In Partial Fulfillment of the Requirements

For the Degree of

Master of Science

in

Geology

University of Regina

By

Chase Robertson Wood

Regina, Saskatchewan

June, 2016

UNIVERSITY OF REGINA

FACULTY OF GRADUATE STUDIES AND RESEARCH

SUPERVISORY AND EXAMINING COMMITTEE

Chase Robertson Wood, candidate for the degree of Master of Science in Geology**,** has presented a thesis titled, ***Structural study of the auriferous Santoy shear zone, northeastern Glennie domain, Saskatchewan,*** in an oral examination held on April 27, 2016. The following committee members have found the thesis acceptable in form and content, and that the candidate demonstrated satisfactory knowledge of the subject material.

External Examiner:	Dr. Mary-Louise Hill, Lakehead University
Supervisor:	Dr. Kathryn Bethune, Department of Geology
Committee Member:	Dr. Guoxiang Chi, Department of Geology
Committee Member:	Dr. Tsilavo Raharimahefa, Department of Geology
Chair of Defense:	Dr. Shaun Fallat, Department of Mathemtaics and Statistics

“Anything I’ve ever done that ultimately was worthwhile… initially scared me to death.”

-Betty Bender

ABSTRACT

The study area lies within the Pine Lake Greenstone belt of the Glennie domain, 125 km northeast of LaRonge, SK. The Santoy shear zone hosts the Santoy 7, Santoy 8/8 East, and "Santoy Gap" gold deposits. This shear zone was studied using a structural and geochronological (ID-TIMS) approach in order to decipher its complex relationship with plutonism, deformation, alteration, and gold mineralization.

Surface and subsurface mapping reveals that the Santoy shear zone, and deposits therein, show a clear structural relationship with the Carruthers Lake synform. The Santoy 7, Santoy "Gap", and Santoy 8 deposits lie along the western limb of this structure while Santoy 8 East has been re-oriented by north-trending, 45°-plunging, S folds. The development of a splay off the D_3 Tabbernor fault, located approximately 8 km east of the deposits, influenced the localization of strain along the western limb of the Carruthers Lake synform. This strain localization, in tandem with elevated fluid pressures, emplaced auriferous fault-fill quartz veins along ore zone parallel dykes during D_3 dextral-reverse oblique slip movement. The age of the Lizard Lake pluton (1874.6 ± 2.9 Ma) and the ore zone adjacent hanging wall dyke (1874.6 ± 1.9 Ma) serves as a maximum mineralization age for these deposits. Structural relationships suggest that the Packman Lake pluton acted as a buttress during D_3 deformation and produced a compressional jog in the Santoy shear zone that may have increased fracture density and fluid flow during mineralization. The age of this intrusion (1807 ± 7 Ma) serves as a maximum age for the development of this flexure. Gold mineralization at Santoy is closely associated with a calc-silicate alteration assemblage. This assemblage formed synchronously with the main stage mineralization event. Titanite and zircon within this

assemblage was dated to 1755.5 ± 8.4 Ma (titanite) and 1754.0 ± 1.8 Ma (zircon) indicating syn-D_3 deposit formation. A beryliferous pegmatite dyke that displays an F_3 axial planar cleavage and crosscuts the auriferous ore lens at Santoy 8A has an age of 1736.1 ± 1.9 Ma. This age represents a minimum mineralization age for this system and a minimum age for regional D_3 deformation in the Glennie domain.

ACKNOWLEDGEMENTS

The National Science and Engineering Research Council, Collaborative Research and Development Grant in partnership with Claude Resources Inc. financially supported this study. I would also like to thank Claude Resources Inc. for providing employment and invaluable work experience during the summers of 2012 and 2013. The exploration and mining staff during this period worked tirelessly to provide training and logistical support for the study and were always around for an evening card game. Special thanks to my field assistants Brandon Bayda, Kevin Schmidt and Jergen Kaminski.

I was very privileged to have many discussions with several members of the Saskatchewan Geological Survey including Dr. Gary Delaney, Dr. Ryan Morrelli, Dr. Ken Ashton and Bernadette Knox, among others during the course of this study. Dr. Mike Hamilton from the university of Toronto spent many late nights by the mass spectrometer collecting geochronological data, which was much appreciated. Brian McEwan donated a lot of his time during the early phases of this study helping me to find my feet and proved a worthy adversary during evening board games. The university of Regina's Faculty of Graduate Studies and Research also provided financial assistance by way of teaching assistantships and Graduate Studies Scholarships and was greatly appreciated.

Finally thank you to Dr. Kathyrn Bethune for her ongoing support during this project. Without Dr. Bethune's encouragement and guidance I would likely have not pursued a Masters Degree and I am grateful for the opportunity she gave me for so many reasons.

TABLE OF CONTENTS

LIST OF TABLES

LIST OF FIGURES

LIST OF APPENDICES

CHAPTER 1

INTRODUCTION

1.1 Geological context and major research questions

The Santoy shear zone is located in the northeastern part of the Glennie domain, 125 km northeast of La Ronge, Saskatchewan and has long been recognized as an important gold-bearing structure within the Pine Lake greenstone belt (Lewry, 1977; Delaney, 1986) (Figure 1.1). The shear zone, situated 16 km east of the main Seabee deposit, hosts the Santoy 8 deposit, the exhausted Santoy 7 deposit, as well as more recently discovered "Santoy Gap" deposit within amphibolite-facies rocks (Figure 1.2).

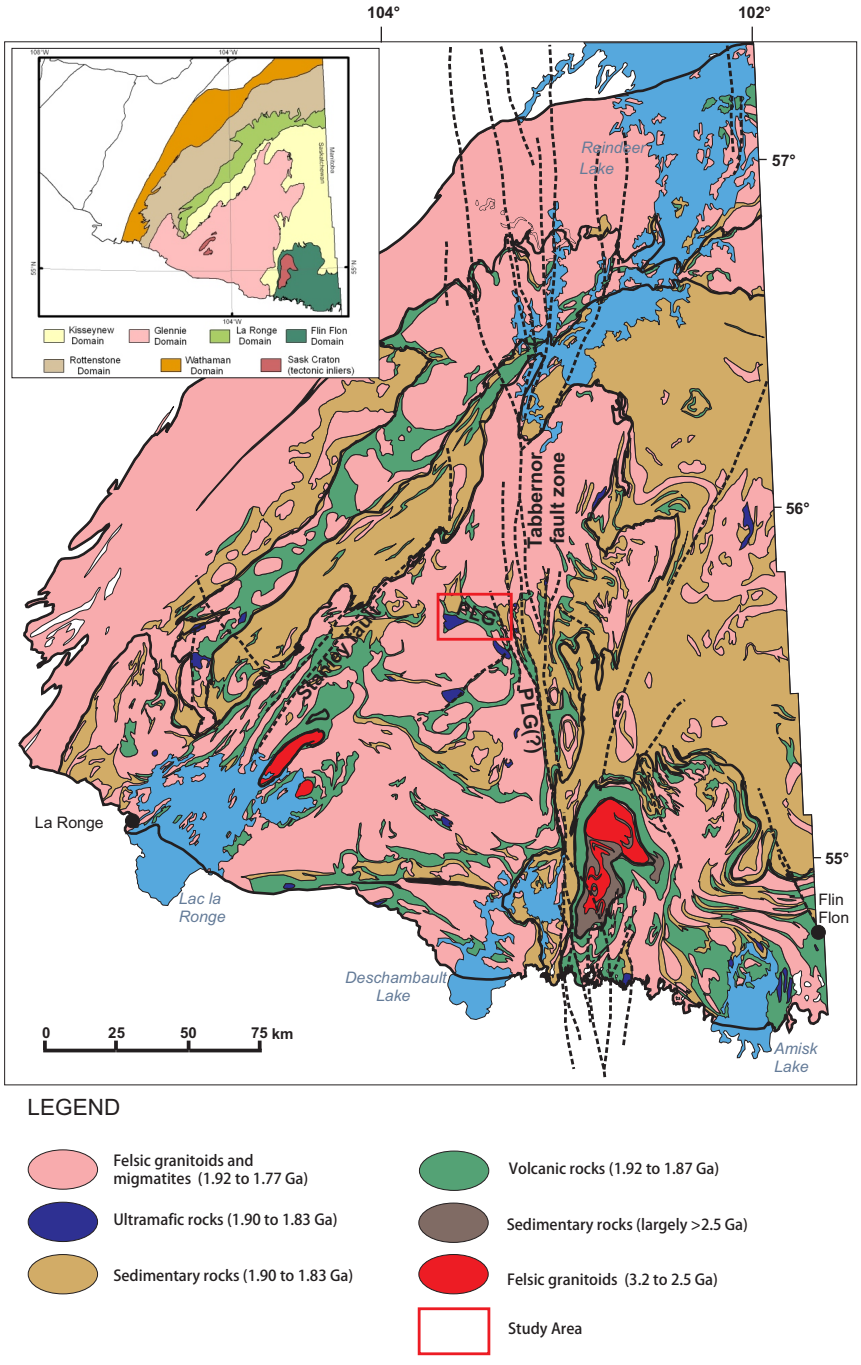

Figure 1.1: Location of the Pine Lake greenstone belt (PLG) within the Glennie domain, northern Saskatchewan. (modified from Morrelli and MacLachlan, 2012; original in colour)

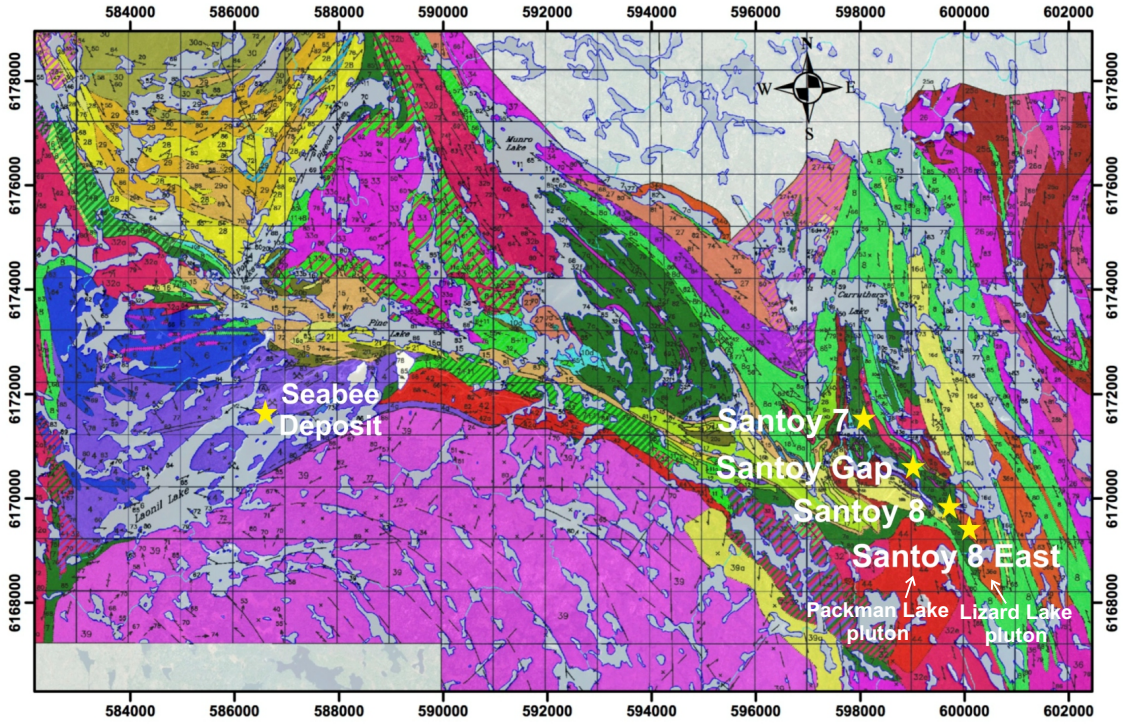

Figure 1.2: Study area and location of Seabee, Santoy 7, Santoy Gap and Santoy 8/8 East gold deposits. (modified from Delaney, 2016; original in colour)

Although the Santoy shear zone has been the target of gold exploration since 1991 (Morrelli and MacLachlan, 2012), the relationships between gold mineralization and deformation are still poorly understood. The recent discovery of the "Santoy Gap" deposit along this auriferous structural trend has renewed interest in this system and access to the Santoy 8 gold mine has provided a window into the Santoy shear zone that was unavailable to previous researchers. In light of this, detailed structural and geochronological analysis was undertaken to constrain regional plutonism and gold mineralization of the Santoy 8 gold deposit. Historically, a large proportion of studies have been directed towards gold deposits in less deformed and metamorphosed greenschist-facies rocks of Archean greenstone belts. Due to this obvious research bias,

many are of the opinion that younger, higher grade rocks are less prospective for large orogenic gold deposits. The study of the Santoy shear zone therefore represents an excellent opportunity to examine the structural evolution of an orogenic gold deposit not only in a higher grade amphibolite-facies terrane, but one which occurs in Paleoproterozoic rocks as well. In doing so, more specific questions that this study will address are as follows:

1: Orogenic gold deposits typically form within active geological terranes that record multiple deformational events (Dubé and Gosselin, 2007). This makes the accurate assessment of the evolution of deposit formation, timing, and kinematics difficult but essential for any gold mining and exploration camp (Robert and Poulsen, 2001). Accordingly, what are the kinematics, structures, and deformational events pertinent to the development and evolution of the Santoy shear zone?

Auriferous quartz veins were first discovered in the Santoy Lake area in 1974, however serious interest in the area did not occur until 1989 when forest fires revealed new outcrop exposure (Delaney and Cutler, 1992). The auriferous Santoy zones, designated zones 1-8 and 8 East, were discovered in 1990-1991 (Delaney and Cutler, 1992). In light of this, a mapping project was initiated to study the regional geology, structure and *P-T-t* history of a 10 km^2 area called the "Santoy Lake gold camp" (Delaney and Cutler, 1992; Durocher, 1997). Details of this study will be described in subsequent chapters where appropriate. The exploration and development history of these zones are available in Morrelli and MacLachlan (2012).

In 2009 – 2011 SRK Consulting (Canada) Ltd. was hired by Claude Resources to develop a geophysical and structural model for the Santoy shear system and surrounding area. The main structural observations that resulted from this work indicated that the Santoy deposits were localized along a compressional jog (left stepping) in a D_3 dextral-reverse shear zone (Figure 1.3).

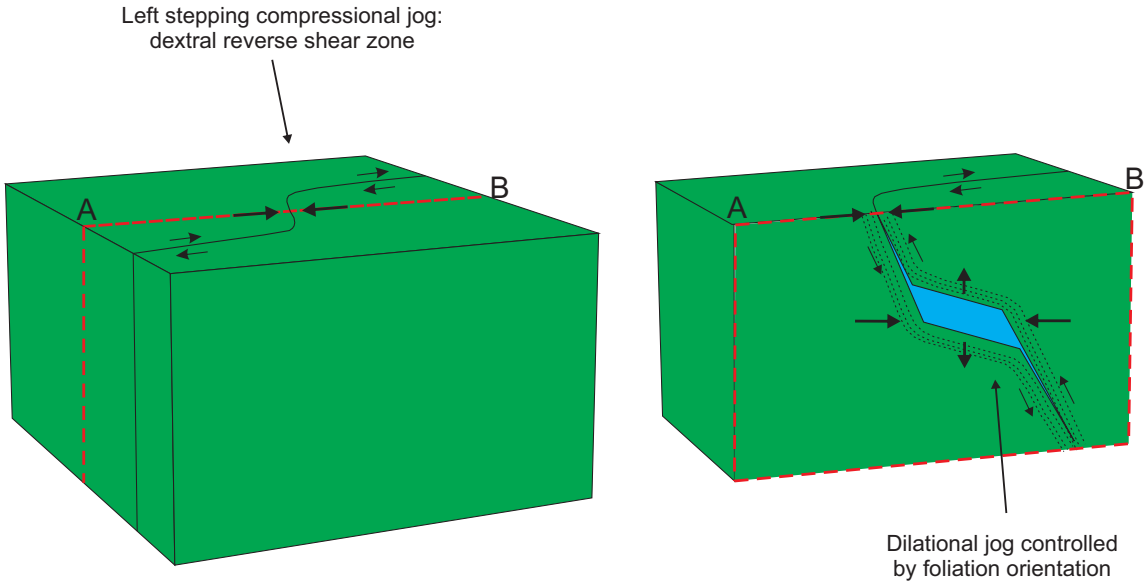

Figure 1.3: Structural relationships in SRK Consulting Ltd. model. A) Compressional jog (left stepping) in a D_3 dextral reverse shear zone. B) Cross section along "A-B" line. Dilation of the shear zone is controlled by dip variation of the foliation. (original in colour)

The individual orebody plunges along this jog were interpreted to vary with steeper ore plunges occurring along the maximum strike curvature of the zone. It was also theorized that Zone 7 formed in a dilational jog created by dip variation within a reverse shear zone, forming a flatter lying orebody, whereas the others were formed in a dextral reverse system forming orebodies that dip more steeply (~60 º) towards ENE. This fluctuation in the foliation dip created the space necessary for auriferous fluids. The high

strain environment in which these deposits were formed was interpreted to have caused fold axis rotation and the occurrence of parallel stretching lineations, fold, and boudin axes. The Individual ore lenses within the Santoy 8A orebody were found to consist of sheeted fault-fill vein networks with felsic dykes and in the hanging wall of the ore zones. Wider auriferous lenses on level plans were associated with a subtle shallowing of the foliation dip to ~45-50º from the average 60º dip. Conversely steeper ~70º foliation dips were associated with narrow and low-grade intervals along the shear zone and "pinching out" of the ore system. Farther southeast within Santoy 8 East, the fault-fill vein network was observed to be folded and, due to the contrasting style of deformation compared to Santoy 8A, was interpreted to have been formed later in the history of the shear zone. Finally late east-west (sinistral) strike-slip brittle faults were observed to affect the internal geometry and continuity of the ore lenses, giving the ore lenses a sigmoidal shape on level plans.

The observations described above served as a very useful starting point for investigating the Santoy 8 mine; however, this study will further investigate, and develop the initial findings of the SRK Consulting (Canada) Ltd. model as well as expand on Delaney and Cutler's (1992) work.

2: Ore zones are localized within and along the contact of amphibolite-grade mafic volcanic rocks and a tonalite-granodiorite pluton hereinafter referred to as the 'Lizard Lake pluton'. Structural relationships also suggest that the Carruthers Lake synform warped around a buttressing quartz syenite pluton ('Packman Lake' pluton) during progressive D_3 deformation. It was deemed important to determine the ages of these intrusions.

In this regard, there is evidence that plutonism in the Glennie domain was episodic. Five main suites have been identified: syn-volcanic, successor arc, late arc, peak metamorphic anatectic melts and syn- to post-tectonic intrusions (Bickford et al., 1987; Van Schmus et al., 1987; Delaney et al., 1988; Chiarenzelli, 1989; McNicoll et al., 1992). U-Pb geochronology was therefore performed on samples of both the Lizard and Packman Lake plutons to better determine their affinity. The age of the former will help constrain the timing of gold mineralization for the Santoy shear system by providing a maximum age. The age of the latter should provide a maximum age for the development of the flexure in the Santoy shear zone.

3: Ore zones within the Santoy system are closely spatially associated with tonalite, diorite, and quartz diorite dykes. Are these dykes and intrusive bodies related genetically and/or temporally? Additionally, are these magmatic events in some way related to the formation of the ore zones?

This close spatial relationship between felsic dykes and auriferous vein systems is also observed in the Seabee gold deposit 16 km to the west. Whereas some early workers viewed the dykes as a 'ground preparation' process by which early, more competent dykes focused strain along their margins (and into surrounding host rocks) during later deformation events (Morrelli and Machlaclan, 2012), others (e.g., Helmstaedt, 1986, 1987; Tourigny et al., 2004) have suggested a close genetic relationship between the dykes, veins, and gold mineralization. It was therefore deemed important to determine the age of the dykes in order to establish their overall position in the structural-tectonic evolution of the region. This age, along with petrography, can then be compared to the age and composition of the peripheral plutons. This data can then be compared to the age

of the alteration package associated with gold mineralization described below to determine whether plutonism, dyke formation, and gold mineralization were synchronous or occurred at various discrete stages over a protracted period of time.

4: What is the age of the alteration package associated with gold mineralization?

Direct age dates for gold metallogenesis in the Glennie domain currently do not exist (Morrelli and MacLachlan, 2012). Schultz (1996) provided an $^{40}Ar/^{39}Ar$ age of 1769 ± 7 Ma and 1728 ± 5 Ma from alteration biotite associated with the shear-hosted Seabee gold deposit. Subsequent researchers (Tourigny et al., 2004) have argued, however, that these ages likely reflect the large amount of time required for the geochronometer to cool below its closure temperature as opposed to a direct mineralization age. Durocher (1997) conducted thermo-barometric calculations to constrain *(P-T-t)* pathways and, on this basis, proposed that gold mineralization in the Santoy Lake region occurred after ca. 1715 Ma. For this reason, mineralization in the study area is currently classified as an episode of renewed or remobilized gold mineralization (Morrelli and MacLachlan, 2012). This interpretation is at odds with the fact that the Santoy deposits (Santoy 7, 8, and Gap) are hosted in ductile shear zones and the 1715 Ma age significantly postdates known ductile deformational events in the Reindeer Zone. Access to the Santoy 8 mine, which was unavailable during Durocher's study, allowed macro-scale observations of ore zones, and drill core, as well as thin section petrography in order to re-evaluate this unique assemblage and its relationship to gold mineralization (Figure 1.4).

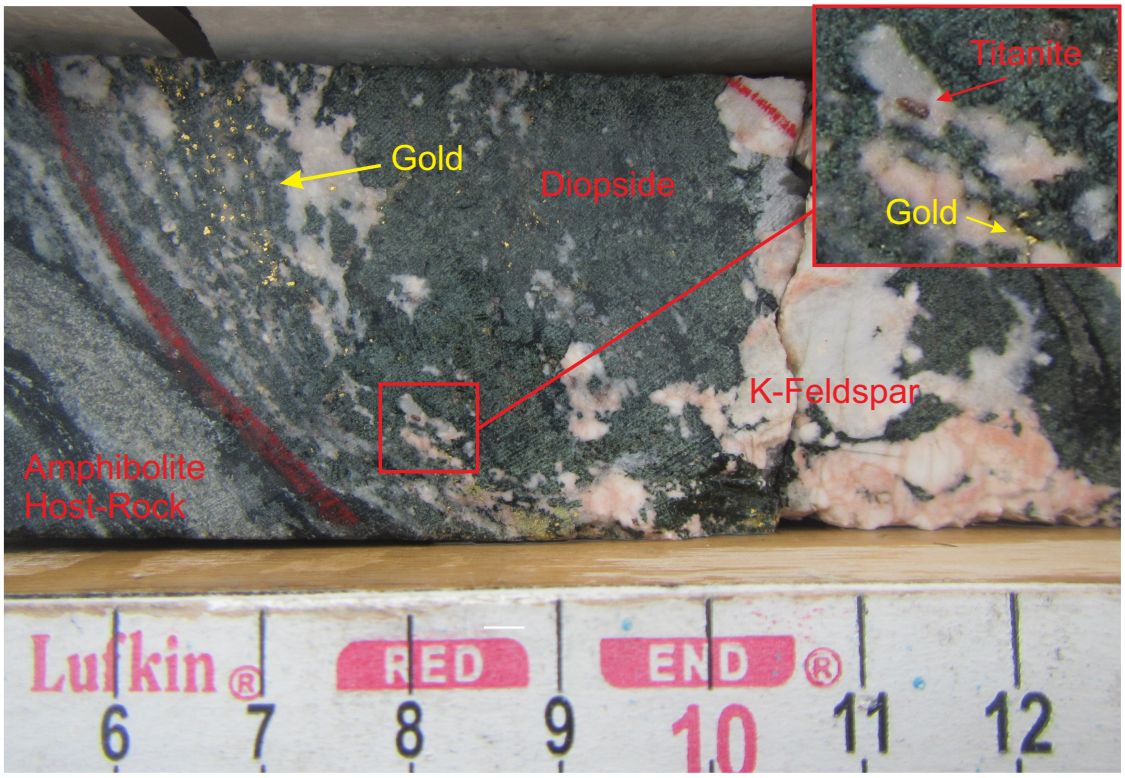

Figure 1.4: High-grade gold mineralization hosted within mafic amphibolite and calc-silicate alteration assemblage. Gold can be seen within K-feldspar and diopside phenocrysts. Upper right — titanite grain enclosed within K-feldspar Santoy Gap drill core (JOY-13-690) at 685m. (original in colour)

5: What is the age of the pegmatites that crosscut Santoy Zone 3 and Zone 8 A?

Elsewhere in the Flin Flon-Glennie complex, the Jan Lake suite of syn-D_3 beryliferous intrusions is thought to mark the end of D_3 deformation. These pegmatites have been dated at approximately 1770-1760 Ma (Chiarenzelli, 1989; Bickford et al., 1992). Durocher et al. (1992, 1993, 1997, 2001) attempted to date one such pegmatite that was interpreted to crosscut (postdate) a D_2 shear zone and pre-date D_3 deformation using the single zircon Pb-evaporation method. The sample yielded four zircon fractions with $^{207}Pb/^{206}Pb$ ages of 2097 ± 117 Ma, 2053 ± 10 Ma, 1815 ± 10 Ma, and 1727 ± 17 Ma. Finally 1815 ± 10 Ma was chosen as the most reasonable age of pegmatite

emplacement as it coincides with peak metamorphism in the Glennie domain. The fact that the zircon crystallization ages were not reproducible, however, suggests that due to inheritance, no one age could be trusted as the emplacement age of the pegmatite (Durocher et al., 2001). In this study, structural relations point to the pegmatites having been emplaced during the latter stages of D_3. A weakly deformed syn-D_3 beryliferous pegmatite that crosscuts the Santoy 8A orebody was chosen for geochronologic analysis in order to place a minimum age on shear zone formation and gold mineralization as well as a minimum age on D_3 deformation in the region.

The answers to these questions will provide more direct geochronological constraints on timing of events, which to date have largely been derived from elsewhere in the Glennie domain. Accordingly, this thesis will provide an updated and coherent structural model for the auriferous Santoy system in order to facilitate future scientific study and guide exploration strategies in the area.

1.2 Field methodology and approach

In the summer of 2012 a 8.5 km^2 area was mapped at 1:2,500 scale by B. McEwan of Claude Resources Inc. in order to provide a solid understanding of the geology along strike, and well outside, the known extent of the Santoy shear zone. As part of this larger mapping effort, more detailed surface and subsurface field investigations for this study were performed over two consecutive summers (2012 and 2013) and were separated into two phases, each with unique challenges.

Phase 1: Surface mapping

Claude Resources Inc. provided transportation to the remote campsite via twin otter aircraft. Once on the mine site, the study area was accessed mainly by vehicle and on foot, but locally by water via motor boat or canoe. Surface investigations employed standard techniques of traversing and outcrop mapping using satellite imagery, GPS, and compasses to aid in navigation. A 0.8 km^2 area situated directly above the operating Santoy 8/8 East mine and along strike of the Santoy Gap, and Santoy 7 deposits was selected for mapping at 1:2,500 scale. Smaller maps and sketches were made in order to highlight the structural characteristics of surface ore zone exposures. Sample collection focused on geochronological and oriented structural-microstructural samples. Several ore zones from the Santoy Gap drill core were also examined and sampled in order to determine if and how this mineralized system compares to other deposits along strike. During this time, as part of a regional prospecting program, excursions were made to different parts of the property in order to ground-truth structural lineaments identified in remotely sensed images as part of Phase 2 (discussed below). The availability of Claude Resources regional maps combined with previous studies (see Chapter 3) provided the opportunity to correlate the broad regional structural evolution of the area to the local surface structure in the vicinity of existing deposits. A solid understanding of the local surface structural control was critical in order to understand the subsurface architecture of the Santoy 8/8 East mine and make predictions for the behaviour of the shear system along its length.

Phase 2: Underground mapping

A main decline ramp provided access to the Santoy 8/8 East mine. Geological mapping on surface can be an arduous activity when faced with less than ideal conditions; however, subsurface geological mapping was by far the most challenging part of this study. The mine was in full operation when subsurface investigation began and documenting important gold-laden structural features had to be done quickly before they were drilled, blasted, and hauled off to the mill (a process which occurs twice daily). In order to speed up this process, existing geological maps created by Claude Resources Inc. mining production staff were employed and supplemented with additional structural measurements and observations. This underground environment requires a high level of spatial awareness to be able to locate yourself in the maze of subsurface ramps and tunnels using the surveyed mine maps. Once a surveyed point was found, a measuring tape was laid down in order to record the locations of structural observations relative to surveyed markers. The most obvious difference between surface and subsurface mapping is the lack of natural light. This affects ones ability to document structural detail and take quality photos i.e., one normally has nothing more than a headlamp and several flashlights. Investigations were also restricted to areas of the mine with access to services such as water, compressed air, and ventilation. The lack thereof rendered parts of this mine inaccessible, no matter how scientifically interesting. Lastly, underground mining is an inherently dangerous activity and requires a high level of situational awareness and specialized training. As such, structural observations, measurements, and samples were taken with safety being the number one priority.

There is, however, one redeeming quality to subsurface mapping and that is that geological structures typically exposed in only two dimensions on the surface can be spectacularly viewed in three dimensions underground.

1.3 Laboratory methods and approaches

After each field season, there was a large amount of structural data and samples that needed to be prepared and analyzed. To do this, laboratory investigations were divided into three main phases.

Phase 1: Compilation

Geological structures can be far too large to properly identify and evaluate when mapping on the scale of individual sills and small surface study areas. To facilitate mapping and structural interpretation at a range of scales, and better understand the overall geological context of the studied deposits, the author designed an ARC GIS database (using ESRI® ArcMap™ version 10.3.1) comprising multiple layers. A high-resolution satellite LANDSAT image as well as orthophotos provided by Claude Resources Ltd. formed the base layer and was complemented by a high-resolution areomagnetic map available from a company survey. Geological maps by Delaney, (2016) and McEwan (2013) were also incorporated as layers for interpretation and comparative purposes. Geosoft Target™ for ArcGIS® was used in order to compile underground geological maps of auriferous vein sets into a three dimensional format. Care was taken to ensure interpretations made from this compilation were then correlated to actual physical structural features observed in the field. All structural data from the Santoy mine area is plotted on equal-area lower hemisphere stereographic plots. Linear

data is presented with a contour interval of 2% per 1% area. Plotting was done using Stereonet version 9.0.1 (Allmendinger et al., 2013; Cardozo and Allmendinger, 2013).

Phase 2: Sample preparation and petrography

Thin section slabs for samples chosen for petrographic analysis were cut at the University of Regina by the author. Samples were oriented in the field with respect to the foliation and stretching lineation. Once in the lab, the samples were cut parallel to the stretching lineation and perpendicular to the foliation, corresponding to the X-Z plane of the strain ellipse. These sections were analysed for strain, microstructure, and kinematic relationships. Samples of alteration and quartz veining associated with gold mineralization, as well as several samples with visible gold were obtained from drill core and underground. These sections were analysed in order to characterize the mineralogical and paragenetic relationships between ore and alteration minerals. In addition to this, thin sections of all samples selected for geochronological study were analysed to determine their mineralogical composition as well as to establish if U-bearing minerals suitable for dating were present. Samples are labelled according to the location (Santoy), year (C12) and sample number (e.g., San C12 056). Samples selected for geochronological analysis are designated with a "GC" (e.g., SAN C12 GC3). Samples collected within the mine are designated by the depth of in meters (multiplied by 10), survey number, and ore lens (e.g., 16L 463 ADR corresponds to 160 m below the surface, in 463, A lens.

Phase 3: Geochronology

Five bulk geochronological samples, of around 25 kg each, were carefully chosen in the field. The samples were sent to the Jack Satterly Geochronology Laboratory at the

University of Toronto. The author assisted with the high precision Chemical Abrasion-Isotopic Dilution-Thermal Ionization Mass Spectoscopy (CA-ID-TIMS) age determinations over a period of two weeks in 2013. The rationale for sample selection and analytical methods used will be discussed in depth in Chapter 7.

1.4 Thesis organisation and structure

This thesis is divided into nine chapters beginning with the preceding introduction to the topic, purpose and methodology of this study. Chapter 2 is an overview of the regional geology of the Reindeer zone. Chapter 3 is a summary of previous work and the local geology of the study area. Chapter 4 presents the regional and local macro-structural controls that define the surface and subsurface structure of the Santoy shear zone and ore bodies within it. Chapter 5 presents the 3-D layout as well as the surface and subsurface structural features of the Santoy 8A and 8 East deposits found during this study. Chapter 6 is concerned with microscopic observations that include the petrological characterization of ore and associated alteration. Chapter 7 discusses the samples, methods, and results of the geochronological analysis. A tectonic synthesis in Chapter 8 deals with the evolution of the Santoy shear zone in relationship to regional tectonics and Chapter 9 further contemplates the main results/conclusions of this study, for example: Were the questions presented at the beginning of the thesis answered? If not, why? What are the outstanding questions pertinent for future research? And finally, what are implications of this study for future gold exploration in the area.

CHAPTER 2

REGIONAL GEOLOGY

2.1 Introduction

As reported in Chapter 1, the Seabee and Santoy gold deposits are located in the northeastern corner of the Glennie domain approximately 125 km northeast of La Ronge, Saskatchewan within the Reindeer zone of the Trans-Hudson orogen. The Trans-Hudson orogen marks the collisional suture zone between the Rae-Hearne, Sask and Superior cratons formed during the closure of the Manikewan Ocean (Stauffer, 1984). A solid understanding of this polydeformed terrane, which contains mixed lithostratigraphic assemblages of different ages preserved in tightly infolded greenstone belt remnants, is critical for deciphering the tectonic history of the Santoy shear zone.

2.2 The Trans-Hudson orogen

The Trans-Hudson orogenic belt can be traced from northern Europe to the southwest into Nunavut and northern Quebec. From there it continues underneath the Hudson Bay basin into Manitoba and Saskatchewan in central Canada (Hoffman, 1988). Using geophysical methods, the Trans-Hudson orogen can be detected in South Dakota, beneath the Phanerozoic rocks of the Williston basin and may extend as far south as the Grand Canyon area (Bickford and Hill, 2007) where it is truncated by the Central Plains orogen (Sims and Peterman, 1986). The Trans-Hudson orogen is generally divided into three distinct zones. They are the Churchill margin, the Superior margin, and the Reindeer zone (Stauffer, 1984). The first two zones are primarily composed of volcanic and sedimentary sequences that were laid down unconformably on the margins of the Archean Churchill and Superior cratons respectively (Ansdell, 2005). The study area

lies within the heart of the Reindeer zone, therefore the following discussion will be focused on this area.

2.3 Evolution of the Reindeer Zone

The Reindeer zone is around 500 km wide and is a geologically complex region that defines the so-called 'internides' of the Trans-Hudson orogen (Figure 2.1). It includes rocks of the Flin Flon-Glennie Complex, Wathaman, Rottenstone, La Ronge and Kisseynew domains and is composed of subduction-generated, primitive to evolved oceanic volcanic rocks, plutonic rocks, interarc and successor arc rocks, as well as marginal-basin sedimentary rocks. These rocks are thought to have been generated within the Manikewan ocean (Stauffer, 1984), that occupied the region between the Rae-Hearne, Sask and Superior cratons ca. 2.07-1.80 Ga (Hoffman, 1988; Ansdell, 2005; Corrigan et al., 2009). Arc volcanic-derived detrital zircons found in the La Ronge and Lynn Lake belts dated at 1.92 Ga provide a minimum age for the initial stage of closure of the Manikewan Ocean (Ansdell, 2005; Corrigan et al., 2005). The closure of this ocean basin ceased around 1.80 Ga (Stauffer, 1984, 1990; Hoffman 1988; Lewry et al. 1990; Syme et al. 1998; Ansdell, 2005; Corrigan et al., 2009). Despite the collision of the Rae-Hearne and Superior cratons, the rocks in this region have been remarkably well preserved because of the intervening Sask craton (Saskatchewan Geological Survey, 2003).

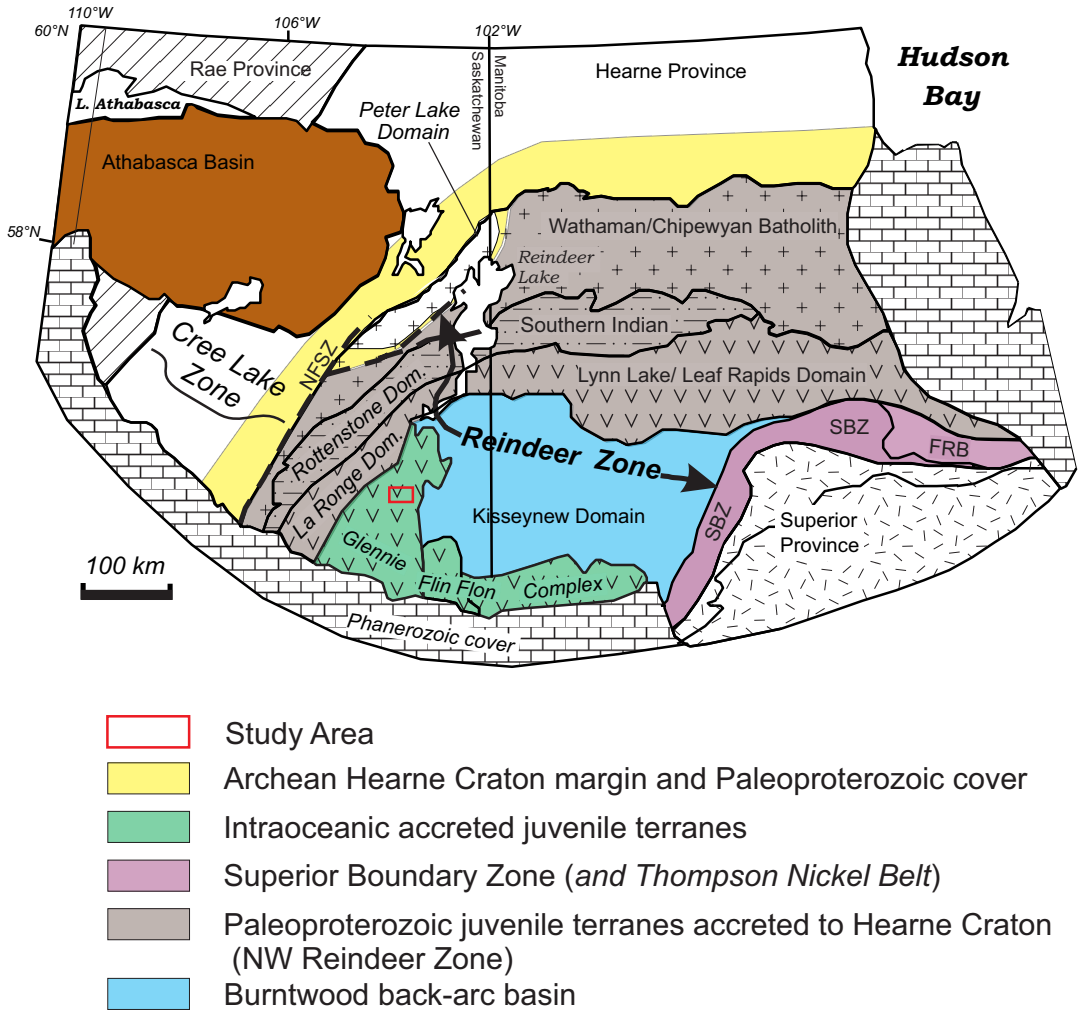

Figure 2.1: The Reindeer zone of the Trans-Hudson orogen in Saskatchewan and Manitoba. (modified from Corrigan et al., 2007; original in colour).

The tectonic evolution of the Reindeer zone can be divided into six major phases beginning with the formation of juvenile volcanic arcs in an oceanic environment and ending with terminal collision of the Superior and Rae-Hearne cratons.

Phase 1: ca. 1.92-1.88 Ga

During the earliest Manikewan ocean phase, juvenile crust of two main types and related assemblages formed. The first assemblage consisted of intraoceanic, primitive, to evolved island arc, ocean crust, ocean plateau, and associated sedimentary rocks as well as syn-volcanic plutonic rocks found in the Flin-Flon and Glennie domains of the southeastern Reindeer zone (e.g., Stauffer, 1984; Syme and Bailes, 1993; Lucas et al., 1996; Ansdell, 2005; Corrigan et al., 2009). The second assemblage consisted of pericratonic ocean arc, back arc, ocean crust and syn-volcanic rocks that comprise the La Ronge-Lynn Lake arc in the La Ronge domain of the northwestern Reindeer zone (Maxeiner et al., 2004; Ansdell, 2005; Corrigan et al., 2005). After their initial formation, these two assemblages of juvenile rocks evolved very differently during the period ca. 1.88-1.865 Ga and, as such, will be discussed separately starting with rocks of the southeastern Reindeer zone.

Phase 2: ca. 1.88-1.865 Ga

The weakly deformed greenschist-facies rocks of the Flin Flon domain in the southeastern Reindeer zone underwent a period of intra-oceanic accretion soon after the initial formation of juvenile crust. This accretion was responsible for the juxtaposition of distinct tectono-stratigraphic assemblages along thrust faults to form the so-called "Amisk Collage" (Lucas et al., 1996). A somewhat older, ca. 1.89 to 1.87 Ga package of predominantly mafic to intermediate volcanic flows with synvolcanic intrusive, sedimentary and felsic volcanic rocks in the Glennie domain, (e.g., older volcanic rock sequences of the Pine Lake, Gee Lake and Brownell greenstone belts) is thought to broadly correlate with the Amisk Group. Rocks of the Flin Flon domain and the more

intensely deformed rocks of the Glennie domain therefore share a similar history and the two are considered to be broadly correlative. Accordingly, rocks of the Amisk collage, the Hanson Lake block and the Glennie domain are collectively referred to as the Flin Flon–Glennie complex (Lucas et al.,1997; Ashton, 1999). U-Pb crystallization ages obtained from plutonic rocks that cut the oldest (juxtaposing) thrust faults indicate that the Flin Flon–Glennie complex formed a single crustal entity by ca. 1.87 Ga (Lucas et al., 1996).

As mentioned above, rocks in the northwestern Reindeer zone record a different history. In this region, early east-dipping subduction led to the accretion of the La Ronge-Lynn Lake arc to the Rae-Hearne craton, contemporaneous with development of a foreland basin in which the upper Wollaston Supergroup was deposited (Tran, 2001; Corrigan et al., 2005). The accretion of this arc complex was followed by a reversal in subduction polarity resulting in west-dipping subduction beneath the Hearne margin. Some researchers (e.g., Tran, 2001) have pointed out, however, that accretion of the La Ronge-Lynn Lake arc to the Hearne craton could have occurred along multiple, west-dipping structures, eliminating the need for a subduction polarity reversal.

Phase 3: ca. 1.865-1.845 Ga

The third phase, lasting about 20 million years, is informally termed the Wathaman Orogeny (Corrigan et al., 2009). During this phase, west-dipping subduction beneath the eastern Hearne margin was responsible for the formation of the Andean-type continental arc, the 1.865-1.855 Ga (Meyer et al., 1992) Wathaman-Chipewyan batholith (Fumerton et. al., 1984) of the Wathaman domain. This batholith broadly marks the suture zone between the Paleoproterozoic rocks of the Reindeer zone and Archean rocks of the

Hearne craton (Saskatchewan Geological Survey, 2003). The end of this period of magmatism is thought to have been caused by the collision of the Flin Flon–Glennie complex with the La Ronge-Lynn Lake arc (Corrigan et al., 2005).

Phase 4: ca. 1.85-1.84 Ga

The collision of the Flin Flon–Glennie complex with the La Ronge-Lynn Lake arc resulted in the deformation responsible for the uplift and subsequent erosion necessary to produce the 1.85-1.84 Ga shallow marine fluvial sandstones of the Ourum, Pine Lake, Missi, and Wapawekka groups in the Flin Flon–Glennie complex, as well as deeper water facies sedimentation of the McLennan Group and Burntwood Group turbidites in a back arc basin within the Kisseynew domain (Ansdell, 1995). The next major phase in the evolution of the Reindeer zone also occurred in this time period, as the Flin Flon–Glennie complex overrode the converging Sask craton. A major basal décollement zone, the Pelican thrust (Sun et al., 1996) and related structures, separate the two juxtaposed terranes (e.g., Lewry and Macdonald, 1988; Ashton et al., 2005). The Sask craton is only exposed in four tectonic windows, across the Reindeer zone but it is interpreted to underlie much of the zone based on aeromagnetic surveys and LITHOPROBE seismic profiles (Lucas *et al*., 1993; Lewry *et al*., 1994; Ansdell, 1995; White et al., 2005).

Phase 5: ca. 1.83-1.80 Ga

The terminal phase in the creation of the Reindeer zone and final configuration of the Trans-Hudson orogen is attributed to the collision between the Superior craton, Reindeer zone, and Rae-Hearne craton. The generation and emplacement of 1.85-1.83 Ga successor arc plutons within the Reindeer zone ceased between 1.83 and 1.825 Ga (Van Schmus et al., 1987) and marked the final stages of closure of the Manikewan Ocean.

This was superseded by widespread deformation and metamorphism (Lewry and Collerson, 1990) that occurred between 1.83 and 1.80 Ga.

Phase 6: ca. 1.770-1.762 Ga

The major orogenic events discussed above were followed by the emplacement of late-to post-tectonic granites and beryliferous pegmatites of the Jan Lake granite suite (Bickford et al., 1987); and have been dated between 1770 and 1762 Ma (Chirenzelli, 1989).

2.4 Structural-tectonic context of the Glennie domain

Lewry (1977) defined three main episodes of deformation and refined the structural understanding of the Glennie domain first described by Padgahm (1966). Subsequent work at the regional scale (Lewry et al.,1990) led to the recognition that the Reindeer zone consists of several km-scale thrust sheets, one of which (the Wapassini sheet) encompasses the northeastern Glennie domain. These thrust sheets, each bounded by a significant high strain zone, were active during regional $D_{1/2}$ deformation facilitating transport of Paleoproterozoic rocks over Archean basement. At the regional scale, D_1 is inferred to have been composite in nature involving two phases of isoclinal recumbent folding (F_1 and F_2) associated with southwest-directed thrusting. However, as discussed in Section 3.3 below, only one major early deformational fabric manifests itself at the local scale; this has resulted in the reassignment of D_2–local (as D_3) and D_3–local (as D_4) (Figure 2.2). The latter terminology (i.e., Lewry et al., 1990) is used throughout the remainder of the thesis.

According to Lewry et al., (1990) and others (e.g., Tran, 2001), D_1 is expressed in the form of tight to isoclinal folds with an associated axial planar schistosity that

parallels bedding. During D_2, this composite $S_{0/1}$ foliation was refolded by tight to isoclinal F_2 folds that transposed primary layering and early D_1 structures into the S_2 foliation plane. D_2 deformation is thought to have taken place from ca. 1840 to ca. 1800 Ma during the convergence of the Hearne, Sask and Superior cratons. Late- to post-collisional D_3 deformation during the ensuing latest stages of shortening formed close to tight, north-trending and west-verging F_3 folds from ca. 1800 to ca. 1770 Ma. Early deformation in the near vertical, north-trending, Tabbernor fault zone was initiated during D_3, and F_2 fold axial planes and D_2 thrust faults were rotated into its shear plane (Saskatchewan Geological Survey, 2003). F_3 sheath-like folds parallel the Tabbernor fault and display curvilinear, fold-axis parallel, stretching lineations (Ashton et al., 2005). Asymmetrical kinematic indicators and down-dip stretching lineations indicate that the latest phase of ductile deformation of the Tabbernor fault zone was high-angle reverse (east side up) (Wilcox, 1990, 1991; Ashton and Balzer, 1995). However, the fault may have undergone earlier displacement inferred to have been normal (east side down), based on more extensive preservation of Ourum Group rocks to the east (Elliot, 1995). A pegmatite dyke that was deformed during the final stages of ductile movement along the Tabbernor fault was dated at 1737 ± 2 Ma and represents a minimum age for (sinistral) movement (Elliot, 1995). It has also been suggested that the Tabbernor fault zone may have been initiated by upper crustal level reactivation of an older Archean structure in the underlying Sask craton (Ashton et al., 2005). Regional F_3 folds were subsequently refolded along upright, northeast-trending F_4 axes during D_4 deformation resulting in the dome-and-basin interference pattern characteristic in this part of the Glennie domain (Lewry, 1977). The D_4 event was caused by post-collisional shortening

between the Rae-Hearne and Superior cratons and is poorly constrained at less than 1770 Ma. Finally, the Tabbernor fault zone was subsequently reactivated during D_4 as a narrow brittle (sinistral strike-slip) fault (Saskatchewan Geological Survey, 2003). Brecciated Phanerozoic rocks imply a minimum 80-km southern extension under Phanerozoic cover and episodic reactivation up to Quaternary time (Byers, 1962; Giroux, 1995). Peak metamorphism in the Glennie domain is thought to occur around 1810 ± 10 Ma and was followed by rapid uplift and cooling at ca. 1770 Ma (Schneider et al., 2007).

D_1	D_2 (D_1 Local)	D_3 (D_2 Local)	D_4 (D_3 Local)
Early isoclinal folding of S_0	E-W trending isoclinal folds and thrusts (e.g., Guncoat thrust) Main foliation (composite $S_{0/1/2}$)	N to NW-trending folds (e.g., Carruthers Lake antiform/synform) Initiation of the ductile phase of Tabbernor fault	Upright NE-trending/ plunging folds Late brittle faulting (e.g., brittle reactivation of Tabbernor Fault

Figure 2.2: Summary of regional (in relation to local) events in the Seabee area.

2.5 Plutonism in the Glennie domain

Plutonism in the Glennie domain can be divided in to at least five broad phases, suites A-E (Figure 2.3). Suite A comprises a group of 1.89 to 1.87 syn-volcanic arc-type plutons (Chiarenzelli, 1989). Whereas suite B comprises a group of 1.86 to 1.846 successor arc plutons (Bickford et al.,1987; Delaney et al., 1988; Chiarenzelli, 1989). Suite C comprises of 1.836-1.828 Ga late-arc intrusions and were followed by a phase of ca. 1807 Ma (suite D) crustal melt intrusions formed during peak metamorphism. Finally, suite E is composed of a series of late to post-tectonic granites and pegmatites of the 1770 – 1762 Ma Jan Lake granite suite.

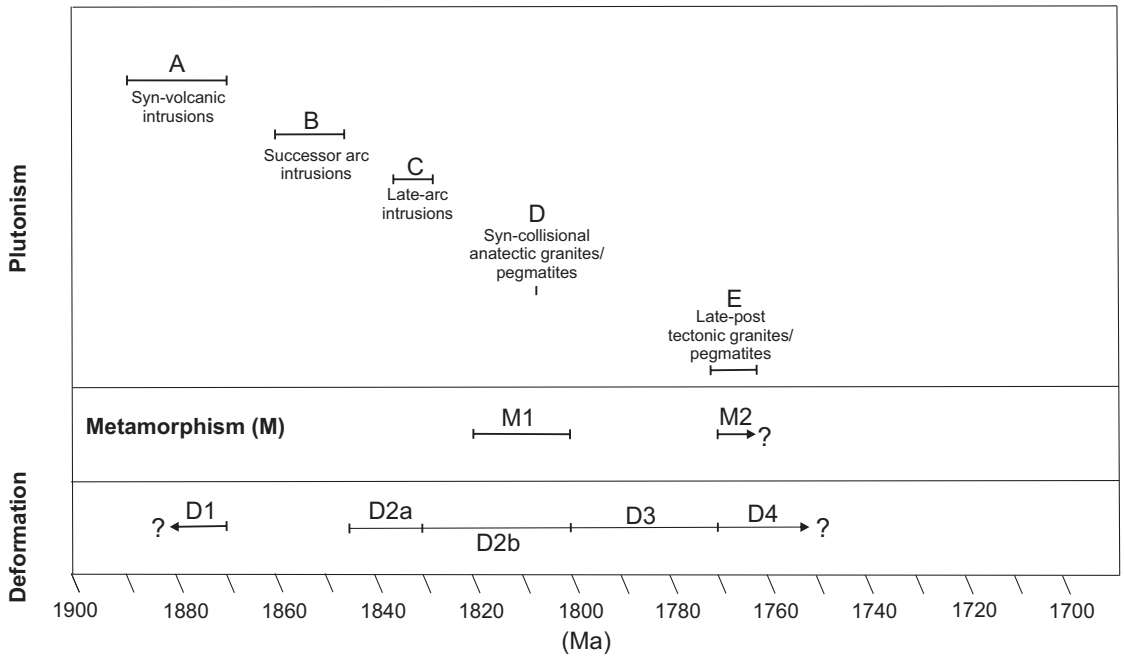

Figure 2.3: Timing of plutonism, metamorphism and deformation in the Glennie domain. Age-ranges for plutonic phases A-E taken from Saskatchewan Geological Survey (2003). Individual ages and associated references are included in Appendix B. Metamorphic ages are reported from Schneider et al. (2007) and Durocher et al. (2001). Deformation ages are reported from Ashton et al. (2005).

CHAPTER 3

LOCAL GEOLOGICAL SETTING

3.1 Introduction

As elucidated by Lewry et al. (1990), the Glennie domain records a complex history of polyphase folding superseded by strain localization, shear zone development, and late-stage brittle faulting. While primary structures are locally preserved, the high levels of strain imparted during the initial stages of deformation (D_1 and D_2) have rendered primary relationships such as bedding or way up indicators difficult to decipher. Gold mineralization within the domain also appears to have occurred at different stages in a variety of structural settings (Morrelli and MacLachlan, 2012).

The purpose of this Chapter is to provide an overview and related analysis of the geology within a 10-16 km radius of Seabee Mine. This will provide the geological context needed in order to accurately evaluate the local structural controls and timing of gold mineralization specific to the Santoy deposits.

3.2 The Seabee area

Work peripheral to the Seabee area of the northeast Glennie domain began as early as 1913 with the reconnaissance investigations of the Churchill River area (McInnes, 1913) and the Pelican Narrows area (Satterly, 1932). Mapping in the Glennie lakes area (NTS 63M-12), encompassing the western part of the Pine Lake greenstone belt, was undertaken in 1970 and 1971 by John F. Lewry (1977). Later, Delaney and Cutler (1992) expanded on Lewry's (1977) earlier work, dividing the rocks of this belt into two major supracrustal assemblages, A and B, and an overlying siliciclastic succession known as the Porky Lake group (Figure 3.1).

A 1:50,000 unpublished compilation map, Map 240 of the Laonil-Uskik Lakes area, (Delaney, 2016) served as a major foundation for the analysis and interpretation of regional geological relationships (Figure 3.2). Assemblage "A" is the older ca. 1.89-1.80 Ga Amisk-equivalent package comprising various mafic-intermediate volcanic and volcaniclastic rocks as well as minor siliciclastics, all metamorphosed to amphibolite facies (Delaney and Cutler, 1992). The 1889 ± 9 Ma Laonil Lake intrusive complex represents the oldest, (Amisk-equivalent) mafic volcano-plutonic package of the Glennie domain (Chiarenzelli, 1989), and consists mainly of gabbro and diorite with subordinate lenses of ultramafic rock, quartz diorite-granodiorite, as well as mafic and intermediate felsic dykes (Lewry, 1977; Delaney, 1986). The 1859 ± 5 Ma granodioritic Eyahpaise Lake pluton intrudes assemblage A (Van Schmus et al., 1987). Assemblage "B" is the younger package of deformed, metamorphosed, and altered volcaniclastic and sedimentary rocks of the Pine Lake group. Major lithological units in this group include felsic volcaniclastics, hornblende volcaniclastics and sediments, lapilli tuffs, and chlorite-actinolite schists as well as a polymictic conglomerate that defines the boundary between assemblages A and B. This conglomerate is intercalated with a rhyolite in the area between Pine and Porky lakes that yielded a U-Pb zircon age of 1838 ± 2 Ma (McNicoll et al., 1992) confirming that assemblage "B" of the Pine Lake group represents the younger ca. 1840 Ma (Missi-equivalent) supracrustal package. Delaney and Cutler (1992) theorized that the epigenetic gold deposits in the region may be localized along this contact due to enhanced fluid flow along the unconformity during deformation (Delaney,1995; Morrelli and MacLachlan, 2012). Rocks in this region were estimated to have reached pressures and temperatures of 500-650º C and 2.5-7 kbar

during D_2 (Durocher, 1997) and 655-705º C and 6.1-7.3 kbar during D_3 (Durocher et al., 2001).

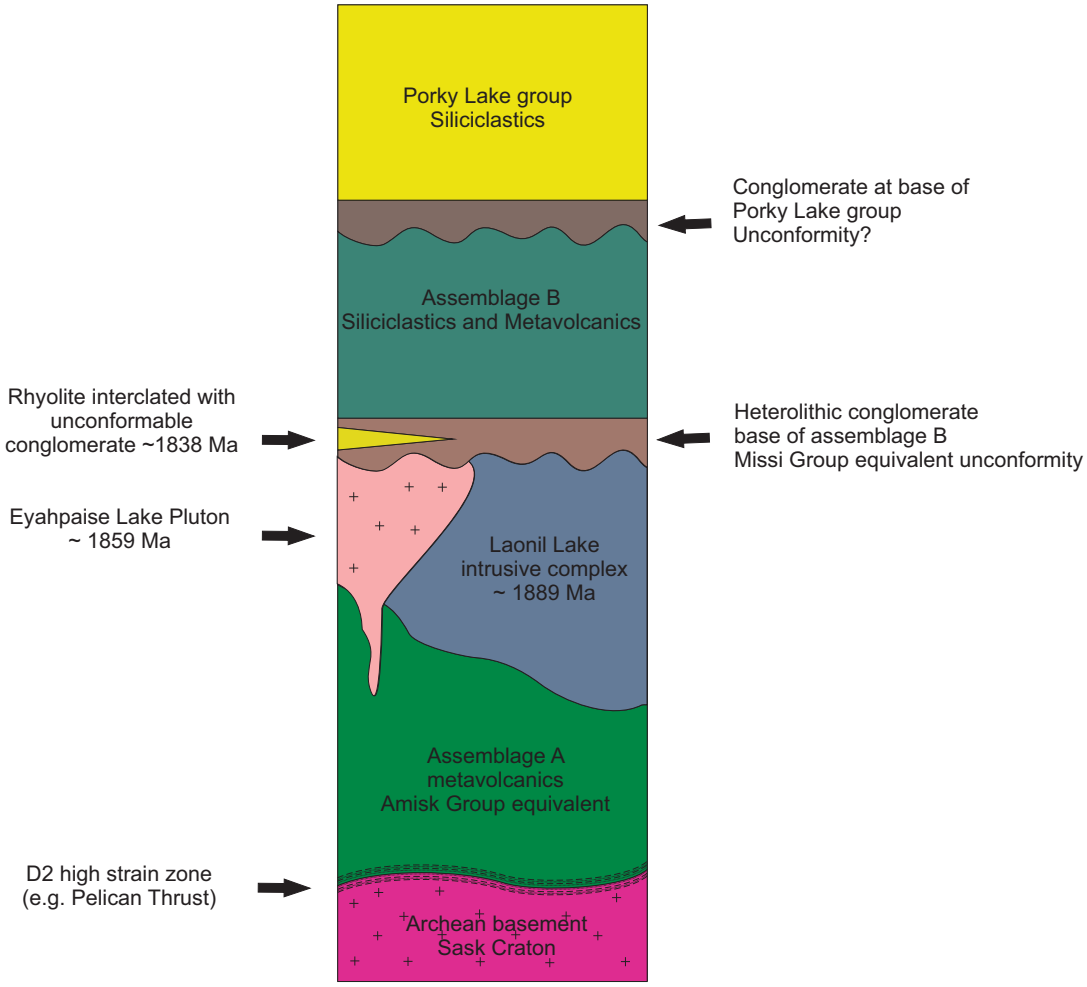

Figure 3.1: Simplified stratigraphy of the Pine Lake greenstone belt. (original in colour)

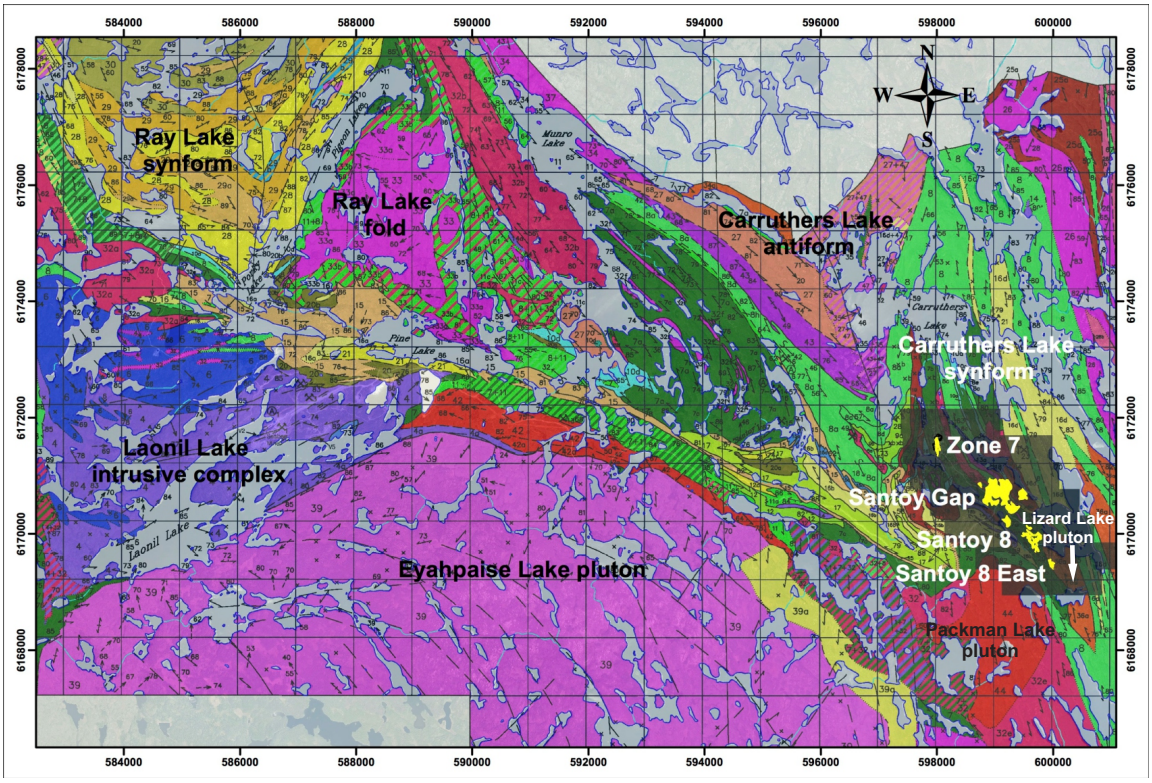

Figure 3.2: Santoy deposits and regional geologic map 240. Geology of the Pine Lake greenstone belt Laonil-Uskik Lakes area (modified from Delaney, 2016; original in colour)

In the northwestern part of the map area (Figure 3.2), the Porky Lake group, exposed mainly in the core of the Ray Lake synform, is fundamentally different in character from the underlying Pine Lake group (Lewry, 1977; Delaney, 1986). Siliciclastic rocks dominate this uppermost assemblage, including micaceous meta-arkose/arenite, meta-greywacke and biotite-rich metapelite. Trough cross-bedded meta-arkose units contain scattered, pebble-sized granitic clasts and in places are associated with thicker units of heterolithic conglomerate (Delaney, 1986). The contact between the Pine Lake group (Assemblage "B") and the basal units of the Porky Lake group is highly strained. The abrupt change in character of the rocks across this contact, and related inferred change in depositional environment (e.g., Lewry, 1977), hints at a

second possible unconformity, albeit highly tectonized/strained. The Sask craton underlies the Glennie domain at depth, based on aeromagnetic surveys and LITHOPROBE seismic profiles (Lucas *et al*., 1993; Lewry *et al*., 1994; White et al., 2005).

3.3 Structural geology of the region

As reported earlier, (Section 2.4) Lewry (1977) recognized three main episodes of deformation in the vicinity of Seabee. Later, when he expanded his work to the regional scale (Lewry et al., 1990), he observed that the earliest identifiable foliation in the Glennie domain, and throughout the Reindeer zone, was actually dual in nature (i.e., D_1 involves two phases of early isoclinal folding, or $D_{1/2}$), based on the local observation of earlier folds. However, early isoclinal folds have never been identified with confidence in the Seabee area (Durocher et al., 2001). Despite this, for the purposes of tectonic correlation, this thesis has adopted the regional hierarchy of Lewry et al. (1990), meaning that the three phases specific to the local area have been re-assigned as D_2, D_3 and D_4 (Figure 2.2).

As is evident on the geologic and aeromagnetic maps (Figures 3.2 and 3.3), the area is dominated by several WNW-trending F_3 folds. From west to east, these are respectively the Ray Lake fold, Carruthers Lake antiform and the Carruthers Lake synform. Locally, these F_3 folds are seen to refold earlier tight to isoclinal F_2 folds and a related strong axial planar foliation (S_2) that parallels bedding. The composite S_0/S_1 foliation is folded into close to tight folds (F_2) with a related axial planar foliation (S_2). The composite $S_0/S_1/S_2$ foliation, effectively a transposition foliation, and narrow high strain zones contained therein dominate the structural fabric of the study area. During

D_3, F_2 folds (and this composite $S_0/S_1/S_2$ transposition foliation) were refolded about NNW-trending axes locally producing type two and three interference patterns (Delaney and Cutler, 1992; cf. Ramsey and Huber, 1987). As elaborated below, the F_3 folds that dominate the map area are generally highly non-cylindrical with curvilinear axial planes and variable plunges. Some of this irregularity may relate to earlier generation folds whereas some of it may be due to superposition of younger (D_4) folds. Interference between NE-trending F_4 folds and NW-trending F_3 folds is thought to have generated the regional dome-and-basin structure of the Glennie domain and greater Reindeer zone (Lewry et al., 1990).

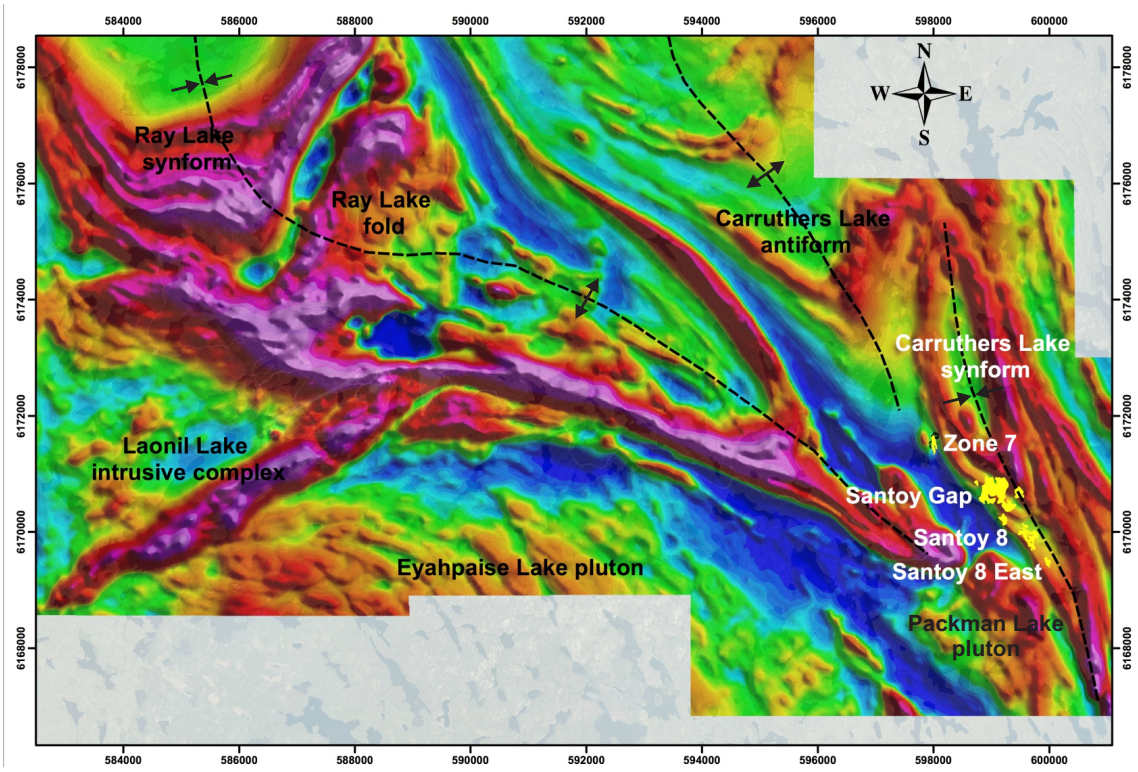

Figure 3.3: Total field regional aeromagnetic map. The magnetic pattern is closely governed by the regional geology and structure of the area (modified from Claude Resources internal report; original in colour).

3.4 D_3 and D_4 folds

The Ray Lake fold was originally named by Johnston (1968) in the Kelly lakes area to the north (Figure 3.3) and was subsequently mapped by Lewry (1977), and Delaney (1986, 1987). According to Lewry (1977), it is a close to tight asymmetrical synform (Ray Lake synform) that plunges approximately 30° to the northeast. At the northern contact of the Porky Lake group, the plunge steepens and is near vertical; however, at the southern boundary of the Porky Lake group, the plunge is 65-70° to the southeast and the fold becomes a steeply plunging antiform (Porky Lake antiform). Lewry (1977) explained the plunge variation in this fold structure to be a function of competency contrast between the Pine Lake metavolcanics and the Porky Lake group. However, Helmstaedt (1986, 1987) suggested that the plunge variation could have been caused by interference between an earlier an F_2 structure and younger F_3 folding. To the south, one can see that the axial plane of the Ray Lake fold, Carruthers Lake antiform and Carruthers Lake synform are remarkably non-planar and are deflected in a consistent manner around the Eyahpaise Lake pluton. Lewry (1977) theorized that the abrupt change in the strike of the axial trace of the Ray Lake fold had been caused by the emplacement of the Eyahpaise pluton to the south, and deflected the F_3 folds as it rose in a diapiric fashion. The emplacement of Eyahpaise pluton however, is now known to predate D_3 deformation by at least 60 Ma (Van Schmus et al., 1987; Ashton et al. 2005). Therefore the Eyahpaise pluton likely behaved as a competent rigid body during a progressive D_3 event whereby the less competent rocks of the Pine Lake greenstone belt, and regional F_3 folds warped around it. This deformation mechanism would have had the potential to influence the orientation and kinematic evolution of any regional

structure that predated or was synchronous with D_3, i.e., (fold axis, fold axial planes, foliations, lineations, shear zones, dykes, veins, and deposits).

To the east, the Ray Lake fold gives way to the Carruthers Lake antiform and Carruthers Lake synform that were originally identified by Budding and Kirkland (1956). The Carruthers Lake antiform is a major SSE-plunging antiform whose minor structures are coaxial with the fold hinge and whose axial trace dies out southwards, as the fold apparently tightens up within the Santoy shear zone.

Delaney and Cutler (1992) examined the Carruthers Lake synform in more detail and determined that it is a moderately plunging, overturned synform with mineral, crenulation, and stretching lineations, all sub-parallel to the fold axis and plunging approximately 45° towards the north (Delaney and Cutler, 1992). Inspection of the Carruthers Lake synform using satellite ortho-images, aeromagnetic data, as well as existing geological maps, however, has revealed that it is structurally more complex than originally described. For example, towards the northern shore of Carruthers Lake, the folding pattern closes off indicating that the Carruthers Lake synform is non-cylindrical (i.e., doubly plunging). A structural basin that lies immediately west of the Carruthers Lake synform (located by an "X" on Figure 4.1) was identified during Delaney and Cutler's (1992) study. It was suggested that this basin was formed by superposition of NNE-trending folds on WNW-trending folds forming a type 1 dome-and-basin interference fold (Ramsay, 1967; Ramsay and Huber, 1987). This interpretation was adopted in the most recent mapping by Claude Resources personnel (B. McEwan, pers.comm., 2013).

It is notable that the D_4 folding event is not well expressed and is only recognized rarely as a weak crenulation of the L_3 lineation about east to NE-trending axes (Delaney and Cutler, 1992). The extent to which both the smaller doubly-plunging synclinal basin resulted from the fold interference proposed above is uncertain and beyond the scope of this thesis.

3.5 D_3 high-strain zones

A number of curvilinear NNW-trending, high-strain zones transect the area, enveloping the major D_3 folds. These zones curve southwards into parallelism with the Tabbernor fault zone immediately to the east. The Santoy shear zone represents one of these structures; it is at least 3.5 km long, extending from from Zone 7 in the northwest to Zone 8 East in the southeast, and is localized along the western limb of the Carruthers Lake synform. The moderately strained western limb of the Carruthers Lake synform is approximately 500 m wide while the mineralized zones themselves occur in discrete highly strained zones which are approximately 1.5 to 15 meters wide. It has been proposed that several of these NW-trending high-strain zones may represent reactivated D_2 structures (Delaney and Cutler, 1992). The region is also crosscut by late-D_3 vertical to steeply dipping E-trending extension joints and conjugate fractures mantled by alteration halos (Delaney and Cutler, 1992). More specific attributes of the Santoy shear zone and its related gold deposits are discussed in the next chapter.

CHAPTER 4

GENERAL CONTEXT OF THE SANTOY 8 DEPOSITS

4.1 Introduction

As reported in the previous chapter, the Santoy shear zone is located within a ~500m wide structural corridor that extends at least 3.5 km from Zone 7 in the northwest to Zone 8 East in the southeast along the western limb of the Caruthers Lake synform (Figure 4.1). The actual limits/widths of the 'shear zone' are not that well defined, but marked by a gradual increase in intensity of the $S_{2/3}$ composite foliation and change in habit of quartz veins that occur in 1.5 to 15 m wide sheet-like lenses. The shear zone hosts the Santoy Zone 7, Santoy Gap, and Santoy 8A/8 East gold deposits, however the current study involved a combination of surface and subsurface geological mapping that was focused primarily on the Santoy 8A and 8 East gold deposits in the south.

4.2 Geology in vicinity of the Santoy 8 deposits

At the outset of this project, a 0.8 km^2 area encompassing the southern extent of the Santoy shear zone, and Santoy 8/8 East deposits was mapped at 1:2,500 scale (Figure 4.2). The area is situated directly above the Santoy 8/8 East and along strike of the Santoy Gap, and Santoy 7 deposits. The western part of the area is underlain by mafic volcanic-derived amphibolite, which is in contact with the Lizard Lake tonalite to the east. The contact is gradational with numerous sheets and dykes of tonalitic-dioritic composition injected into the amphibolitized mafic volcanic rocks and all variably affected by high strain.

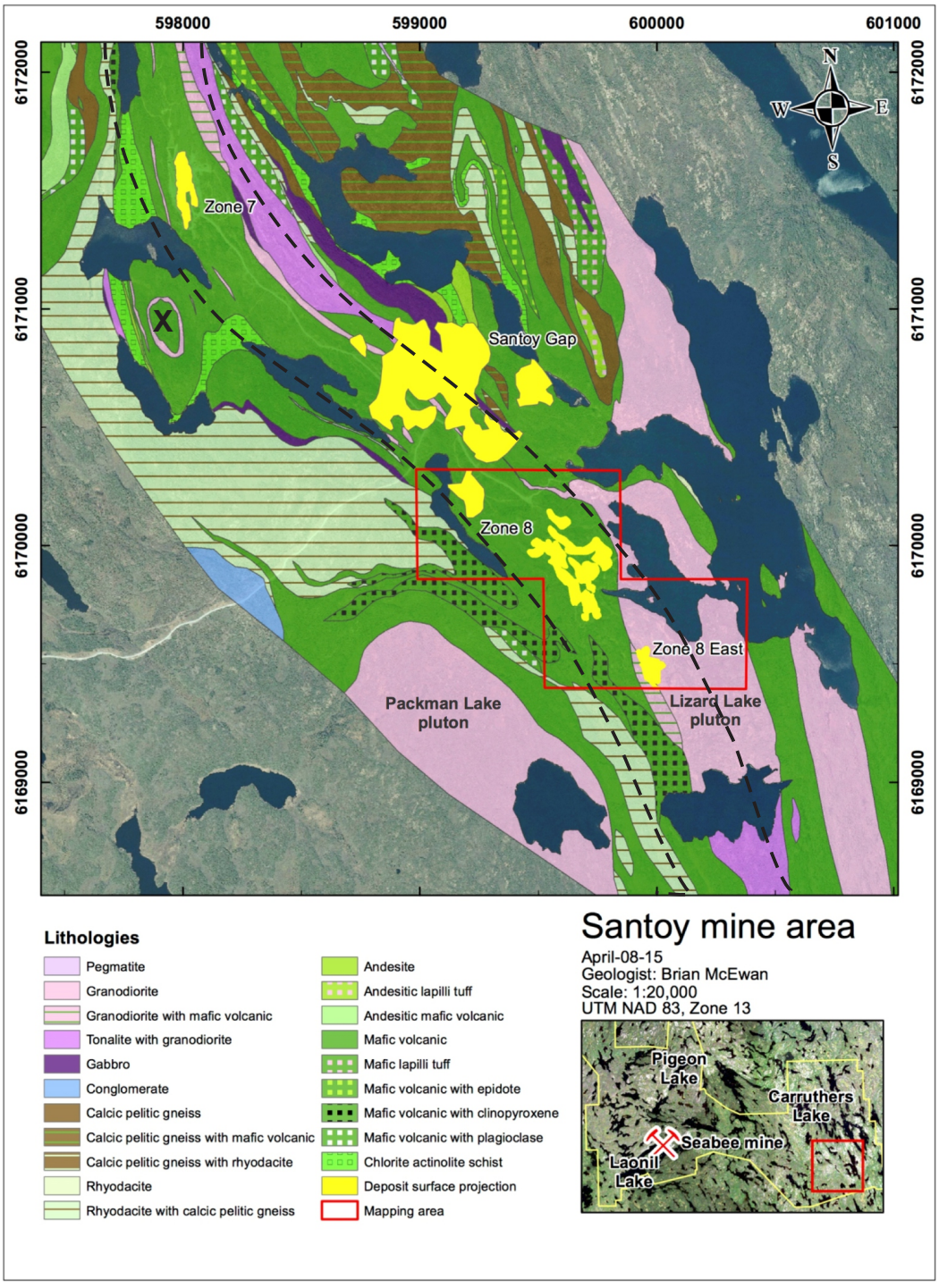

Figure 4.1: Location of 0.8 km^2 map area encompassing the Santoy 8 and 8 East deposits. "X" indicates location of synclinal basin identified by Delaney and Cutler (1992). Dashed lines indicate approximate limits of the Santoy shear zone. The larger map area is also located in the shaded area of Figure 3.2 (modified from McEwan, 2013; original in colour).

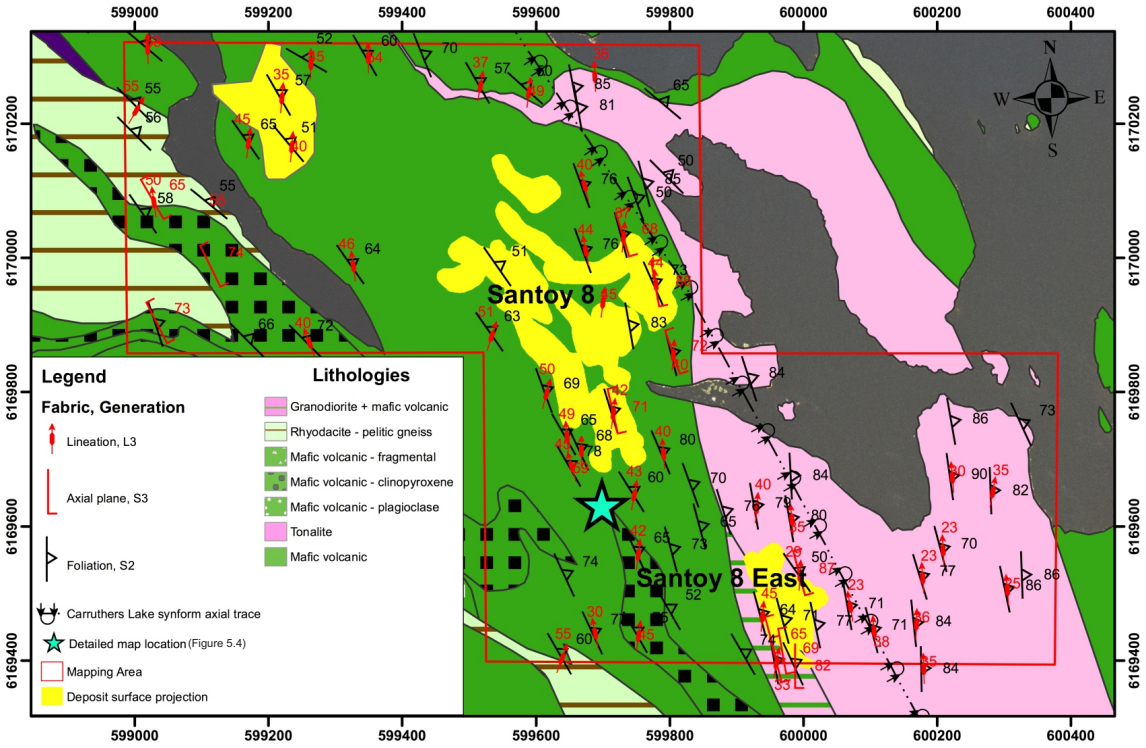

Figure 4.2: 1:2,500 scale geological map of study area. (original in colour)

4.2.1 Mafic volcanic rocks

Amphibolite-grade Assemblage A mafic volcanic rocks dominate the outcrop area in the vicinity of the deposits. Their weathered surfaces are a dark grey-green colour, whereas their fresh surfaces are green-black with a colour index of 40-50. They are typically fine to medium grained and very well foliated, corresponding to S > L tectonites; hornblende, plagioclase, and lesser biotite define the main (S_2) foliation. Very rare primary structures are evident (pillow structures). Plagioclase commonly forms mm-scale porphyroblasts giving the rock a spotted "salt and pepper" appearance.

4.2.2 Lizard Lake (tonalite) pluton

The southernmost known extent of the Santoy shear system and Santoy 8 East orebody occurs adjacent to the folded contact between a unit of fine- to medium-grained, tonalite-granodiorite and mafic volcanic-derived amphibolite of Assemblage A. This body, is approximately 2.5 km long, 0.5 km wide and is very well exposed in outcrop. It also contains xenoliths of the mafic amphibolite indicating that it post-dates emplacement of mafic volcanic rocks. Like the amphibolite, it also contains deformed, rusty-coloured quartz veins and calc-silicate style alteration typical of the Santoy 8 East deposit (see Section 6.2), indicating that both units predate gold mineralization.

In keeping with its attenuated, northeast-elongate shape, the pluton is strongly deformed at the mesoscopic scale, corresponding to an S > L tectonite, with biotite and hornblende defining the main (S_2) foliation; S_2 is folded and quartz and plagioclase define a strong fold-axis parallel L_3 stretching lineation (Figure 4.3A). In outcrop it displays grey-buff weathered surfaces, whereas fresh surfaces are light pink. Although it was initially mapped as a granodiorite (potentially transitional to tonalite), petrographic observation of thin sections confirm a tonalitic composition characterized by approximately 55% plagioclase feldspar, 20% quartz, 15% hornblende, 6% biotite with accessory apatite, monazite, and zircon with quite variable proportions of hornblende and biotite (Figure 4.3B). Plagioclase is commonly altered to sericite and forms myrmekitic intergrowths with quartz; it also commonly displays tapered mechanical twins, as an effect of deformation. Quartz displays serrated to rounded grain boundaries with undulatory extinction and the formation of subgrains.

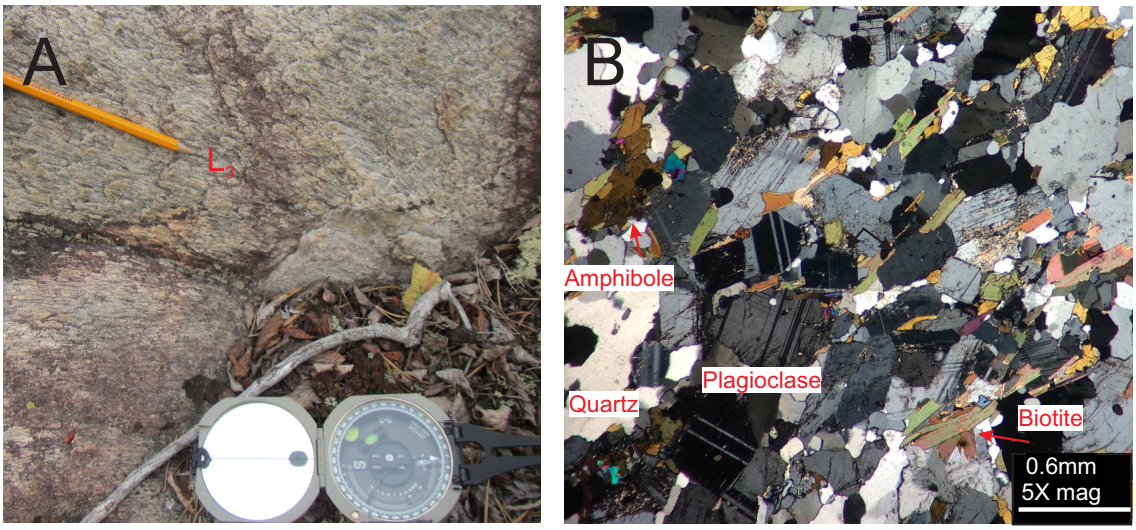

Figure 4.3: Structural and petrographic features of the Lizard Lake pluton. A) Typical L_3 Stretching lineation defined by elongate quartz and feldspar and alignment of hornblende. B) Photomicrograph under crossed polarized light of representative sample of the Lizard Lake pluton. (original in colour)

4.2.3 Santoy dykes

Dykes ranging in composition from tonalite to diorite were mapped on the surface where they clearly intrude and therefore post-date the mafic volcanic rocks of Assemblage A. They are highly strained with a strong internal foliation and their long dimensions parallel to the main S_2 foliation. Petrographic study suggests there are at least three types of dykes that range in composition from tonalite to quartz diorite and diorite (Appendix A). The only notable exception to this is of a suite of beryliferous granitic pegmatite dykes that commonly crosscut the main S_2 foliation and are gently folded (F_3) with a weak S_3 axial planar cleavage (see sections 5.3.1 and 7.2). In Delaney and Cutler's (1992) study of the Santoy lake gold camp, more than 40 of these beryliferous pegmatites were identified, two of which were mapped in detail and geochemically studied for their rare earth element potential (Williams et al., 1992).

4.3 Structural geology

As elsewhere in the Seabee area, all rocks carry a strong S_2 foliation that dips moderately-steeply to the northeast and is folded about NNW-trending close to open (F_3) folds. Evidence for the D_1 deformation event was not recognised in the map area. In Figure 4.4, poles to the main foliation (S_2) in the region are plotted stereographically and define a common great circle, demonstrating that the S_2 foliation is folded around a common axis of ~45→000º, inferred to represent the F_3 fold axis. The poles are distributed asymmetrically, which indicates both fold limbs dip towards the northeast. Stretching lineations, crenulation lineations, mineral lineations and fold axes are all co-axial and correspond to the F_3 fold axis.

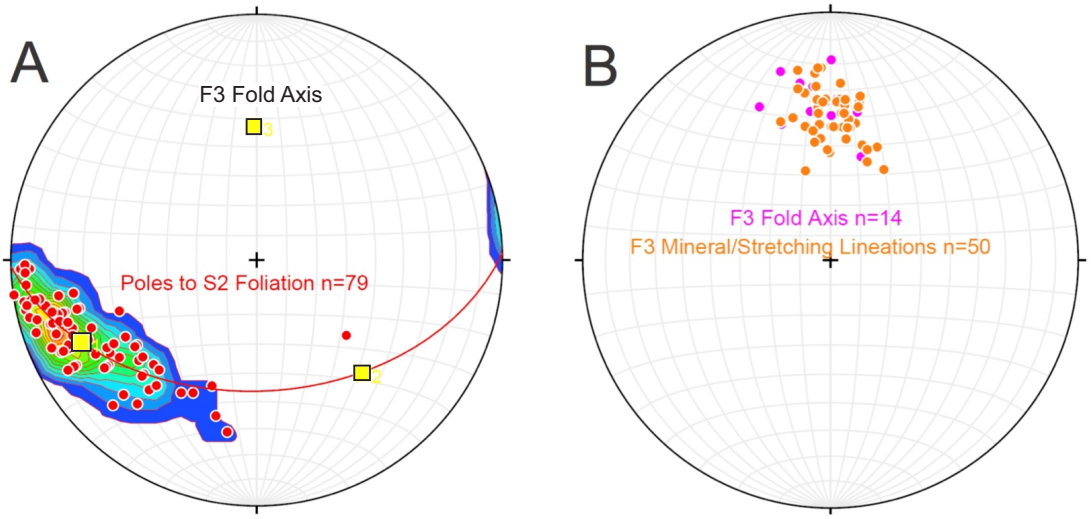

Figure 4.4: Structural data in the Santoy mine area. A) π-Pole plot of the poles to the S_2 foliation define a great circle, the pole to this defines the F_3 fold axis of the Carruthers Lake synform in the south (~45→000º). The S_2 poles are asymmetrically distributed indicating that both fold limbs dip toward the east. B) All linear structural features coincide with the F_3 fold axis in this area. (original in colour)

This relationship genetically links these linear fabrics with the F_3 folding event and defines the plunge of the southern part of the Carruthers Lake synform. In addition, based on several brief excursions outside the map area it was determined that this fold plunges approximately 57→136° in the north (Figure 4.5), confirming its doubly plunging, non-cylindrical nature.

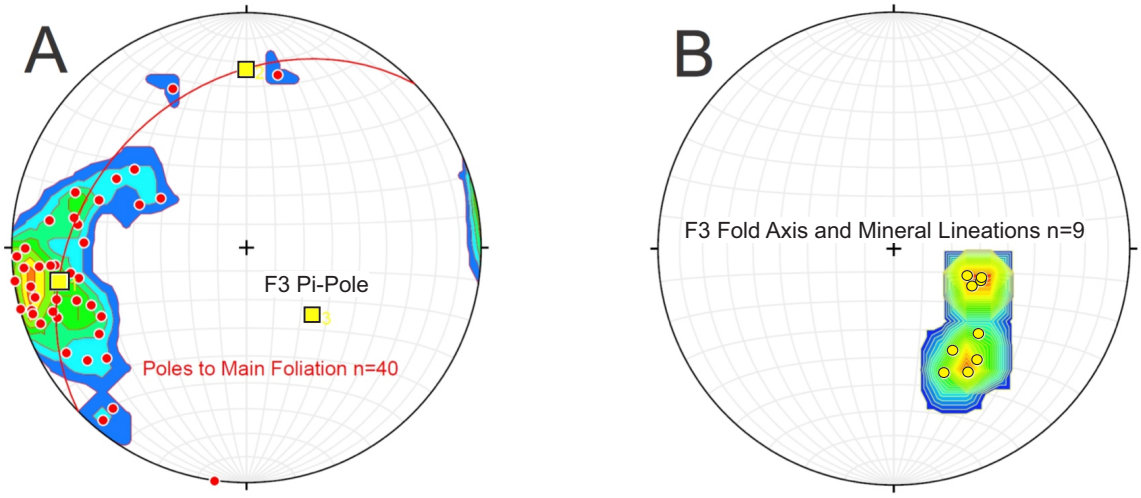

Figure 4.5: π-Pole plot of the northern portion of the Carruthers Lake synform. A) Contoured π-Pole plot that defines the F_3 fold axis of the Carruthers Lake synform in the North (~57→136°). B) All linear structural features coincide with the F_3 fold axis in this area. (original in colour)

The D_4 deformational event in this map area was not recognized in the 0.8 km^2 map area. However regionally it is thought to correspond to upright NE – SW trending folds with wavelengths spanning tens of kilometres and interference related to this superposed folding may be responsible for reversals in plunge of F_3 fold axes (Lewry et al., 1990, Maxeiner and Normand, 2009).

4.3.1 Nature of the Santoy 'shear zone'

The actual limits of the Santoy shear zone are poorly defined, being marked by a gradual increase in intensity of the regional S_2 foliation that has been overprinted by, and transposed into parallelism with S_3 along the western limb of the Carruthers Lake synform. In tandem with this, there is a dramatic change in habit of quartz veins, with openly folded quartz veins crosscutting the foliation outside the zone giving way to abundant lit-par-lit veins within the zone. This change in the character of quartz veins is also accompanied by evidence of extreme flattening in the form of boudinage perpendicular to the L_3 lineation. This S_3 'shear foliation' is a composite feature produced by flattening and transposition of the regional S_2 foliation along this limb of the fold during D_3 deformation/shearing. The north-plunging lineation within this zone also appears to be genetically linked to the regional D_3 event. The bulk kinematic framework and related progressive evolution of these structures will be discussed after reporting the layout and details of deposit scale geology in the next chapter.

CHAPTER 5

3-D LAYOUT & SURFACE/SUBSURFACE FEATURES OF THE SANTOY 8 DEPOSITS

5.1 Introduction

In order to gain a fuller perspective of the Santoy 8 deposits, the mapping conducted within the southern part of the Santoy shear zone reported in Chapter four was complemented by construction of a 3-D model. Along with this, outcrop-scale surface, and subsurface investigation was undertaken in deposits 8A and 8 East. This allowed the documentation of macroscopic to microscopic features such as lithologies, structures, alteration, and related kinematic indicators.

5.2 General deposit layout and 3-D modelling

The first step in 3-D modelling involved compiling existing level plan maps created by Claude Resources Inc. mine geologists. A typical example of these maps is shown in Figure 5.1 and includes auriferous quartz veins and dykes that serve as a proxy for the subsurface and surface location of the Santoy shear. These 1:250 scale maps of auriferous vein sets were digitized and georeferenced using ESRI® ArcMap™ version 10.3.1. A z-axis coordinate corresponding to the depth in meters below the surface was then subsequently assigned using Geosoft Target™ for ArcGIS® in order to view auriferous vein sets in a three dimensional framework (Figure 5.2). This exercise revealed that the surface expression of the Santoy 8A ore lens is continuous at depth and the subsurface expression of the Santoy 8A ore lens is structurally remarkably uniform in the vertical dimension. This is important because it meant that additional structural mapping and measurements could be made with a focus on the structural changes in the orebody along its strike in a horizontal plane. In the Figure 5.2, changes along the 8A

orebody in a horizontal plane suggest that the deposit has been gently folded/warped as expressed by a slight "S" shaped curvature. In zone 8 East, the structure of the deposit is more irregular again, likely due to the influence of folding.

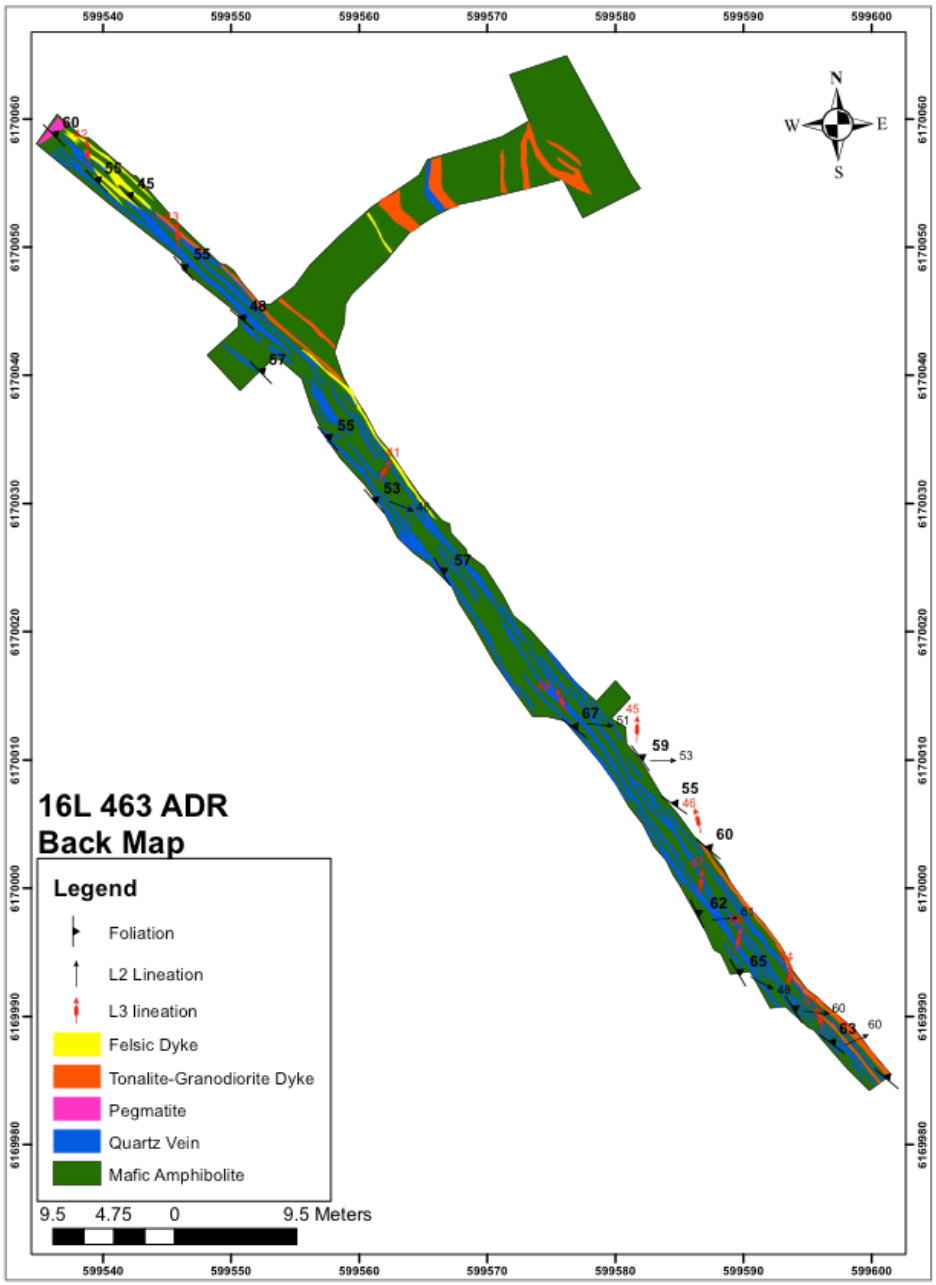

Figure 5.1: Geological level plan map of 16L 463 ADR Santoy 8A. The original was created by Claude Resources Inc. mine geologists. This map was georeferenced, digitized, and augmented with additional structural measurements by the author. (original in colour)

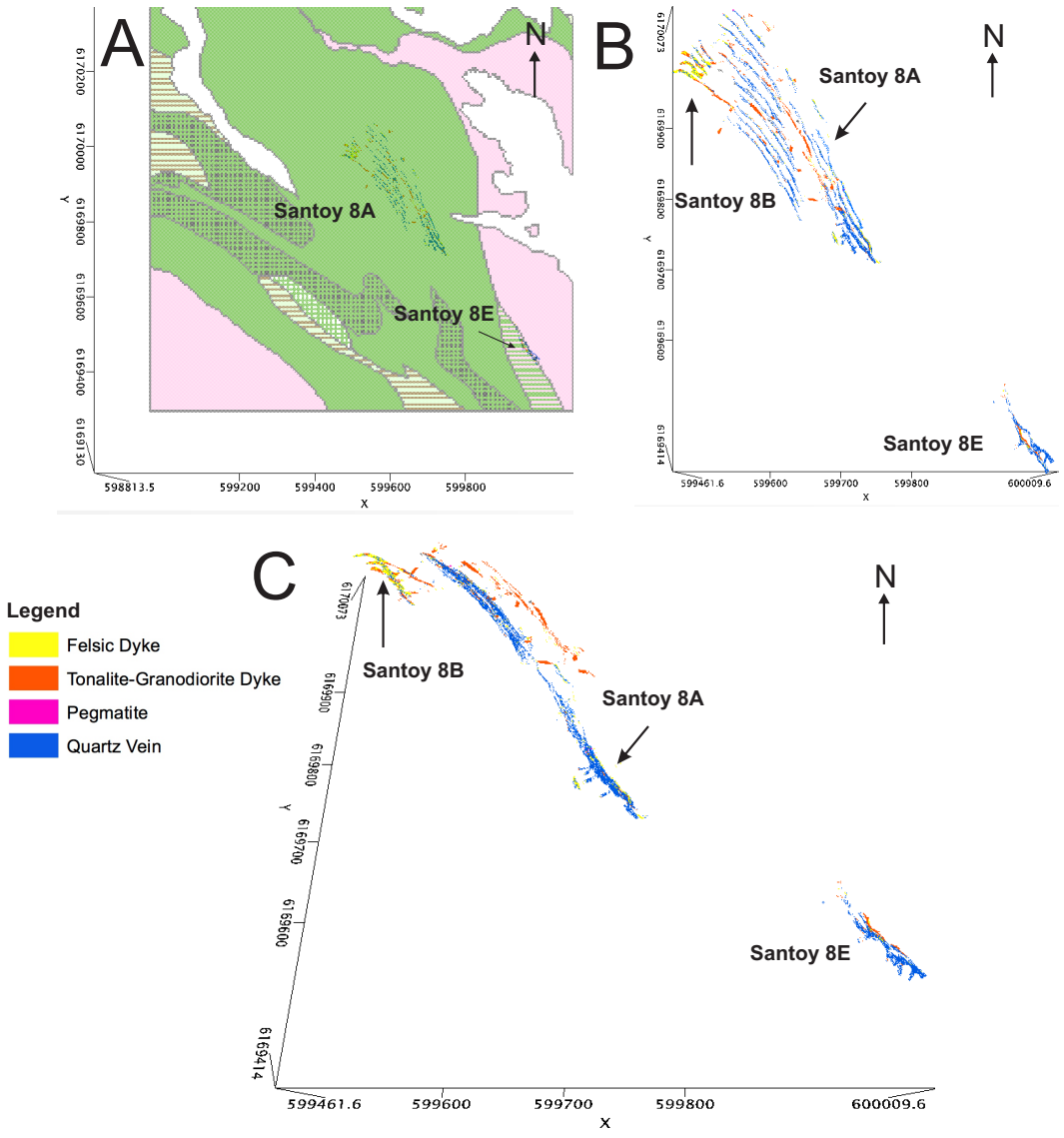

Figure 5.2: 3-D compilation of Santoy 8 and 8 East ore zone maps. A) Near-vertical perspective view of Santoy 8A and 8 East orebodies displayed with local geology overlaid. B) Vertical view of Santoy 8A and 8 East orebody without geological overlay. C) Down-plunge view of Santoy 8A and 8 East. Orebody rotated about dominant stretching lineation 45→000°. (original in colour)

5.2.1 Longitudinal Section

A longitudinal section prepared by Claude Resources Inc. and shown in Figure 5.3, displays the known extents of measured, indicated, inferred, and exhausted portions of the Santoy 8/8 East and Santoy Gap deposits from drill hole data. The section reveals that the highest-grade portions of the Santoy 8/8 East deposits plunge parallel to the axis (F_3) of the Carruthers Lake synform and the local dominant (L_3) lineation. The plunge of the high-grade zones in Santoy Gap, however, are somewhat less well defined. This could be due to a number of factors as these high-grade zones may be related to both the initial characteristics of deposit formation and later deformation/remobilization as mineralization ceased and D_3 progressed. It is important to note that care must be taken while interpreting this section because the orebody extent is somewhat based on economics (e.g., >= 3g/t), and not geologic structure alone. The definition of high-grade zones within the Santoy shear zone and deposits contained therein may change as gold prices fluctuate and mine development continues to progress.

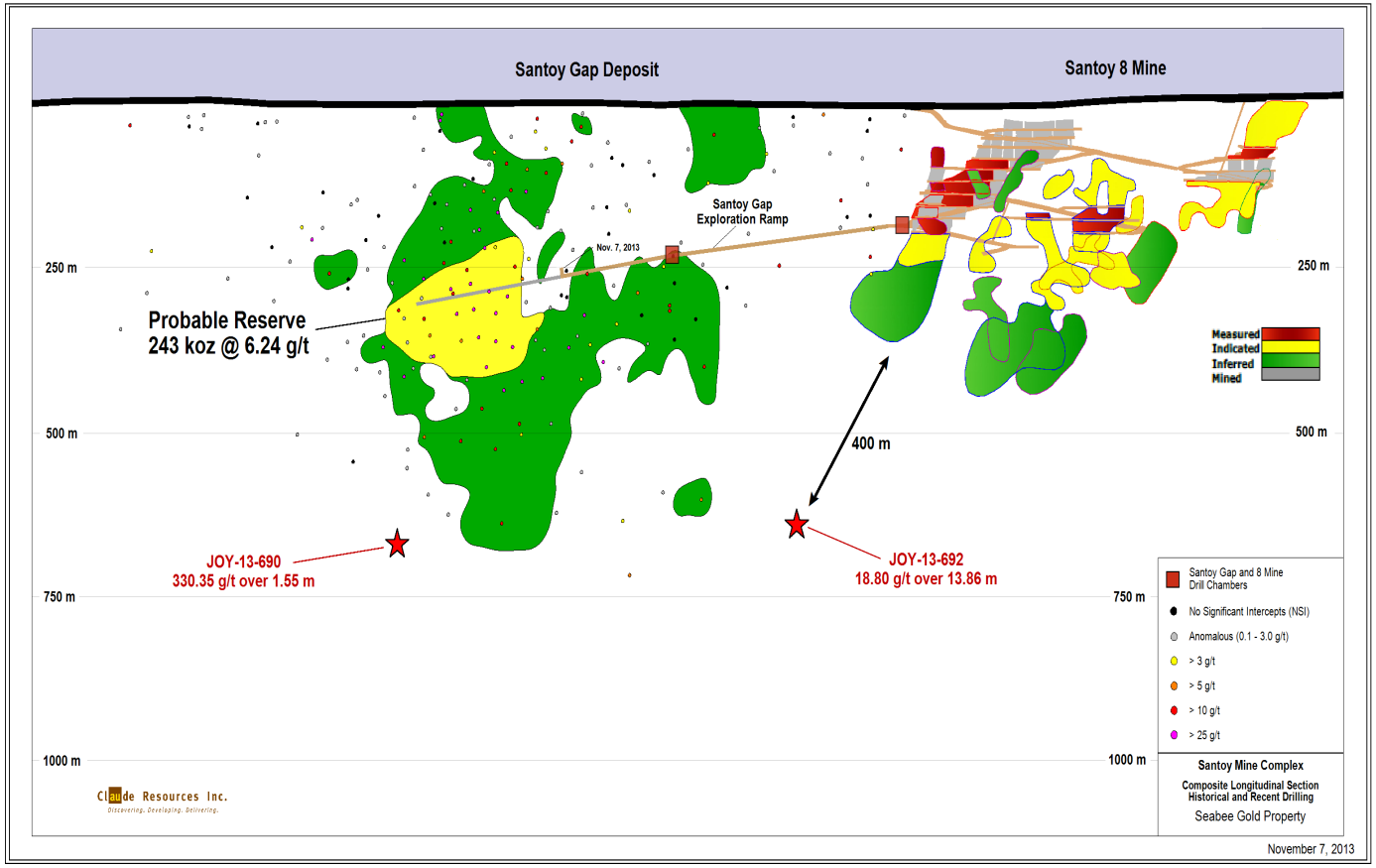

Figure 5.3: Longitudinal section of the Santoy 8, 8 East and Santoy Gap orebodies. Note, the extent of the orebodies is based on a cut-off grade 3 g/t (Claude Resources 2013; original in colour).

5.3 Detailed (deposit-scale) surface and subsurface mapping

5.3.1 Santoy 8A Deposit

The Santoy 8A ore lens is situated almost wholly within the mafic volcanic rocks west of the Lizard Lake pluton (Fig. 4.1 previous Chapter), and is characterized by numerous foliation parallel fault-fill quartz veins and calc-silicate altered wall rock. The surface expression of the Santoy 8A ore lens is limited; however, an excellent outcrop exposure of it was mapped (See Figure 4.2, previous chapter) at a scale of 1:28 in order to document its surface structural characteristics (Figure 5.4 and 5.5). In addition, part of the 8A lens was investigated underground to more fully characterize it in the third dimension. Quartz veins make up to 40% of the outcrop and invade strongly sheared mafic volcanic rocks lit par lit. The mafic volcanic rocks are strongly deformed, L-S tectonites with a NNW-striking, moderately east-dipping foliation and associated north-plunging mineral/stretching lineation. The quartz veins are generally foliation parallel to sub-parallel and display an anastomosing pattern typical of fault-fill veins (Robert and Poulsen, 2001). At least one isoclinally folded quartz vein on the eastern side of this outcrop was observed with its easternmost limb truncated against the main foliation. This observation indicates that other, possibly unrecognizable, (due to deformation) isoclinal folds are incorporated within this zone as well as the laminated quartz veins that contain numerous, elongate, foliated amphibolite slivers. These veins are also discontinuous both along strike and down-dip where they grade into isolated veinlets.

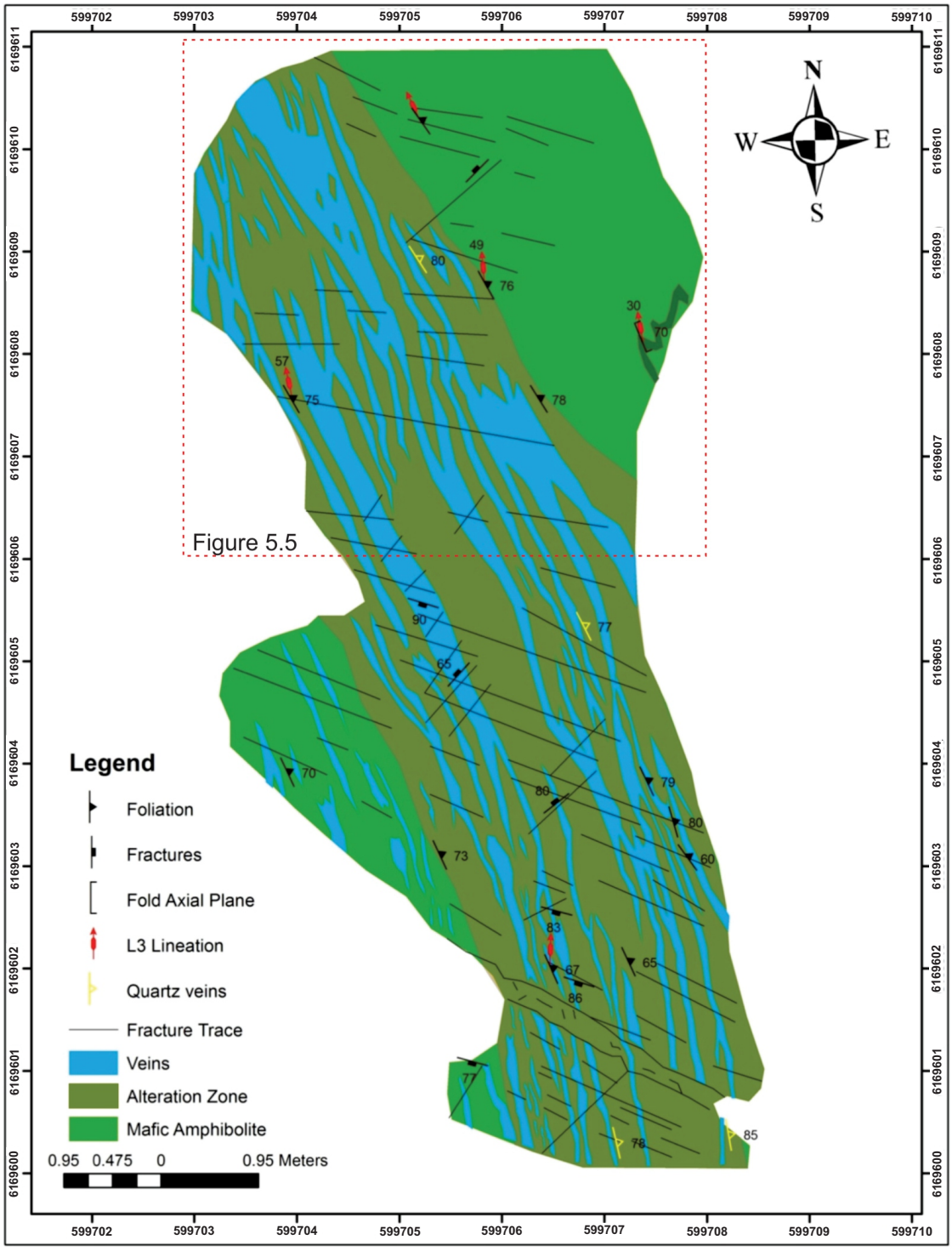

Figure 5.4: Detailed map of Santoy 8A surface expression. Location of outcrop shown by blue star on Figure 4.2 (previous chapter). (original in colour)

Figure 5.5: Outcrop Photograph of outlined area in figure 5.4. A series of photographs was taken and stitched together using Agisoft PhotoScan. (original in colour)

The mafic amphibole wall rock between quartz veins is generally pervasively altered. This diagnostic alteration, in most cases developed right along the contacts of quartz veins comprises an assemblage of calc-silicate minerals in discontinuous layers and lenses, including diopside, K-feldspar, titanite and amphibole, and is described in more detail in Chapter 6. In this outcrop, the calc-silicate layers/lenses have been boudinaged perpendicular to the L_3 lineation.

In terms of kinematics, there is no obvious asymmetry evident in outcrop on horizontal surfaces parallel to the strike of the foliation. This might be expected given the relatively steep plunge of the lineation. However, an oriented sample of material

containing boudinaged calc-silicate alteration was collected for more detailed investigation. In a slab cut perpendicular to the foliation and parallel to the lineation (Figure 5.6), rotated boudins are evident, indicating NE-side up displacement along the lineation. Given the orientation of the lineation and foliation, this translates to dextral-reverse displacement for the outcrop as a whole (Figure 5.7).

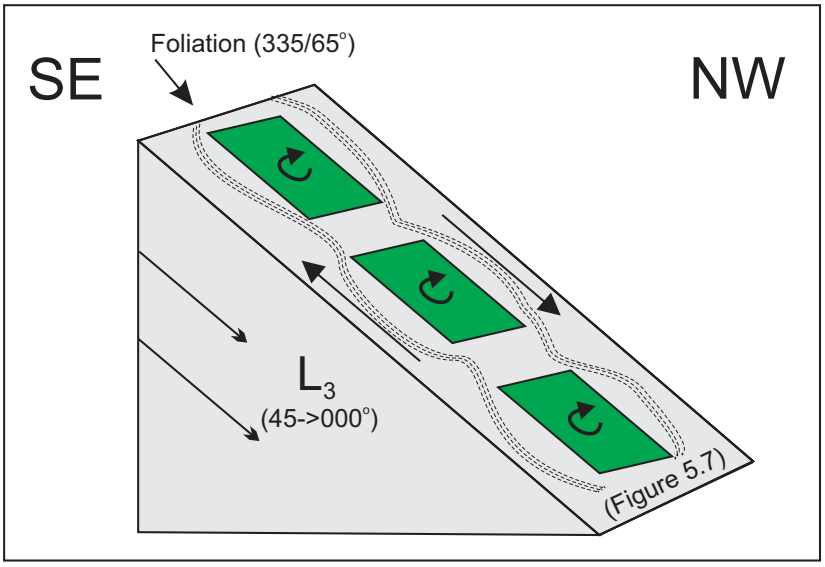

Figure 5.6: Oriented sample of boudinaged calc-silicate alteration from outcrop map (Figure 5.4). Figure displays orientation of Figure 5.7 (below). (original in colour)

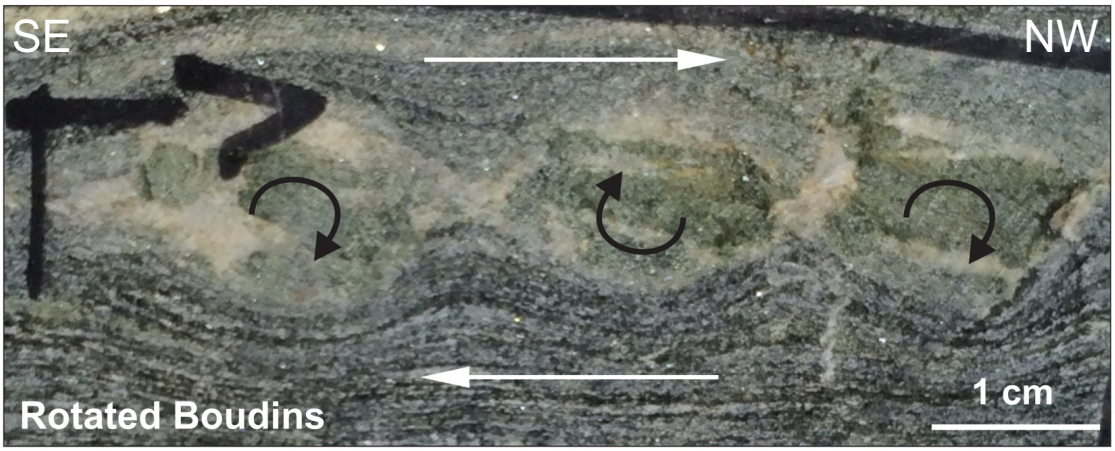

Figure 5.7: Boudinaged and rotated calc-silicate alteration. (original in colour)

In addition to Santoy shear-related ductile structures, two distinct sets of brittle fractures oriented approximately 106/84º and 227/73º dissect the outcrop with the 106/84º set preferentially developed (Figures 5.4, 5.8). These fractures likely represent a conjugate set and will be described in more detail in Chapter 8.

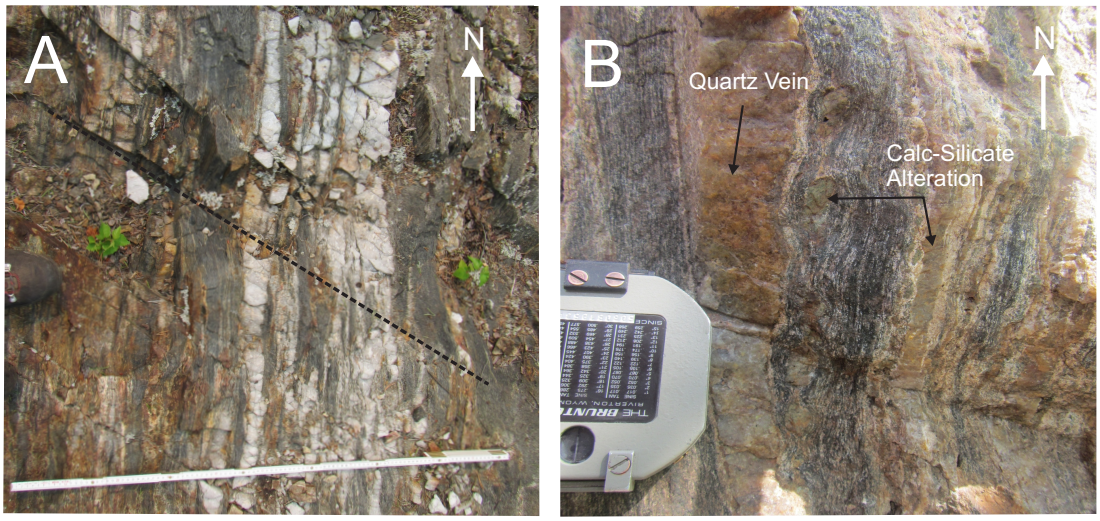

Figure 5.8: Fault-fill veins and alteration on surface. A) Anastomosing foliation-parallel fault-fill quartz veins cut by the dominant 106º-striking fracture set. B) Calc-silicate alteration developed marginal to quartz veins. (original in colour)

Due to the observation in the 3-D model that the subsurface expression of the Santoy 8A ore lens is structurally uniform in the vertical dimension, structural mapping and measurements could be made with a focus on changes in the orebody in a horizontal plane. Near-horizontal shafts mined parallel to and along the orebody are known as "sills" or "drifts". These passageways are shown in Figure 5.9, and were used to investigate one level of the Santoy 8A ore lens 160 m below the surface. Figure 5.10 (below) shows a typical cross-sectional view of the 8A ore lens underground. As can be seen on surface, this ore lens consists of highly strained laminated fault-fill veins and foliated wall-rock slivers with variably developed calc-silicate wall rock alteration along the quartz vein margins.

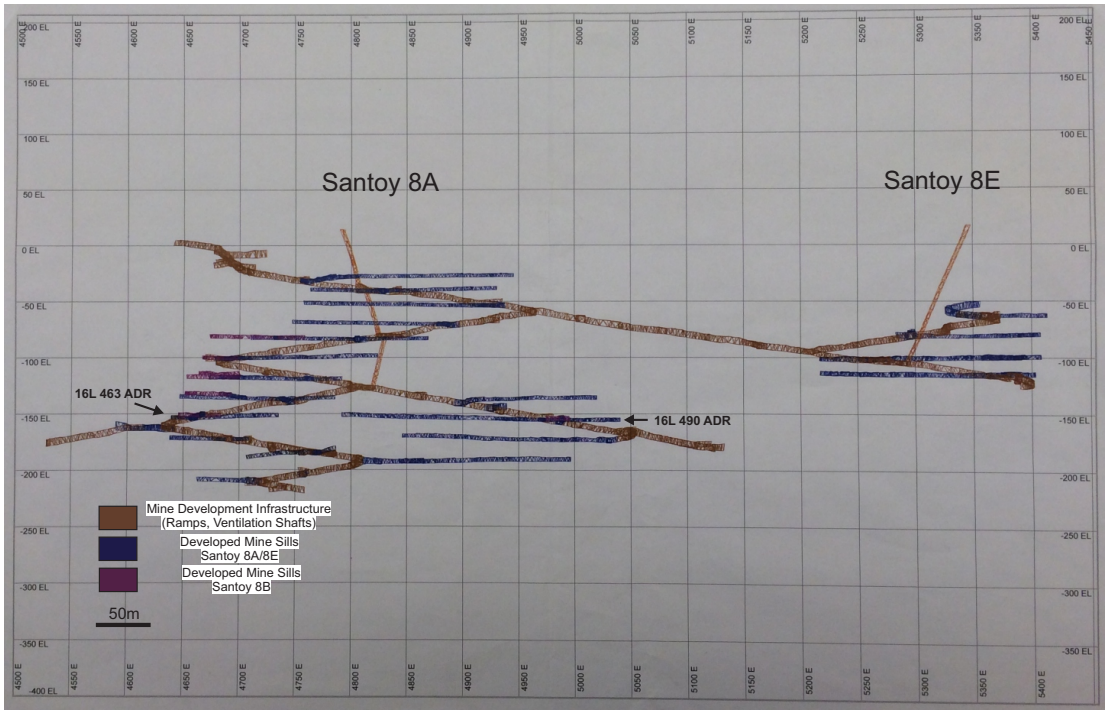

Figure 5.9: Longitudinal section looking east of the Santoy 8 and 8 East underground infrastructure. 16L 463 ADR and 16L 490 ADR correspond to mined "sills/drifts" studied by the author 160m below the surface. (original in colour)

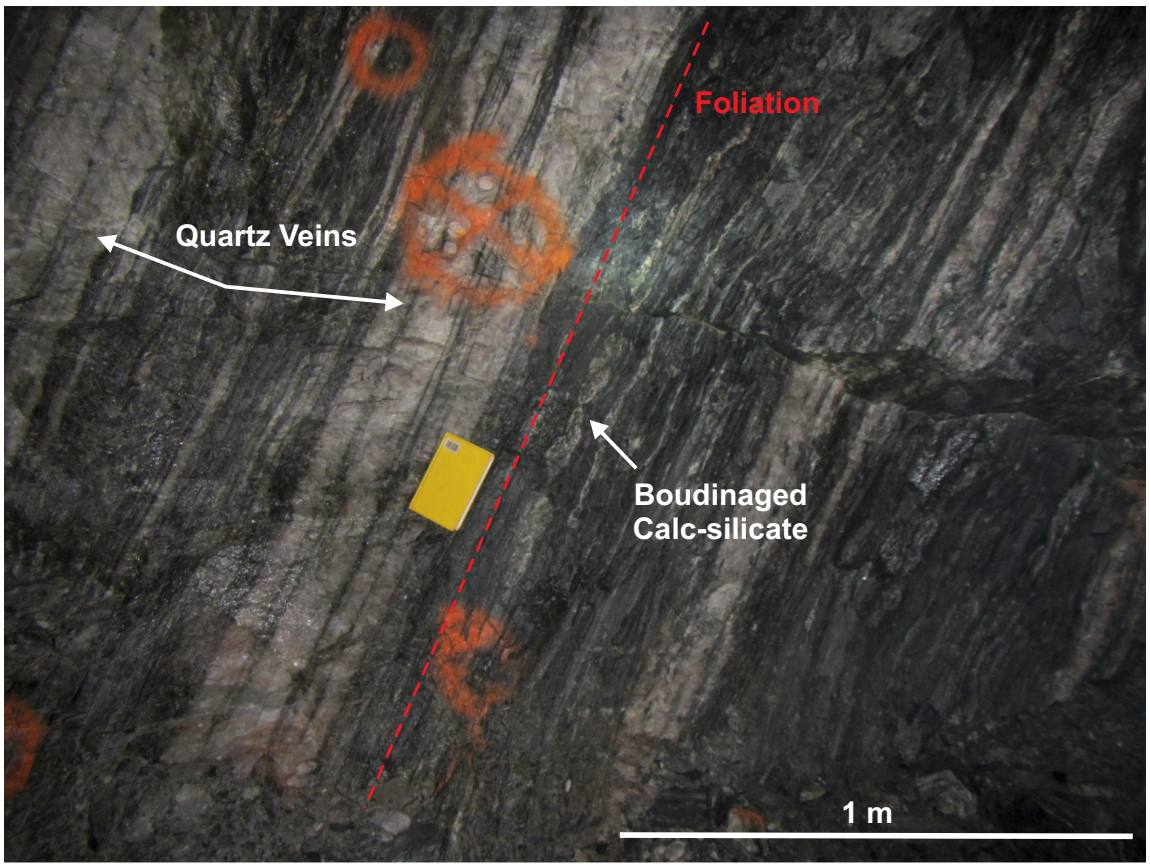

Figure 5.10: Cross-sectional view of Santoy 8A ore lens with boudinaged calc-silicate alteration. Photo oriented southeast perpendicular to strike; quartz veins oriented approximately 310/56°. (original in colour)

Due to the competency contrast between the alteration assemblage and quartz veins, the calc-silicate assemblage tended to boudinage forming dilational zones that are commonly filled with remobilized pyrrhotite, chalcopyrite, and pyrite. Very rare sub-vertical quartz veins were observed and are generally oriented perpendicular to the shear foliation and are folded. In addition, aside from the main lineation (L_3), variously expressed as a mineral and crenulation lineation, the better exposed foliation surfaces underground locally reveal an older mineral lineation (L_2) on $S_{2/3}$ foliation surfaces (Figure 5.11).

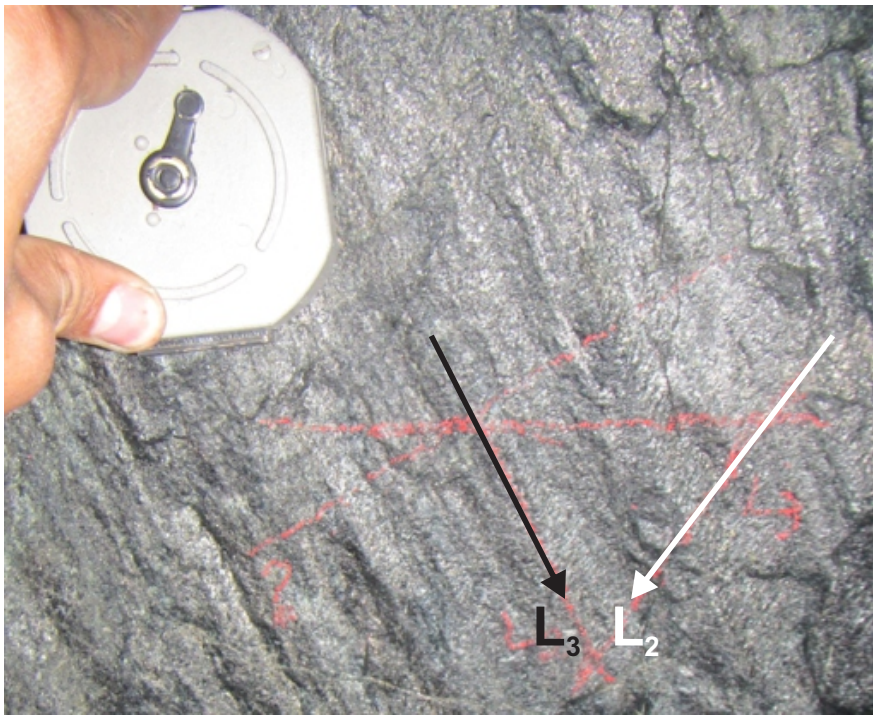

Figure 5.11: L_2 and L_3 lineations in subsurface. L_2 is a penetrative mineral lineation that can be observed on foliation surfaces and is defined by alignment of amphibole and biotite oriented approximately 56→101°. L_3 is a crenulation lineation that overprints the L_2 lineation as well as the foliation. (original in colour)

The ore zones themselves show a very close spatial relationship to numerous foliation-parallel granodioritic-tonalitic dykes and sheets, representative of the Santoy dykes on surface (Figure 5.12). High-precision age dating of one of these dykes was undertaken and the results and significance of this will be discussed in Chapter 7.

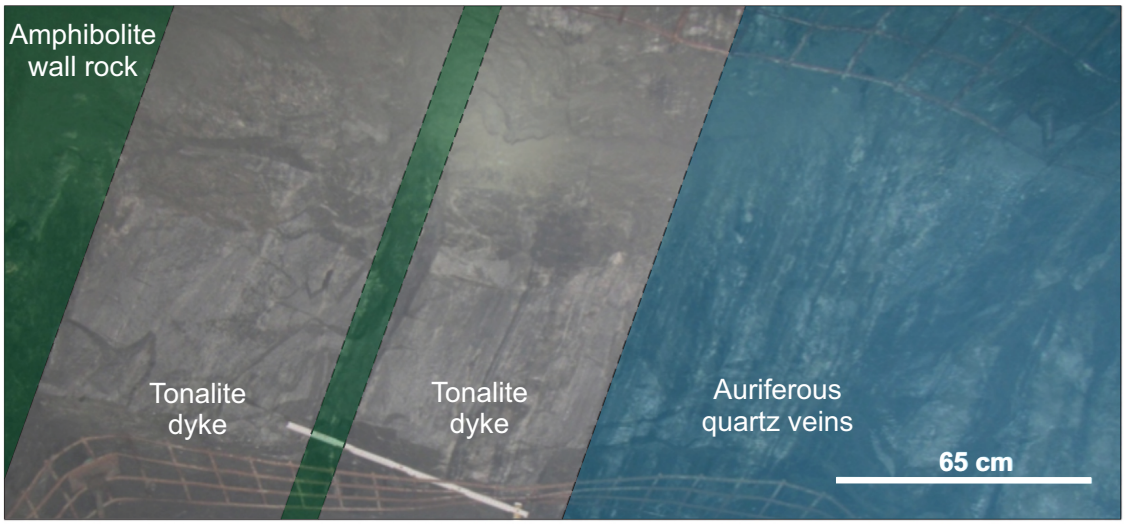

Figure 5.12: Cross-sectional view of ore zone-parallel hanging wall tonalite dykes. Photo facing S-SE. (original in colour)

The only crosscutting lithology observed in this part of the ore system was a beryliferous granitic pegmatite dyke. As illustrated in Figure 5.13A, this dyke cuts across shear fabrics and quartz veins of the ore zones, and is gently folded but not mineralized. A weakly developed F_3 axial planar cleavage indicates that the dyke was emplaced synchronous with, or during the late stages of deformation (Figure 5.13B). Owing to the fact that it places a lower limit on the timing of mineralization the dyke was sampled for geochronological analysis as discussed in Chapter 7. The pegmatite dyke is only weakly deformed and shows no evidence of displacement across the shear zone.

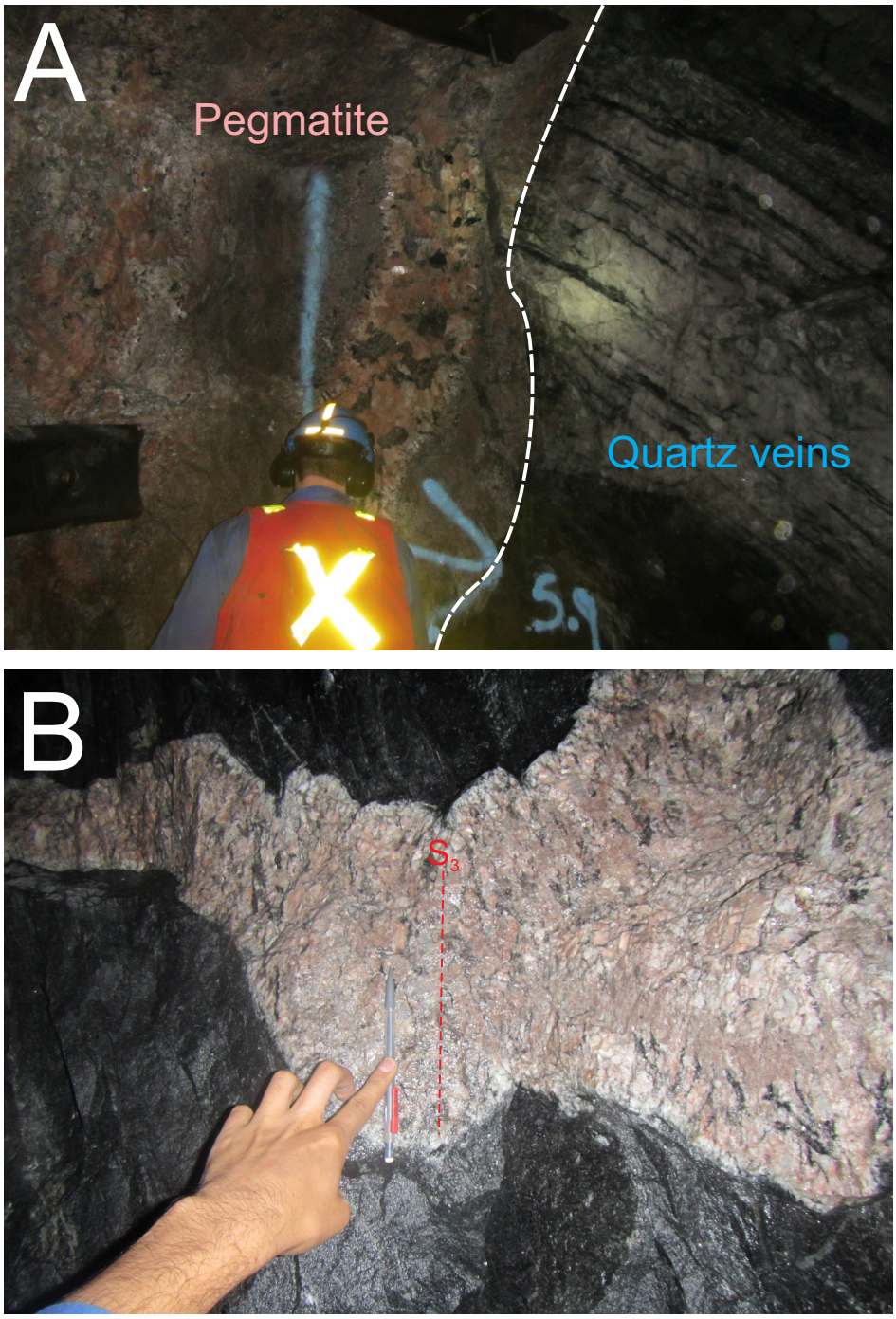

Figure 5.13: Nature of late-D_3 beryliferous granitic pegmatite dykes in the Santoy 8A deposit. A) Pegmatite dyke crosscutting auriferous quartz veins. B) D_3 folded pegmatite dyke containing F_3 axial planar cleavage. (original in colour)

Late, NNW-striking, moderately to steeply east-dipping discrete brittle faults occur sub-parallel to the ore zones and foliation (Figure 5.14A). They dominantly display a shallowly southeast-plunging slickenstriae (sinistral reverse oblique displacement) (Figure 5.14B). A second slickenstriae orientation was also observed to be shallow-moderately plunging to the northwest (sinistral normal oblique displacement) (Figure 5.14C). The displacement direction of these faults was evaluated by using the steps formed on the fault surfaces (Figure 5.14D). The similar orientation and character of these separate fault planes suggests that different movement directions may be related to reactivation after initial fault formation. These associated thin, discrete slip surfaces commonly have patchy, striated pyrite coatings; inboard of slip surfaces there is brecciated/calc-silicate wall rock, forming zones where less competent sulphides have migrated. These faults have also affected the pegmatites locally, but observed offsets are negligible.

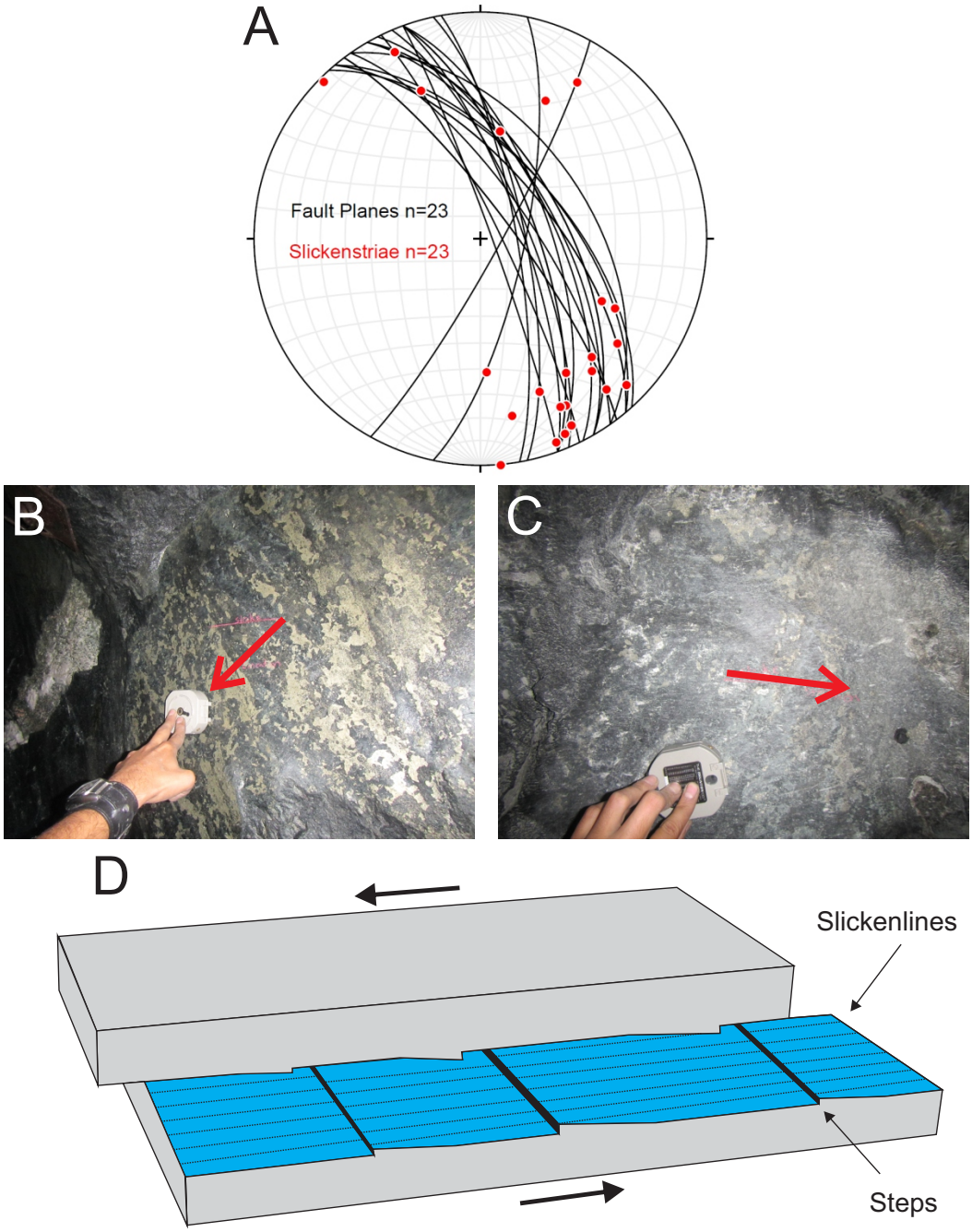

Figure 5.14: Characteristics of late NNW brittle faults. A) Stereographic plot of orientations of 23 NNW-striking faults and associated slickenlines. B) Example of patchy sulphides developed on smooth fault surface (012/74°) with slickenlines raking 43° from the SE. C) Example of smooth fault surface with sulphides oriented 334/83° and with slickenlines raking 10° from the NW. D) Steps formed on the fault surface allowed evaluation of movement directions. (original in colour)

There is also a prominent set of E-W striking, moderately south-dipping faults that crosscut the ore zones and display down-dip slickenstriae (Figure 5.15). At one locality along the Santoy Gap development ramp, a pegmatite dyke was observed to have been displaced in a reverse sense; the fault plane itself contained a ~ 20 cm wide barren quartz vein.

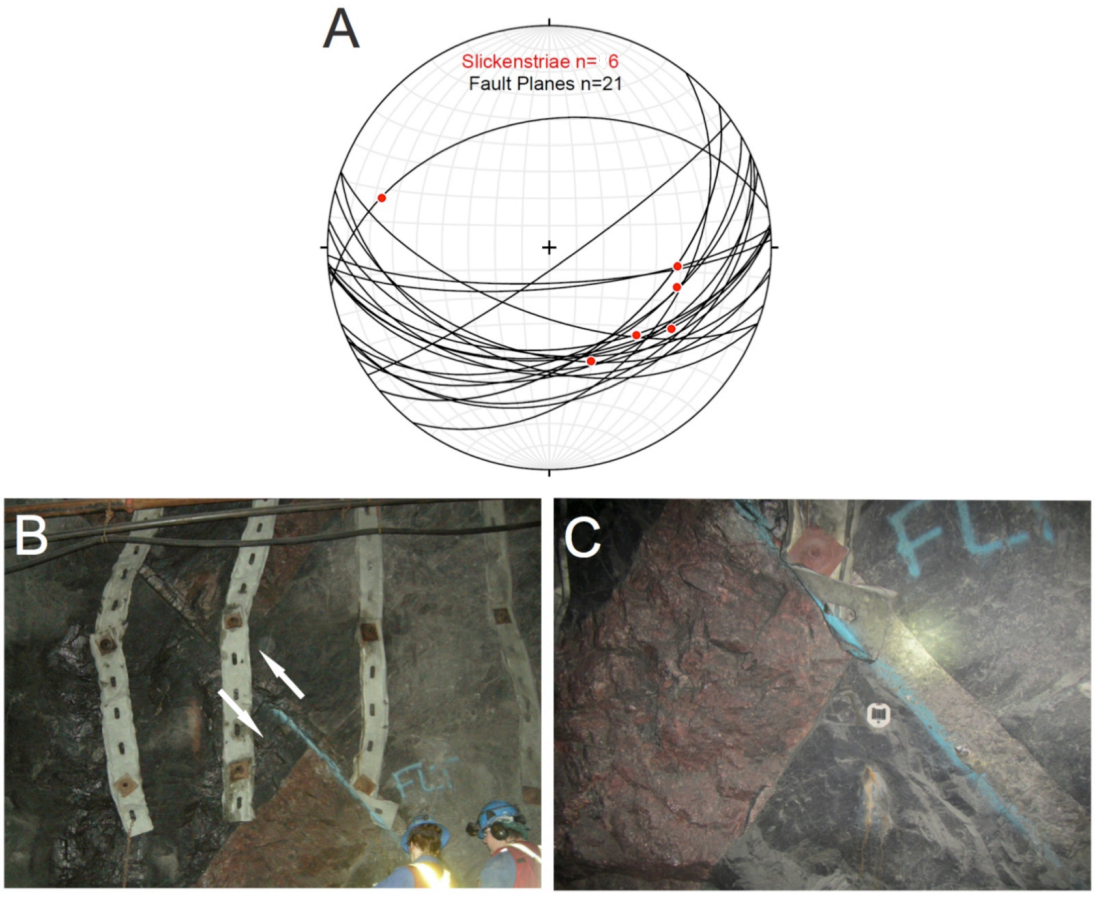

Figure 5.15: Chacteristics of late E-W Brittle Faults. A) Sterographic plot of orientations of 21 NNW-striking faults and associated slickenlines. B) A pegmatite dyke located in the Santoy Gap development ramp was displaced in a reverse manner. C) A 20 cm wide barren quartz vein was subsequently emplaced within the fault plane. (original in colour)

This indicates that E-W oriented faulting occurred after the development of the pegmatite dykes, and thus after mineralization, and that the barren quartz veins were emplaced well after the mineralization event.

5.3.2 Summary of mesoscopic structural relationships in Santoy 8A

Figure 5.16A is a block diagram summarizing the main structural characteristics of Santoy 8A ore lens and Figures 5.16B and 5.16C shows the related fabric elements plotted in stereographic projection. As suggested by 3-D-modelling, there is remarkable consistency in nature and orientation of various fabric elements between surface and depth. In particular, shear foliation and related lineations documented throughout the mine are identical to those seen on surface. The π-pole plot in Figure 5.16B also demonstrates that the $S_{2/3}$ foliation has been folded around a common axis (F_3), which corresponds closely in orientation to the plunge of the Carruthers Lake synform documented at the regional scale. As reported above, two lineations are present in this system, L_2 and L_3. L_2 is a penetrative mineral lineation that can be observed on foliation surfaces and is defined by alignment of amphibole and biotite oriented approximately $56 \rightarrow 101^{o}$. L_3 is a crenulation lineation that overprints the L_2 lineation as well as the ($S_{2/3}$) foliation.

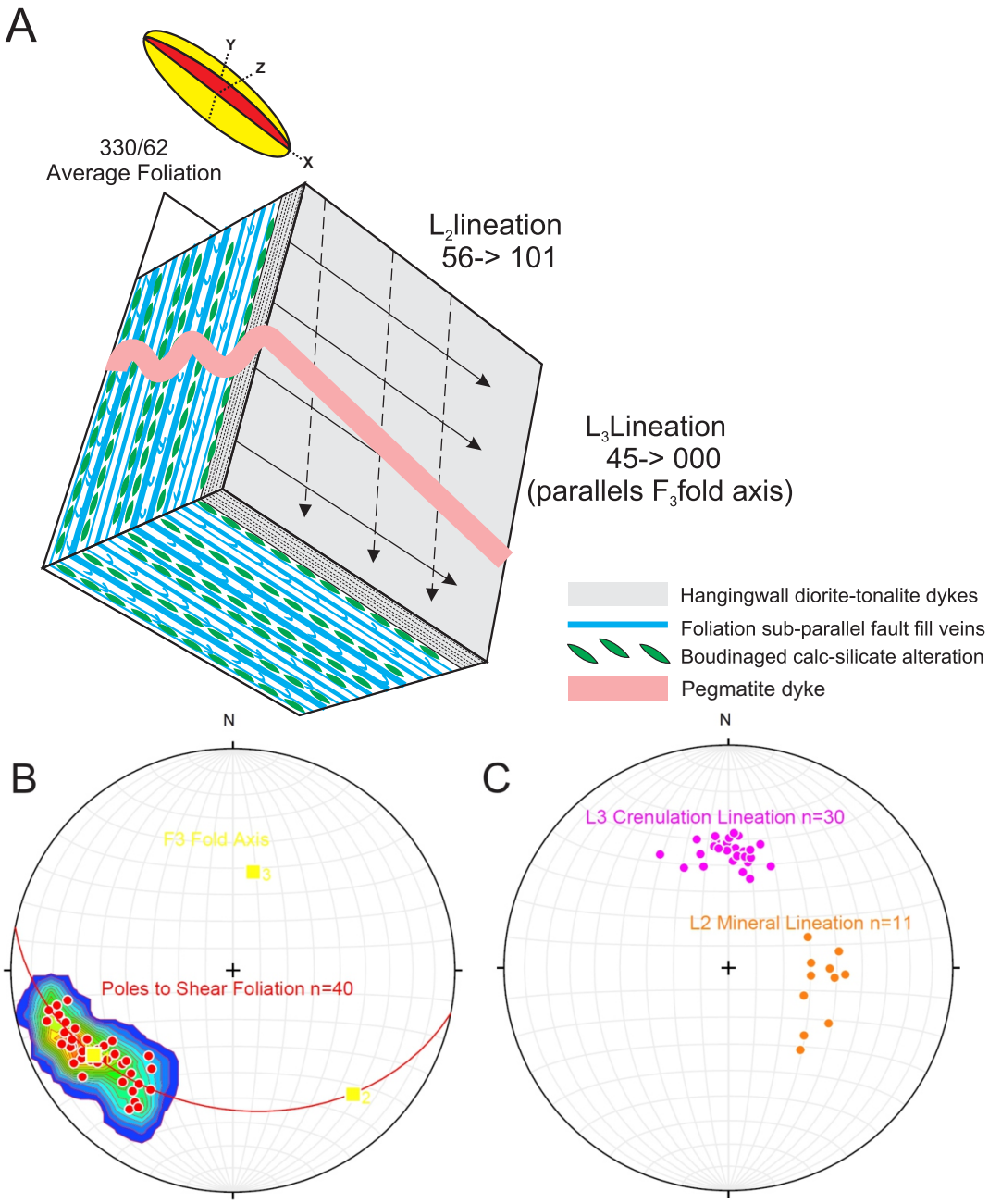

Figure 5.16: Tectonic fabric elements of the Santoy 8A orebody as documented in subsurface investigation. A) Block diagram of Santoy 8A ore lens displaying dominant lithological and structural features. B) π-Pole plot of the main foliation, the poles define a great circle, the pole to which defines the F_3 fold axis, 53→011° C) Linear elements within Santoy 8A. L_3 mean vector is 46→000° and L_2 mean vector is 56→101°. (original in colour)

The above diagram also illustrates that the attenuated layers and lenses of calc-silicate alteration parallel to $S_{2/3}$ are apparently boudinaged in two directions; measurements of the boudin axis (L_B) in Figure 5.17A however, indicates extension perpendicular to the L_3 stretching lineation. The diopside porphyroclasts typically display symmetrical Φ type geometries of the boudins. However, as discussed in section 5.3.1, the boudins are locally rotated indicating reverse displacement along the L_3 lineation. Both the boudinage and lack of asymmetry point to a strong component of flattening (normal strain) within this zone.

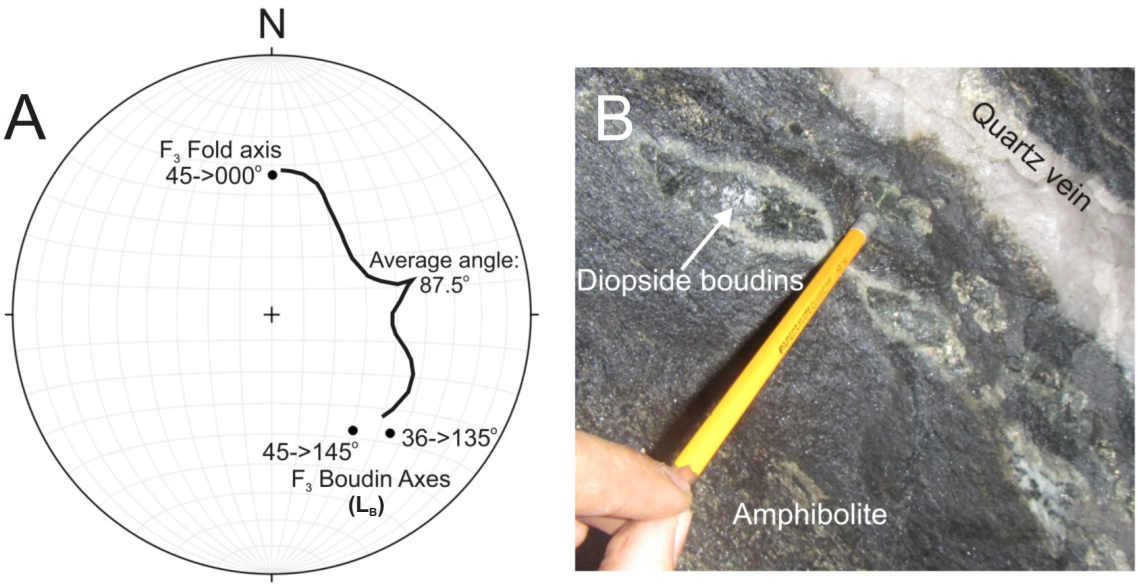

Figure 5.17: Boudin axes (L_B) in the Santoy shear zone. A) The angle between L_3 stretching lineation and boudin axes is approximately 90°. B) Diopside boudins parallel to the quartz veins and foliation. (original in colour)

5.3.3 Santoy 8 East

As implied by the 3-D model, the Santoy 8 East deposit is fundamentally different in character from Santoy 8A in that the structure is dominated by gentle to open F_3 folding.

In the surface exposure of Santoy 8 East, quartz veins have been injected mainly into mafic-volcanic amphibolite marginal to the contact of the Lizard Lake pluton (Figure 5.18). Locally the quartz veins and calc-silicate alteration are observed to cut the S_2 fabric (at variable angles) and are open to closely folded by F_3 forming S folds that plunge parallel to the F_3 fold axis.

Figure 5.18: Surface expression of Santoy 8 East. F_3 folded quartz veins and wall rock fragments. Photo oriented NNW approximately down-plunge of the fold axis. (original in colour)

Owing to the fact that this part of the vein system is variably folded, subsurface ore zones in Santoy 8 East are structurally much more complex that those in Santoy 8A. In Figure 5.19, a wallrock fragment that was incorporated into the fault-fill vein system

was folded around the F_3 fold axis. This reveals that the fault-fill vein system incorporated the wall-rock fragment and subsequent deformation folded the foliated wall rock fragment and enclosing vein material about the F_3 fold axis producing this final structural configuration.

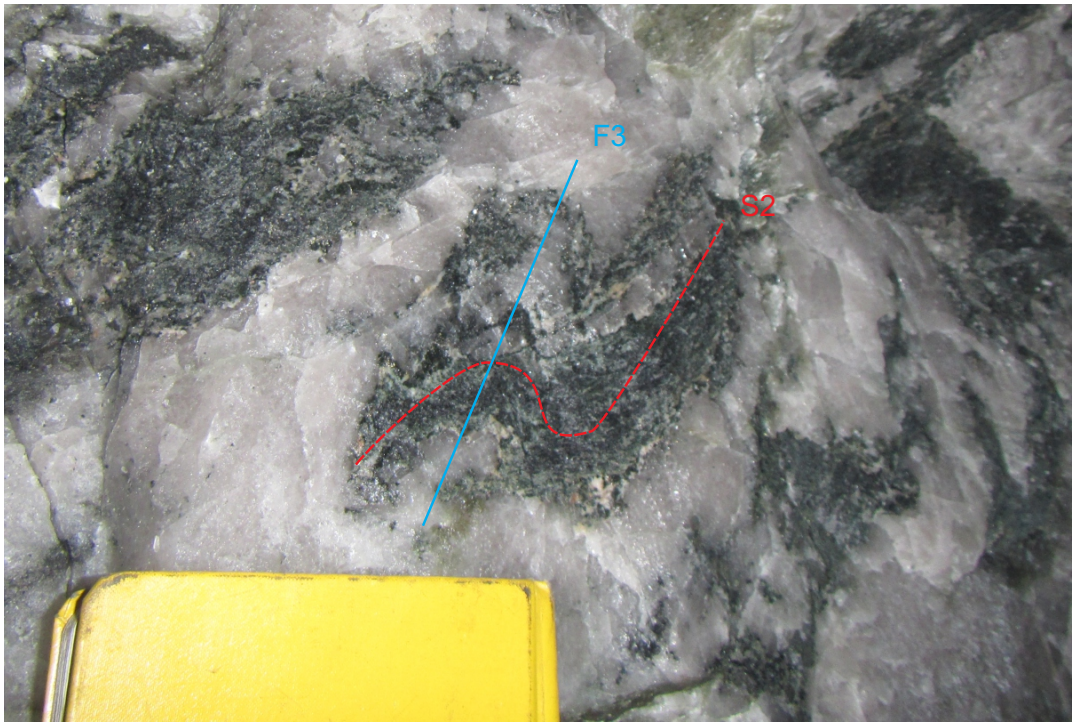

Figure 5.19: F_3 folded wall rock fragment located in Santoy 8 East. S_2 foliation defined by amphibole is truncated by the quartz vein and both were subsequently folded about the F_3 fold axis. (original in colour)

On a larger scale, the structural character and complexity of Santoy 8 East is largely caused by the reorientation of the system by these 45→000º plunging S-folds along the western limb/hinge of the Carruthers Lake synform. The plunge of these folds controls the plunge of the deposit in this location (Figure 5.20).

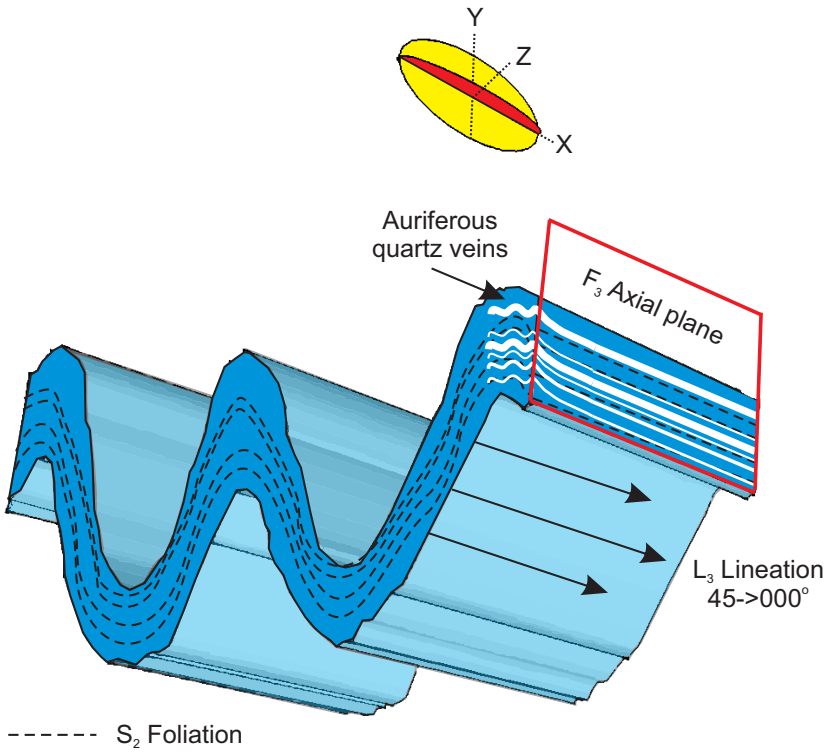

Figure 5.20: Tectonic fabric elements of the Santoy 8 East orebody. (original in colour)

5.4 3-D strain scenario and kinematics of the Santoy shear zone

As reported above, strain markers within the Carruthers Lake synform and Santoy shear zone include folded and boudinaged dykes, quartz veins, and calc-silicate alteration. Across the map area, markers oriented at a high angle to the foliation and shortening field of the F_3 strain ellipsoid are folded, whereas markers oriented at a low angle to the foliation and within the extensional field of the strain ellipsoid are boudinaged. The 3-D strain ellipsoid for the map area is included in Figure 5.21 while representative structures located in each sector of the 2-D strain ellipse are included in Figure 5.22. The foliation

contains the x-y plane and related $1 + e_1$, $1 + e_2$ axes, while the lineation (L_3) parallels the $1 + e_1$ direction.

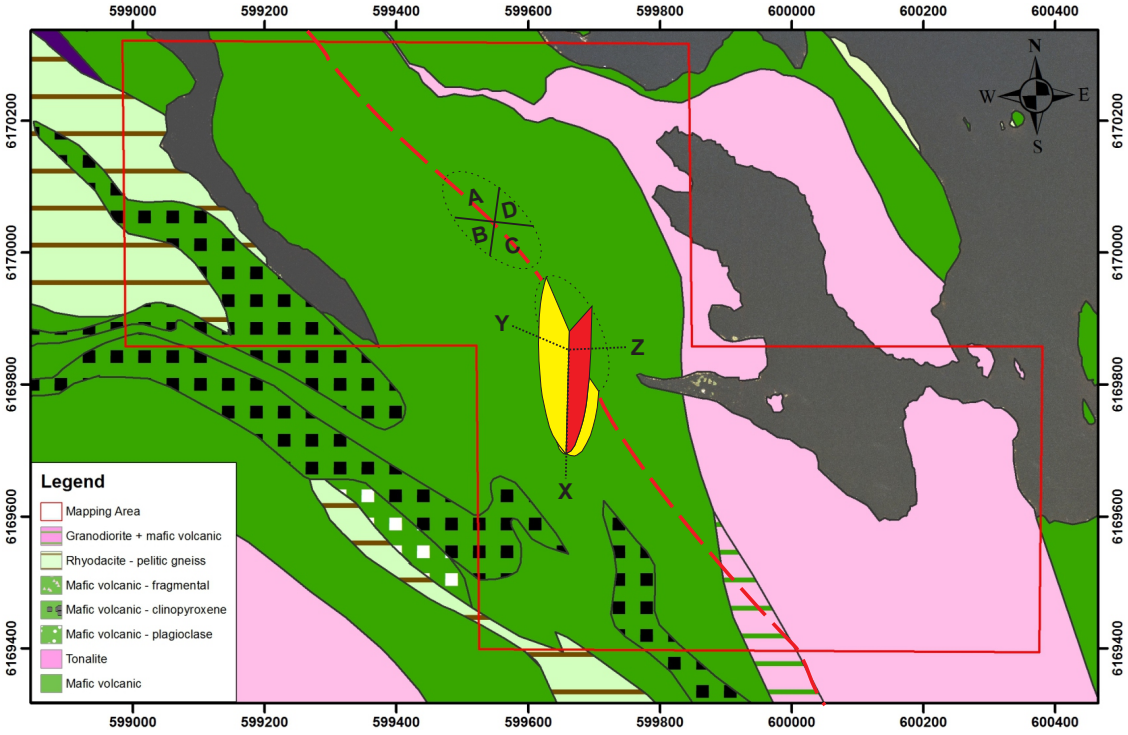

Figure 5.21: 3-D Strain ellipsoid for Santoy area. X axes oriented along the main stretching lineation plunging 45° towards north. A, B, C, and D refer to individual sectors of the 2-D strain ellipse and Figure 5.22. (original in colour)

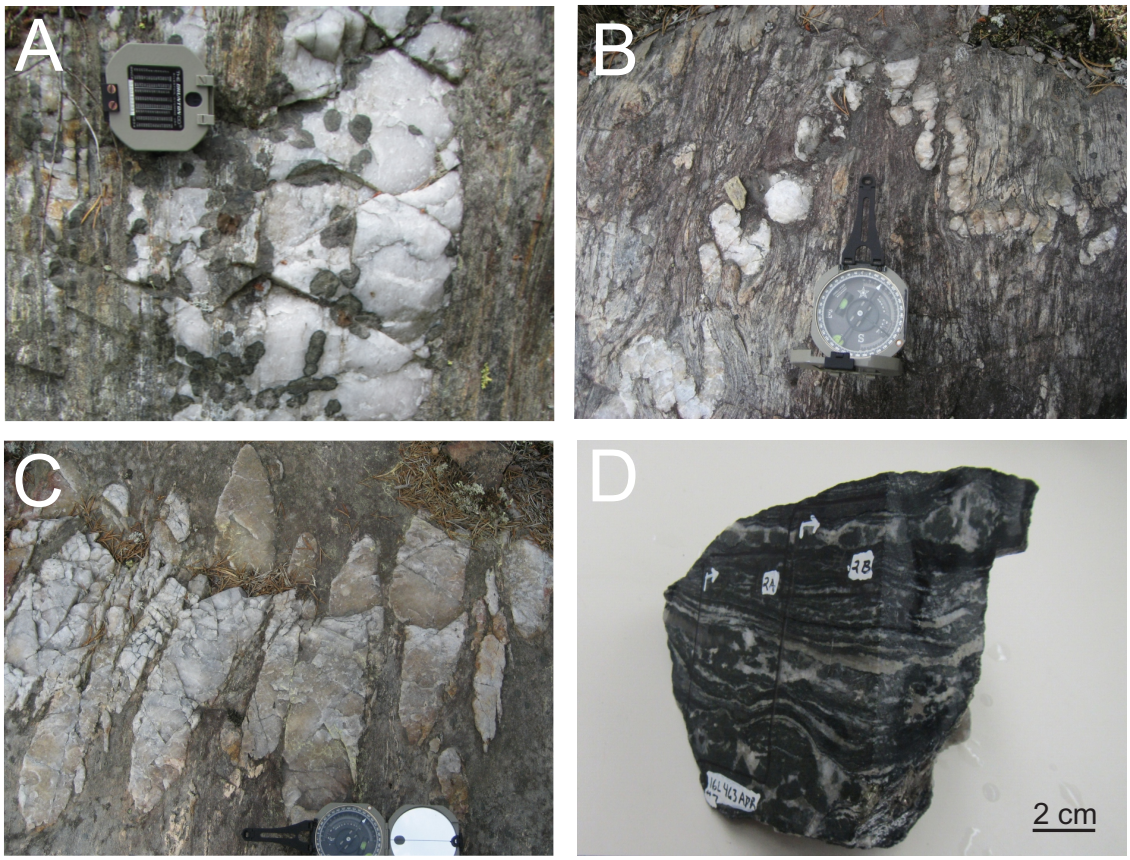

Figure 5.22: F_3 strain markers. A) Highly strained foliation parallel quartz veins crosscut by brittle conjugate fracture set. B) F_3 M folded quartz vein with associated S_3 cleavage. C) Folded and rotated quartz vein, aligned with S_3 fabric D) Calc-silicate alteration cut parallel and perpendicular to L_3 lineation displaying apparent boudinage in two directions. (original in colour)

The strong component of flattening (normal stress) is dominant in the map area however the fault-fill character of the auriferous veins within Santoy 8/8 East and Gap, as well as the analysis of several oriented thin sections (Figure 5.23), indicate there was also a significant simple shear strain component in the development of this shear zone. In order to accurately deduce the sense of shear, kinematic indicators must be viewed in sections perpendicular to the foliation and parallel to the stretching lineation (L_3) in the X-Z plane of the strain ellipse. As mentioned earlier in Chapter 5, the presence of rotated

boudins of calc-silicate alteration in the surface exposure of the Santoy 8A ore lens suggests dextral-reverse kinematics. Two other microstructural samples also display rotated porphyroclasts and CS-S-C' fabrics that both indicate dextral-reverse oblique sense of shear during D_3 deformation (Figure 5.24). Strain markers that are younger than the quartz veins and crosscut the shear zone (pegmatite dykes) were not observed to show any ductile shear offset.

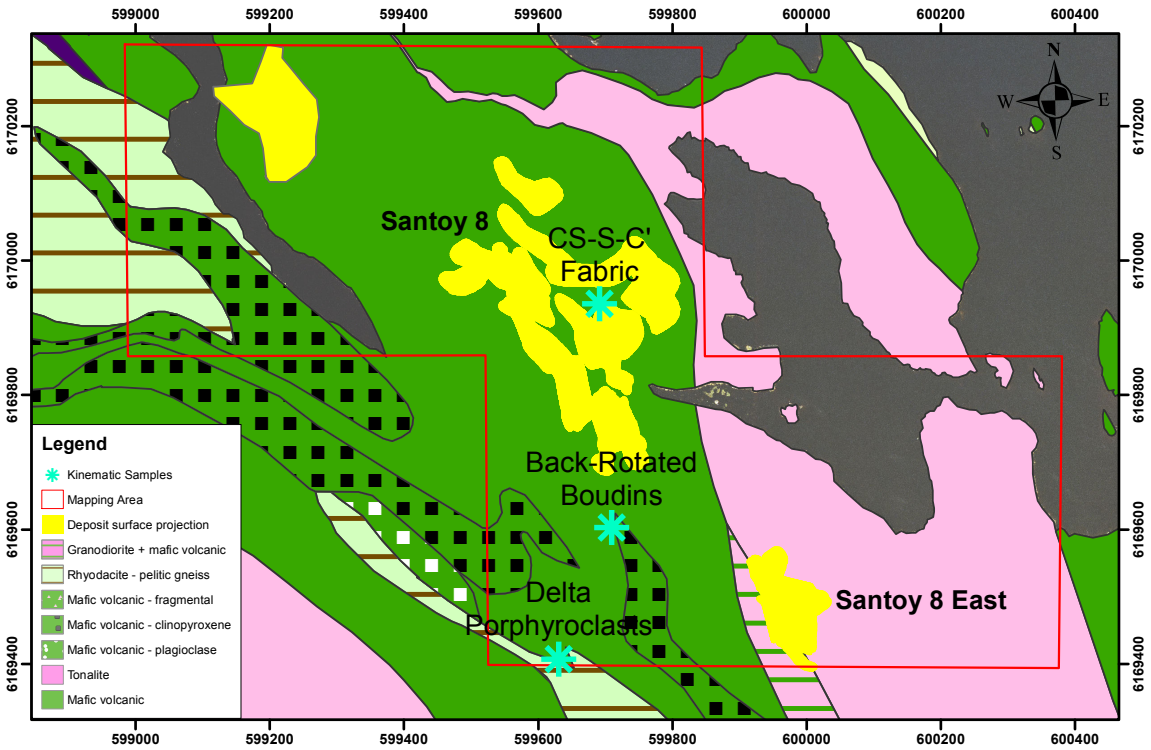

Figure 5.23: Location of samples displaying kinematic indicators. (original in colour)

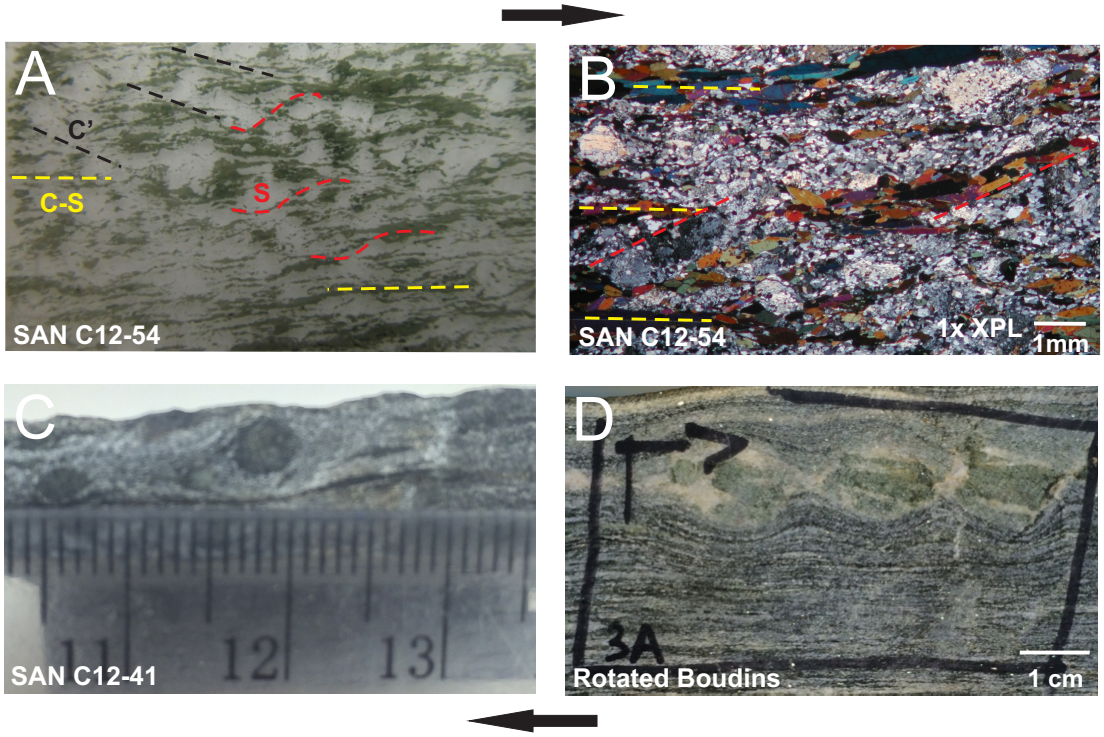

Figure 5.24: Kinematic indicators of the Santoy shear zone. A) Photo of thin section showing kinematic fabrics developed within mafic amphibolite. B) Photomicrograph of amphibolite with C-S and S fabrics developed. C) Dextrally rotated delta-type porphyroclast in mafic amphibolite matrix. D) Rotated boudins of calc-silicate alteration. All samples suggest dextral reverse kinematics for the Santoy shear zone. (original in colour)

5.5 Stress-strain relationships

In the preceding sections the finite 3-D strain ellipsoid was derived for the Santoy shear zone. While there is clearly a large component of normal stress acting on this zone, there is also a significant shear stress (non-coaxial) component as well. During non-coaxial deformation, theory holds that the long axis strain ellipsoid rotates, the $1 + e_1$ direction becoming increasingly sub-parallel with the shear plane (X direction of external reference frame) (Ramsay and Huber, 1987). Due to this non-coaxial simple shear component there is not enough information to derive the stress directions based on the strain ellipsoid

alone. Also, due to post-vein strain, tilting, and interaction with the Packman Lake pluton discussed in Chapter 8, the analysis of the veins in terms of their causative stresses becomes increasingly enigmatic.

Many gold deposits and gold districts, however, have undergone sub-horizontal compression ($\sigma 1$ horizontal) with gold-bearing veins emplaced under high fluid pressures within moderately to steeply-dipping regional shear zones (Sibson et al., 1988; Robert and Poulsen, 2001; Morrelli and Machlaclan, 2012). For the purposes of further discussion and analysis in Chapters 8 and 9, $\sigma 1$ will be assumed to be approximately oriented horizontal and the $\sigma 1/\sigma 3$ plane will contain the L_3 lineation as well as the pole to the fault.

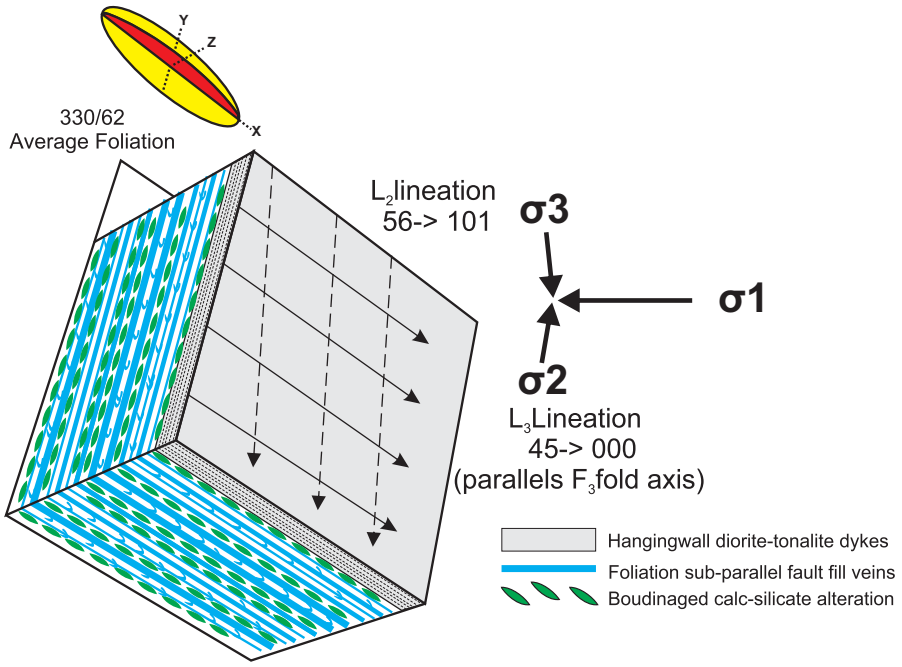

Figure 5.25: Stress-strain relationships of the Santoy shear zone. $\sigma 1$ is oriented horizontally and the $\sigma 1/\sigma 3$ plane contains the L_3 lineation and the pole to the fault. (original in colour)

CHAPTER 6

NATURE OF GOLD MINERALIZATION

6.1 Introduction

Durocher et al., (1993) and Durocher (1997) undertook a petrographic study of the ore/alteration mineral assemblages of the Santoy showings (Zones 1-8) and divided ore zone development into two stages within D_2 shear zones. The mineral paragenesis reported by Durocher's (1993, 1997) study, however, includes observations from many showings/zones with variable mineralogy and it is unclear how these observations relate to the Santoy deposits themselves (Santoy 7, 8/8 East, Gap). In this study, access to the Santoy 8 mine and drill core from the Santoy Gap, which were unavailable during Durocher's study, allowed the ore and alteration paragenesis specific to the Santoy deposits to be re-evaluated. This work indicates that main-stage gold mineralization in the Santoy shear zone shows a clear spatial relationship with quartz veins and calc-silicate alteration. During the summers of 2012 and 2013, petrographic samples were collected with two goals in mind.

1. To characterize key lithologies and ore/alteration mineral assemblages both petrographically and from sill and outcrop observations.
2. To document the mineralogical and textural setting of gold mineralization.

6.2 The calc-silicate alteration assemblage

As shown in Figure 6.1, the calc-silicate alteration is commonly developed right along the margins of the quartz veins demonstrating that the alteration is genetically related to veining, and in turn, mineralization.

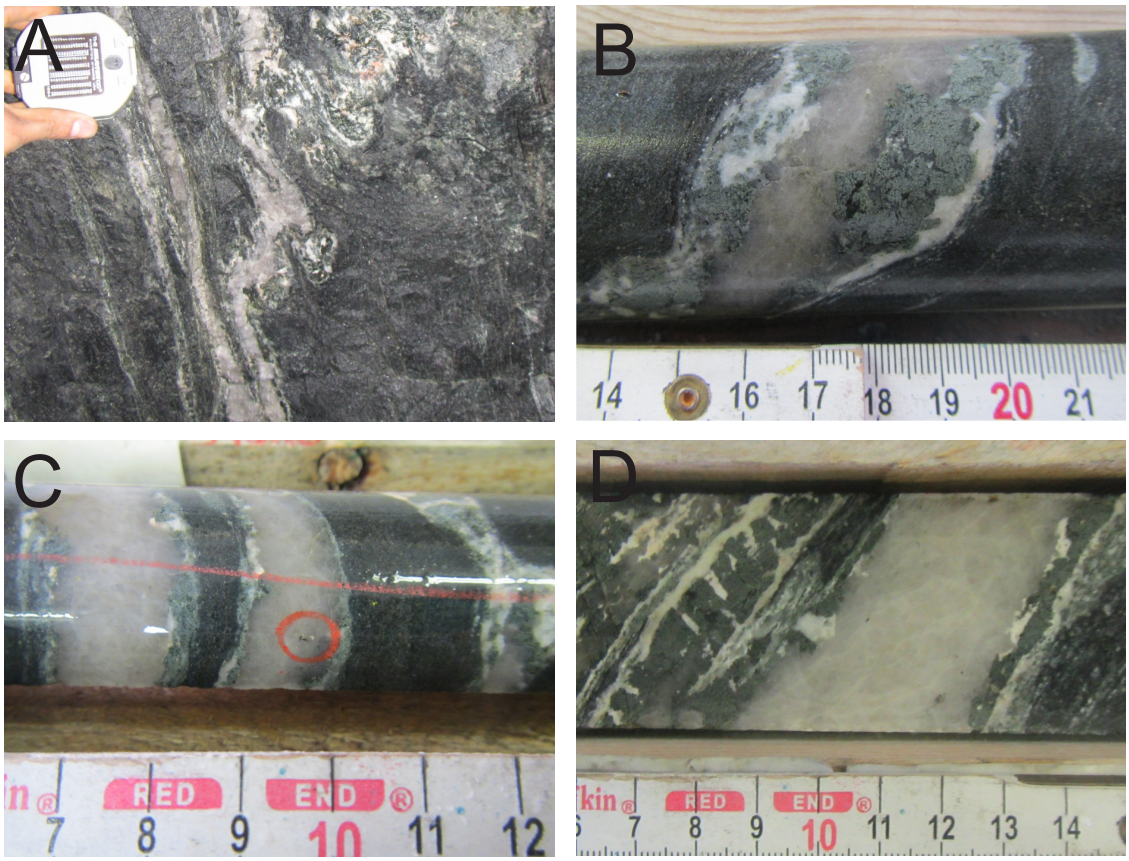

Figure 6.1: Quartz vein-alteration relationships. A) Isoclinally folded quartz vein with calc-silicate alteration developed directly on the quartz vein margins. B) Quartz vein with diopside, K-feldspar, plagioclase, and titanite-rich margin. C) Visible gold (circled in red) within quartz veins. The thin alteration salvages mantle the quartz veins but do not extend very far into the host amphibolite. D) Calc-silicate alteration displaying boudinage. The competent nature of the calc-silicates, and the tendency of it to boudinage and fracture during deformation allows sulphides to flow into dilatent zones. (original in colour)

The mineralogy of calc-silicate assemblage can be quite variable in terms of modal percentages of minerals present and degree of deformation; however, this assemblage is generally characterized by a combination of diopside, quartz, K-feldspar, plagioclase, titanite, and actinolite, with accessory gold, pyrrhotite, pyrite, chalcopyrite, calcite, scheelite, apatite, and zircon (Figures 6.2, 6.3, 6.4).

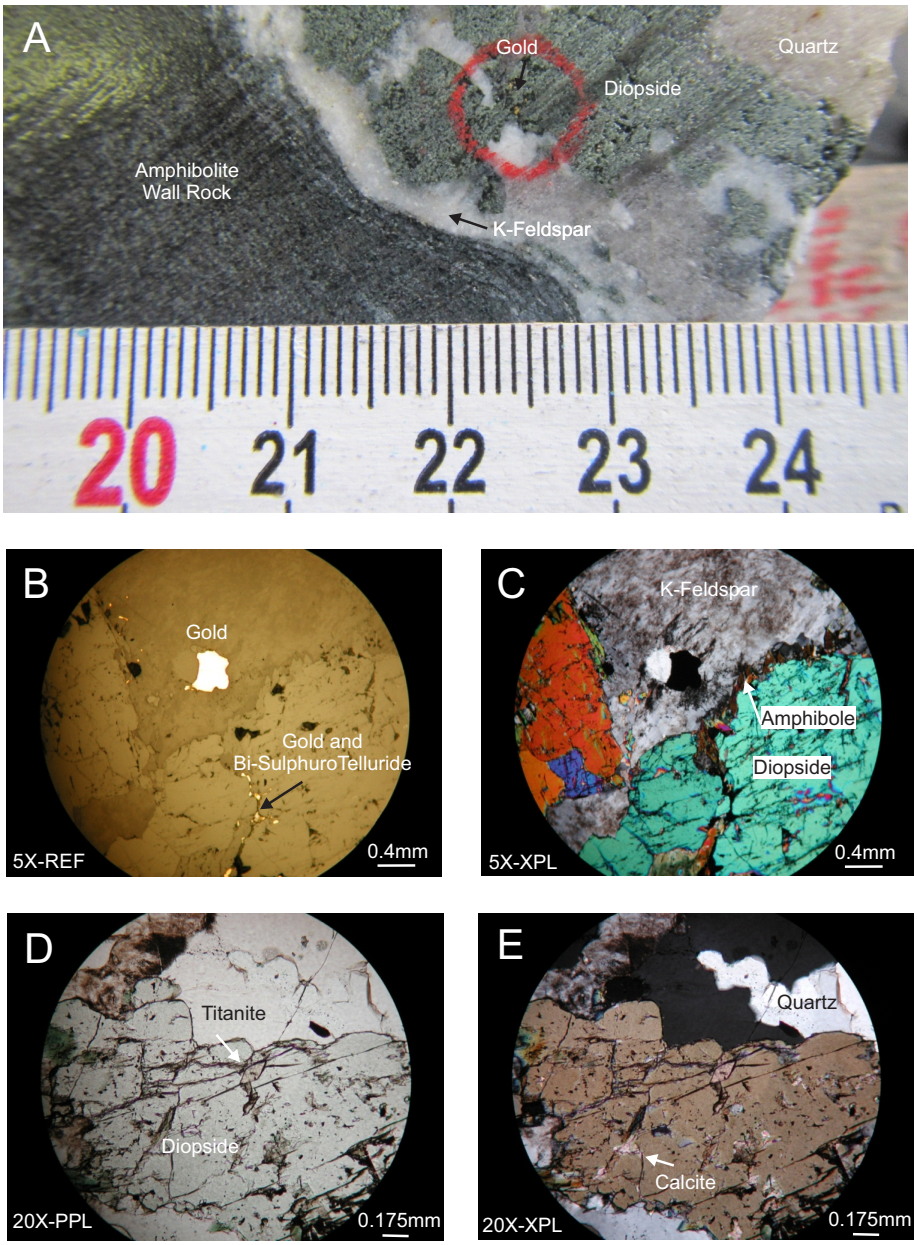

Figure 6.2: Calc-silicate alteration assemblage. A) Santoy Gap core sample displaying boudinaged calc-silicate alteration with visible gold mineralization hosted within diopside. B) Photomicrograph in reflected light of gold and Bi-tellurides within K-feldspar. C) Photomicrograph showing reaction rim of actinolite on margins of diopside crystals; some gold mineralization is associated with this and may be remobilized. D) Photomicrograph in plane light of euhedral titanite within the diopside host. E) Photomicrograph in cross-polarized light showing titanite within diopside surrounded by deformed quartz and minor calcite replacement of diopside. (original in colour)

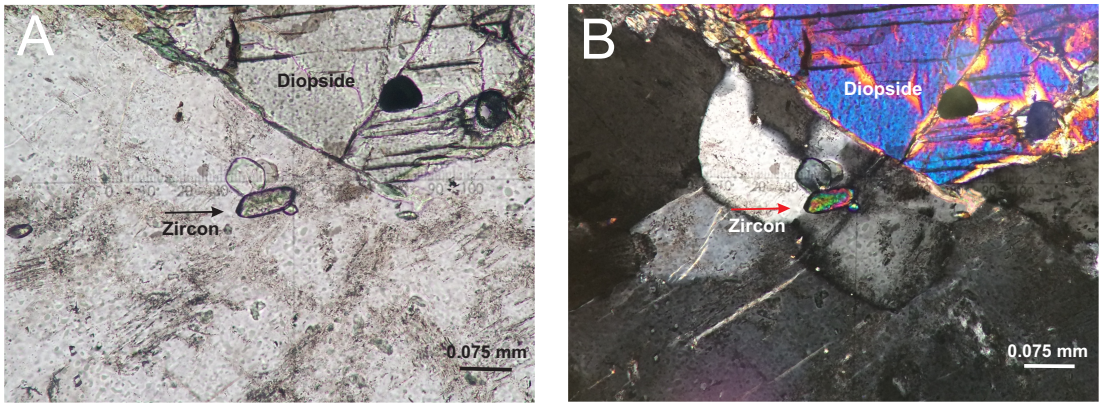

Figure 6.3: Textural setting of zircon within calc-silicate alteration. A) Photomicrograph in plane light of zircon within K-feldspar of calc-silicate alteration from Santoy 8 at 20 x magnification. B) Photomicrograph of zircon under cross-polarized light. (original in colour)

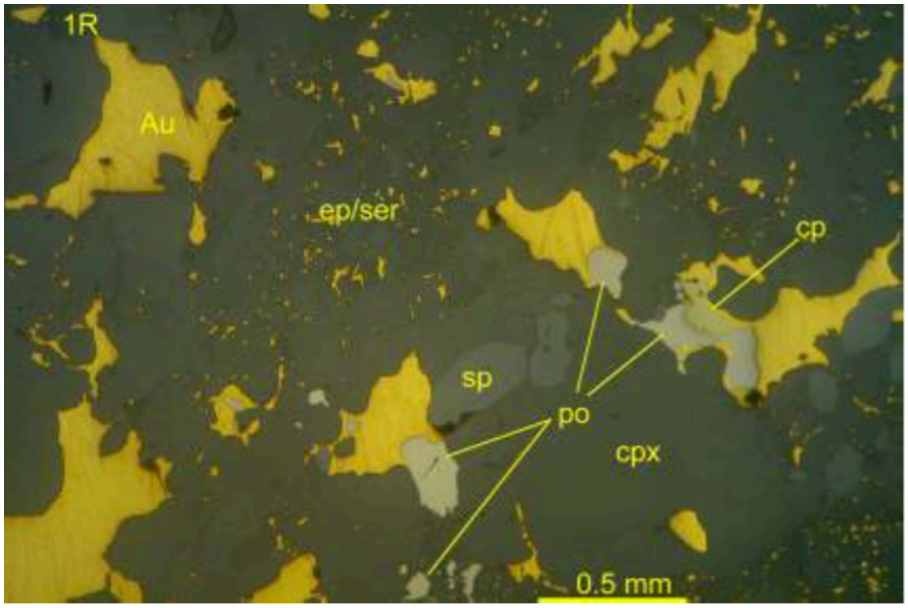

Figure 6.4: Santoy 7 calc-silicate alteration. Photomicrograph from Santoy Zone 7 showing high-grade gold mineralization in association with titanite (sp), chalcopyrite (cp), pyrrhotite (po), epidote (ep), sericite (ser) and diopside (cpx). Photograph taken from Claude Resources internal report. (original in colour)

Accessory sulphides are typically less than 5% of the vein modal mineralogy. As shown in Figure 6.1, the quartz veins are commonly mantled by diopside-rich zones that grade outward, incorporating K-feldspar, plagioclase and titanite. Diopside is coarse grained and subhedral to euhedral where relatively undeformed and is locally variably retrograded to fine-grained actinolite needles, as evidenced by reaction rims on crystal margins. Titanite occurs as subhedral to euhedral inclusions within the diopside at the center of the quartz veins; however, its abundance increases and becomes more anhedral to irregular towards vein margins. Pyrrhotite and chalcopyrite are commonly intermingled, with large concentrations forming in dilatant zones formed by the boudinage of the calc-silicate host. Free gold is associated with Bi-sulphuro tellurides and commonly occurs intergrown with diopside, quartz, actinolite, and on the margins of highly sheared wall rock slivers incorporated into these veins.

6.3 Paragenetic sequence

A paragenetic sequence for petrographic samples was created for the vein and alteration assemblages and is shown in Figure 6.5. The sequence was described in three stages that include, mineralization, retrogression, and late fracturing.

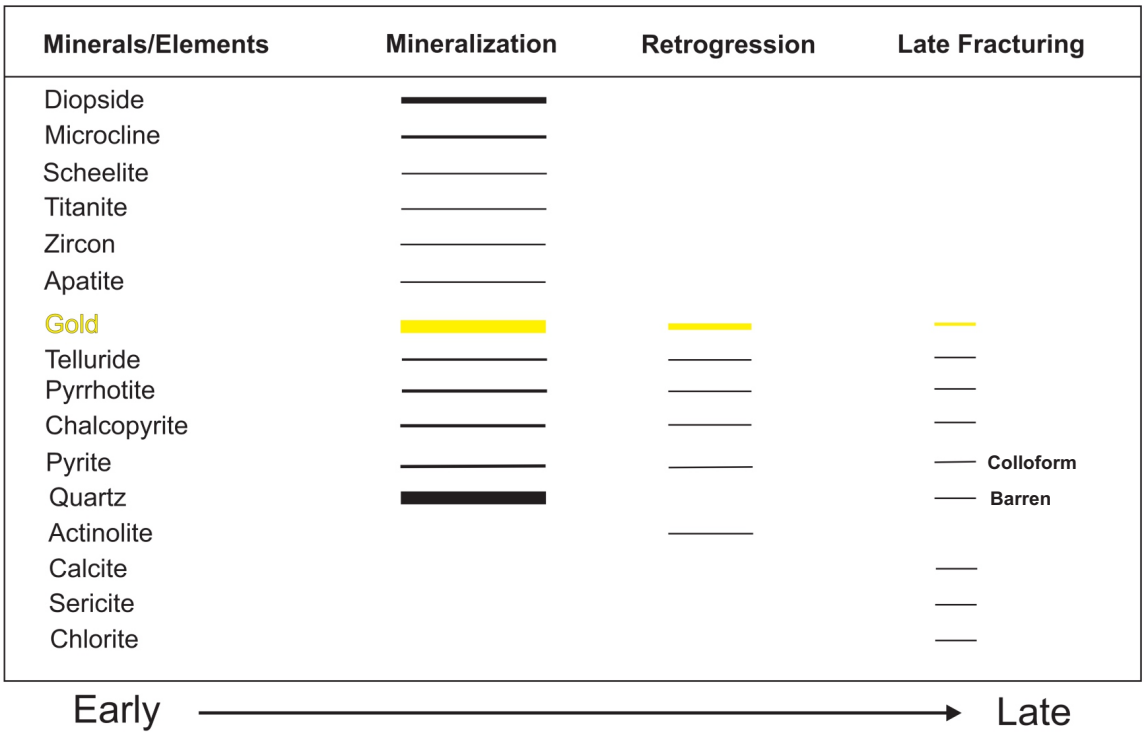

Figure 6.5: Paragenetic sequence of ore/alteration mineral formation. (original in colour)

The "mineralization phase" includes the quartz veins and calc-silicate alteration as well as associated sulphides and accessory minerals (zircon, titanite, apatite). Sulphides within the ore assemblage are much less competent than the host rocks that encompass them. Due to this, the sulphides deform passively and are preferentially concentrated within the calc-silicate phase for two primary reasons:

1. The calc-silicate alteration assemblage and gold were introduced synchronously with the sulphide phases.
2. The competent nature of the calc-silicate minerals, and the tendency of this assemblage to boudinage and fracture during deformation allowed the sulphides

to flow into dilatant zones created at boudin necks, fractures, fault planes, and fold hinges (Figure 6.6).

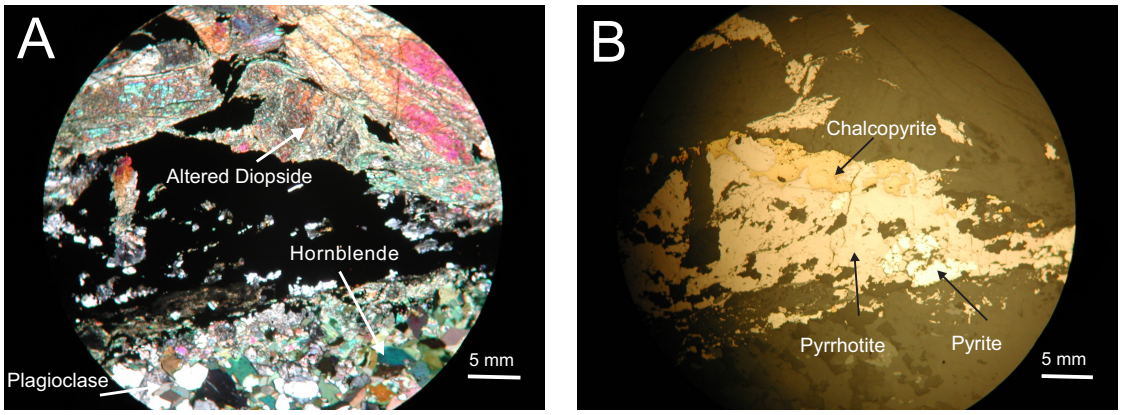

Figure 6.6: Remobilized sulphides. A) Photomicrograph of sample in crossed polarized light of altered diopside and amphibolite wall rock surrounding opaque sulphides. B) Photomicrograph in reflected light of remobilized chalcopyrite, pyrrhotite, and pyrite. (original in colour)

Since sulphide phases have likely migrated from their original textural setting, there is some uncertainty in determining the paragenetic relationships between sulphide minerals. However, textural evidence of gold along with pyrrhotite, and chalcopyrite indicates that they were introduced synchronously with the main mineralization event/calc-silicate assemblage and were redistributed within the assemblage by continued deformation in an active structure and subsequent deformational events. This remobilization would have been more than capable of localizing auriferous sulphides and influencing gold grades within the mine. High-grade plunges of auriferous sulphide shoots could be expected to form perpendicular to the main stretching lineation at an orientation of (27→134^{o}), though this mechanism was not recognized during the study.

The "Retrogession phase" is associated with the growth of reaction rims of actinolite on diopside crystal margins and the inferred minor remobilization of gold and sulphide phases. Finally the "Late Fracturing phase" includes remobilization of sulphides and gold into late brittle fractures and is closely associated with both sericite and chlorite. Pyrite associated with this phase is commonly colloform texture and late quartz veins associated with brittle faulting (e.g., Section 5.3.1) are barren.

6.4 Similar deposits

The structural relationships presented in the preceding chapters (foliation parallel veins) as well as a calc-silicate alteration assemblage hosted in amphibolite-facies rocks at Santoy is atypical of many orogenic gold deposits and other examples of this within the Flin Flon/Glennie domains have not been reported. One other such deposit (the Chalice gold deposit) located in the Yilgarn craton of Western Australia (Bucci et al., 2002) is remarkably similar, albeit hosted in Archean age amphibolite facies rocks. The main-stage mineralization in the latter is characterised by foliation parallel (S_1) veins developed during an asymmetric (non-coaxial) F_2 folding event (Bucci et al., 2002). High-grade ore shoots plunge parallel to the F_2 fold axis and were interpreted to have formed during syn- to late-D_2. The bulk of the mineralization at Chalice as associated with an alteration assemblage of quartz, albite, diopside, titanite, garnet, and pyrrhotite with trace scheelite, pyrite, magnetite, chalcopyrite and rare calcite as well as apatite. The presence of garnet indicates that this alteration assemblage may have formed under somewhat higher-pressure conditions than the Santoy deposits. Age dating of the titanite within this assemblage using SHRIMP II indicated that the S_1 parallel gold bearing veins developed under broadly post-peak metamorphic conditions (Bucci et al., 2004).

6.5 Summary and conclusions

Petrographic analysis, as well as macroscopic observations of the ore/alteration assemblage, indicate that the gold (and associated sulphides) were introduced synchronously with quartz veining. At the same time, the interaction of the mineralizing fluids with the amphibolitic/metavolcanic wallrock produced a distinctive calc-silicate alteration assemblage marginal to the auriferous quartz veins. Ongoing deformation (D_3) within the Santoy shear zone continued after the emplacement of the veins, causing remobilization of some of the gold and sulphide minerals into dilatant zones within the calc-silicate assemblage. Subsequent remobilization is associated with retrogression and the development of actinolite reaction rims on the margins of diopside crystals. Finally, a late fracturing/faulting phase is associated with the remobilization of gold and sulphides into discrete brittle structures. Similar deposits, (i.e., Chalice gold deposit) are relatively rare, however, the strong relationship between calc-silciate alteration and mineralization was also asserted in that case. The occurrence of zircon and titanite within the alteration assemblage at Santoy allowed us to attempt to date the alteration assemblage and in turn gold mineralization. The results of this analysis are presented in Chapter 7.

CHAPTER 7

GEOCHRONOLOGY

7.1 Introduction

The geochronological component of this study was undertaken at the University of Toronto, Jack Satterly Geochronology Laboratory. The author assisted with sample preparation and analysis in a two-week period in December 2013 under the supervision and guidance of Dr. M. Hamilton. Five samples were chosen with the goal of providing further geochronological constraint on:

1. The timing of deformation and plutonism in this region and how it relates to the structural development of the Santoy shear zone.
2. The timing of alteration and mineralization within this system.

The isotope dilution - thermal ionization mass spectrometry (ID-TIMS) method was chosen for this study because of the number of closely spaced tectonic and plutonic events within the Glennie domain. This method provides age dates precise enough to provide more direct geochronological constraints on timing of events that have largely been derived elsewhere in the Glennie domain (Figure 7.1).

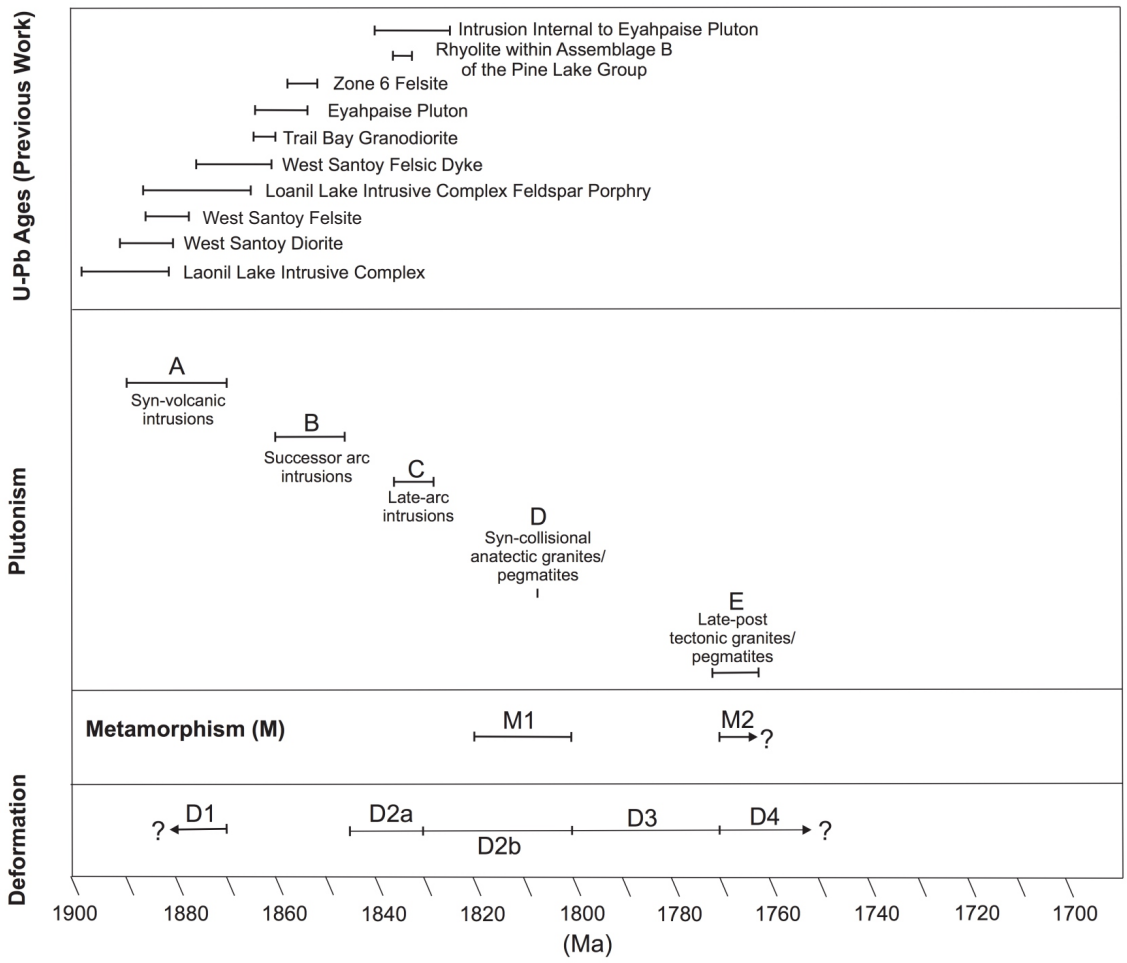

Figure 7.1: Previous U-Pb ages in the region. Age ranges for plutonic phases A-E taken from Saskatchewan Geological Survey (2003). Individual ages and associated references are included in Appendix B. Metamorphic ages are reported from Schneider et al. (2007) and Durocher et al. (2001). Deformation ages are reported from Ashton et al. (2005).

7.2 Sample selection and rationale

Sample sites were selected carefully in order to collect around 25 kg of fresh rock. Care was taken to trim any weathered surfaces in the field.

Sample: SAN C12 GC2- Lizard Lake pluton (UTM 600031E, 6169532N)

The southernmost known extent of the Santoy shear system and Santoy 8 East orebody, occurs adjacent to and within the contact of this tonalitic plutonic body and mafic amphibolites of Assemblage A. The pluton is folded with and contains deformed veins/pods of Santoy 8 East and the calc-silicate assemblage indicating that it predates gold mineralization. It also contains xenoliths of the mafic amphibolite indicating that it post-dates mafic volcanism. The author collected this sample during the summer of 2012 with assistance from Branden Bayda. This age will help constrain the maximum age for the Santoy shear zone and the gold mineralization hosted therein.

Sample: SAN C12 GC3-Tonalite dyke Santoy 8A subsurface (UTM 599706E, 6169688N)

As mentioned and reported in Chapter 5, ore zones within the deposit exhibit a close spatial relationship with tonalitic-dioritic dykes. The author collected this sample during the summer of 2012 within 16L 463 ADR of the Santoy 8A mine. This sample was collected in order to establish the age of the dykes and their overall position in the structural-tectonic evolution of the region. In addition, the age determination will test whether or not these dykes and the Lizard Lake pluton are temporally and possibly genetically related.

Sample: SAN C12 GC4- Packman Lake pluton (UTM 599425E, 6169271N)

This plutonic body is approximately 2 km in width and 7.5 km in length and is a well exposed S>L tectonite with hornblende defining the S_2 foliation and biotite defining an overprinting S_3 axial planar foliation. The moderately north-plunging L_3 mineral lineation is defined by hornblende and biotite. Xenoliths of the mafic amphibolite, are flattened and foliated along the S_2 foliation plane. The pluton typically weathers rusty-pink whereas fresh surfaces are salmon pink. Petrographic study indicates that it is composed of approximately 45-50% potassium feldspar (microcline), 20-25% hornblende, 6-10% plagioclase, 10-15% quartz, 5-10% biotite as well as accessory apatite, zircon and magnetite, constraining it to be of quartz syenite to syeno-granitic in composition (Streckeisen, 1976) (Figure 7.2). Quartz displays undulatory extinction, deformation lamellae, and deformation bands as well as subgrain development and commonly forms myrmekitic intergrowths with potassium feldspar. The author collected this sample during the summer of 2013 with assistance from Branden Bayda. Map analysis and fieldwork discussed in Chapter 3 indicates that the Packman Lake pluton greatly influenced the orientation and deformation of the Carruthers Lake synform, Santoy shear zone, and deposits contained therein. Structural relationships suggest that this pluton acted as a buttress during progressive D_3 deformation, such that the S_2 foliation and regional D_3 fold axial traces warped around the body. The age of this pluton may provide a maximum age for the development of this flexure.

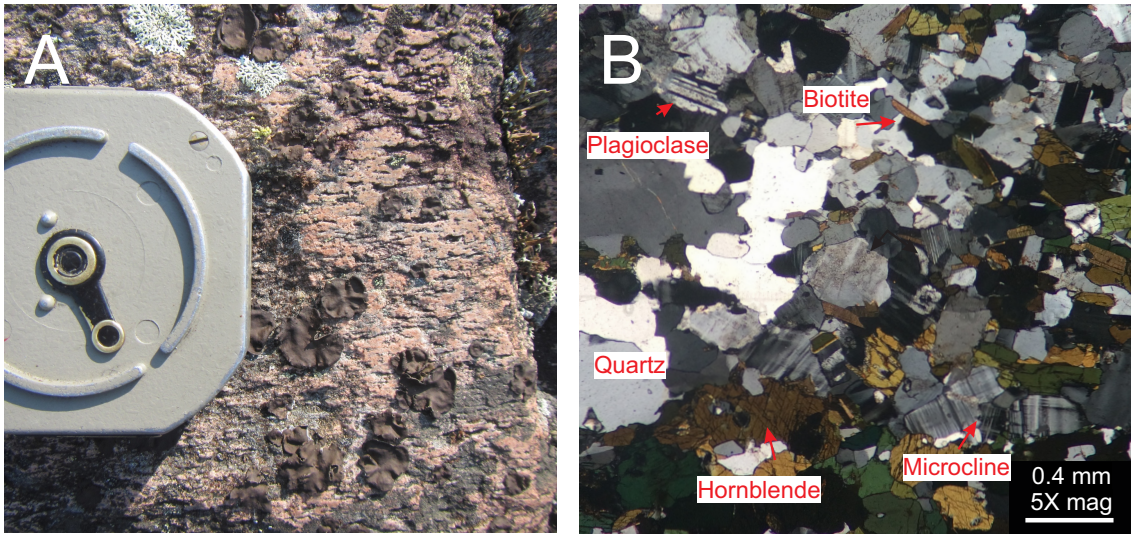

Figure 7.2: The Packman Lake pluton geochronology sample. A) Representative outcrop photo of the Packman Lake pluton. B) Photomicrograph in crossed polarized light showing mineralogy of the pluton. (original in colour)

Sample SAN C12 GC1- Calc-silicate alteration (UTM 599706E, 6169688N)

Calc-silicate alteration is a characteristic feature of the auriferous Santoy shear zone and as discussed in Chapter 6, petrographic relationships indicate that this alteration developed synchronously with gold mineralization. Accordingly, it was reasoned that titanite and zircon found within the assemblage should provide an accurate estimate of the timing of mineralization within the Santoy shear zone (Figure 7.3). A representative thin section of this sample includes 15% hornblende, 35% diopside, 15% quartz, 25% plagioclase and 10% K-feldspar, with approximately 1% titanite and trace calcite. The titanite crystals are sub-idioblastic to idioblastic and 1-2 mm in length.

Figure 7.3: Quartz veins and calc-silicate alteration geochronology sample. This sample was collected during the summer of 2012 by the author and Dr. K. Bethune. (original in colour)

Sample: SAN C12 GC5- Beryliferous granitic pegmatite dyke (UTM 599706E, 6169688N)

This granitic pegmatite crosscuts auriferous ore zones of the Santoy shear zone and was sampled in order to place an upper limit (i.e., minimum age) on the timing of gold mineralization (Figure 5.13). It is approximately 3 m in width and has several textural phases including a fine-grained phase, described below, as well as a megacrystic phase, in which several large beryl crystals of approximately 5 cm in length were observed. The dyke is weakly/gently folded and contains a conspicuous F_3 axial planar cleavage defined by flattened quartz and feldspars. The pegmatites are therefore interpreted to have been emplaced synchronous with D_3 deformation. The pegmatites are also unmineralized indicating that the main stage of gold mineralization had ceased before the end of D_3 deformation. One thin section was made from the fine-grained portion of a beryliferous granitic pegmatite cutting the auriferous ore zone at Santoy 8 21L 457 ADR. It is composed of approximately 40% potassium feldspar (microcline), 30% quartz, 25% plagioclase, 3% garnet, 1% muscovite as well as 1% biotite ± beryl ± tourmaline and accessory zircon. The garnet is anhedral and displays growth zonation with darker cores than rims. The microcline displays classic tartan twinning and is commonly myrmekitically intergrown with quartz. Plagioclase is variably altered to sericite and also very commonly forms myrmekititc intergrowths with quartz and displays mechanical twinning. Quartz displays undulatory extinction, deformation bands, and highly irregular grain boundaries with subgrain formation (Figure 7.4).

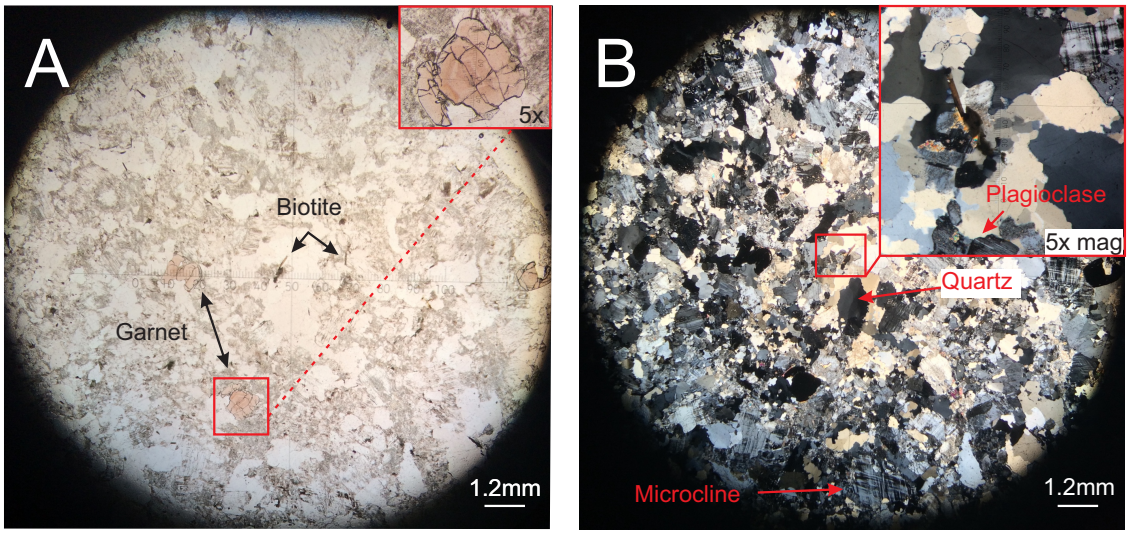

Figure 7.4: Photomicrographs of late beryliferous granitic pegmatite dykes. A) Photomicrograph under plane polarized light showing zonation within garnet crystals. B) Photomicrograph under crossed polarized light showing quartz with undulatory extinction, deformation bands, and highly irregular grain boundaries with subgrain formation. (original in colour)

7.3 Analytical methods

Rock samples were processed in the Jack Satterly Geochronology Lab at the University of Toronto. Conventional crushing and grinding techniques (jaw crusher and disc mill) were employed, followed by the use of a Wilfley™ table to obtain initial heavy mineral concentrates, and finally by Frantz magnetic and methylene iodide heavy-liquid separations.

Hand-picking of the best quality zircon and titanite, (i.e., grains that were as free as possible of cracks, alteration, inclusions, and any optical evidence of cores or overgrowths), occurred under ethanol using a binocular microscope. They were then photographed and analyzed using conventional isotope dilution - thermal ionization mass spectrometry (ID-TIMS) methods. Zircon crystals were pre-treated with a chemical abrasion procedure to remove high U, radiation-damaged and altered zones that may have

lost Pb. This "CA-TIMS" procedure is modified from that proposed by Mattinson (2005), and involved annealing at 1000°C for approximately 48 hours to partially repair radiation damage, followed by leaching in Teflon vessels using a dilute mixture of HF:HNO_3 for 6 hours at 200°C. Final weight estimates were made from a digital measurement of grain dimensions and the mineral's density. The final zircon grains selected for analysis were washed on parafilm with nitric acid, rinsed with ultraclean water and acetone, and loaded into Teflon dissolution vessels with ~0.10 ml concentrated HF along with a mixed ^{205}Pb – ^{235}U isotopic tracer solution (Krogh, 1973). Zircon dissolution occurred over four days at 195°C, followed by re-dissolution in ~0.15 ml of 3N HCl. Titanite was dissolved in Savillex capsules at ~80°C with similar volumes of HF and HNO_3. U and Pb were isolated from the zircon and titanite solutions using 50 µl anion exchange columns using HCl and HBr, respectively. Final volumes were then dried down with phosphoric acid and subsequently loaded with silica gel onto outgassed rhenium filaments.

The isotopic compositions of Pb and U were measured using a single Daly collector with a pulse counting detector on a solid source VG354 mass spectrometer. A detector mass discrimination of 0.053% per atomic mass unit (AMU) and a dead time of 20 nsec were employed for Daly detector measurements. Daly characteristics were monitored using the SRM982 Pb standard. A thermal source mass discrimination correction of 0.1% per atomic mass unit was applied for both Pb and U. The assigned laboratory blank for U was 0.2 pg, while that for Pb is routinely measured below 1 pg. Error estimates were calculated by propagating known sources of analytical uncertainty for each analysis including within-run ratio variability, uncertainty in the fractionation

correction, and uncertainties in the isotopic composition of laboratory blank. Uncertainties for the ID-TIMS data are given at the 95% (2σ) confidence level. Initial corrections were made using an in-house data reduction program (UTILAGE). Decay constants used in age calculations are those of Jaffey et al. (1971). Concordia plots and quoted ages were generated using the Microsoft Excel Add-in Isoplot/Ex v. 3.00 of Ludwig (2003).

Table 7.1: U-Pb isotopic data for geochronologic samples

Fraction	Description	Weight (μg)	U (ppm)	Pb^T (pg)	Pb_c (pg)	Th/U	$^{206}Pb/^{204}Pb$	$^{207}Pb/^{235}U$	± 2σ	$^{206}Pb/^{238}U$	± 2σ	Corr. Coeff.	$^{207}Pb/^{206}Pb$	± 2σ	Ages (Ma) $^{206}Pb/^{238}U$	± 2σ	$^{207}Pb/^{235}U$	± 2σ	$^{207}Pb/^{206}Pb$	± 2σ	Disc. (%)
SAN-C12-GC2 - Lizard Lake pluton																					
Z1	1 4:1 slender , clr, cls, el pr	2.0	88	59.93	0.34	0.262	11155	5.26986	0.01246	0.334126	0.000644	0.919072	0.114390	0.000110	1858.4	3.1	1864.0	2.0	1870.3	1.7	0.7
Z2	1 wider el pr with crack	2.4	139	93.79	1.23	0.204	4854	5.30322	0.01383	0.335532	0.000647	0.878993	0.114632	0.000148	1865.1	3.1	1869.4	2.2	1874.1	2.3	0.6
Z3	1 small el pr	0.9	34	11.45	0.46	0.205	1583	5.29914	0.02844	0.335918	0.001292	0.778410	0.114412	0.000387	1867.0	6.2	1868.7	4.6	1870.6	6.1	0.2
Z4	1 long, broken, clr, cls, el pr	1.3	138	47.08	0.68	0.217	4386	5.31634	0.01611	0.336031	0.000854	0.751151	0.114744	0.000232	1867.5	4.1	1871.5	2.6	1875.9	3.6	0.5
Z5	1 4:1 thin, clr, cls, el pr	1.1	63	21.21	1.02	0.207	1344	5.24863	0.03342	0.333105	0.000925	0.676250	0.114278	0.000564	1853.4	4.5	1860.5	5.4	1868.5	8.9	0.9
SAN-C12-GC3 - Tonalite dyke, underground																					
Z1	1 cldy, 2-3:1 pr	0.9	239	81.50	6.20	0.260	841	5.29119	0.03739	0.333099	0.000760	0.673637	0.115207	0.000666	1853.4	3.7	1867.4	6.0	1883.1	10.4	1.8
Z2	1 cldy, 3:1 pr	0.8	130	43.97	0.51	0.251	5396	5.24411	0.01538	0.331818	0.000769	0.884992	0.114623	0.000160	1847.2	3.7	1859.8	2.5	1874.0	2.5	1.6
Z3	1 cldy, 3:1 pr	0.6	63	20.45	0.96	0.178	1387	5.13484	0.02542	0.324638	0.000872	0.706361	0.114716	0.000413	1812.3	4.2	1841.9	4.2	1875.4	6.5	3.9
Z5	1 cldy, small, el pr	0.6	42	7.11	0.35	0.250	1291	5.30478	0.03884	0.335375	0.001960	0.820931	0.114719	0.000480	1864.4	9.5	1869.6	6.3	1875.5	7.5	0.7
Z6	1 cldy, small, el pr	0.5	41	6.41	0.25	0.212	1613	4.82794	0.03202	0.305760	0.001683	0.871369	0.114519	0.000374	1719.8	8.3	1789.8	5.6	1872.3	5.9	9.3
SAN-C12-GC4 - Packman Lake pluton																					
Z1	1 irreg, 3:1 cloudy, altered	0.9	39	11.79	0.60	0.266	1246	4.48824	0.03003	0.295412	0.001094	0.683884	0.110191	0.000547	1668.5	5.4	1728.8	5.6	1802.6	9.0	8.4
Z2	1 irreg, 2:1 cloudy, altered	0.8	21	4.80	0.58	0.106	559	3.50558	0.04103	0.229544	0.001248	0.658223	0.110763	0.001008	1332.1	6.5	1528.5	9.3	1812.0	16.6	29.3
Z3	1 irreg, 3:1 cloudy, altered	0.7	42	5.15	0.42	0.137	808	2.87139	0.02651	0.187973	0.000863	0.671676	0.110789	0.000779	1110.4	4.7	1374.4	7.0	1812.4	12.8	42.1
SAN-C12-GC1 - Calc-silicate Assemblage; Santoy Mine																					
Z1	1 large, cls, sl cldy, brkn pr	2.2	85	50.62	0.32	0.010	10567	4.59558	0.01212	0.310659	0.000691	0.931283	0.107289	0.000106	1743.9	3.4	1748.5	2.2	1753.9	1.8	0.6
Z2	1 small, clr, cls, pr	0.2	71	4.39	0.39	0.098	751	4.75456	0.05246	0.317294	0.002426	0.782449	0.108680	0.000755	1776.5	11.9	1776.9	9.3	1777.4	12.7	0.1
Z4	1 medium, cls, sl cldy 2:1 pr	0.9	34	10.36	0.44	0.123	1562	4.68359	0.02716	0.311403	0.001393	0.679898	0.109083	0.000468	1747.6	6.8	1764.3	4.9	1784.2	7.8	2.3
Z5	1 large, sl cldy, el pr	1.3	83	24.19	0.85	0.018	1925	4.55073	0.01843	0.305321	0.000763	0.692958	0.108100	0.000317	1717.6	3.8	1740.3	3.4	1767.6	5.4	3.2
Z6	1 small cls, sl cldy, pr	0.5	13	3.82	0.26	0.036	995	4.68292	0.05423	0.315858	0.002781	0.822651	0.107529	0.000712	1769.5	13.6	1764.2	9.7	1758.0	12.1	-0.7
Z7	1 small, cls, sl cldy 2:1 pr	0.5	78	23.06	0.21	0.560	6102	12.95038	0.04559	0.512376	0.001653	0.964118	0.183313	0.000174	2666.8	7.0	2676.0	3.3	2683.1	1.6	0.7
T1	1 M@1.7A larger grain	8.1	43	105.01	9.57	0.135	732	4.60371	0.04235	0.309972	0.000801	0.670762	0.107717	0.000831	1740.6	3.9	1749.9	7.7	1761.2	14.1	1.3
T2	1 M@1.7A medium grain	7.4	15	30.89	4.88	0.050	439	4.52173	0.06344	0.306750	0.000837	0.754689	0.106910	0.001295	1724.7	4.1	1735.0	11.7	1747.4	22.3	1.5
T3	1 M@1.7A smaller grain	5.1	12	18.90	3.07	0.160	417	4.60459	0.06867	0.310484	0.000972	0.729072	0.107560	0.001379	1743.1	4.8	1750.1	12.5	1758.5	23.5	1.0
T4	1 M@1.7A smaller grain	5.1	14	21.72	3.49	0.090	428	4.53918	0.07884	0.307554	0.001194	0.678041	0.107042	0.001607	1728.7	5.9	1738.2	14.5	1749.7	27.5	1.4
T5	1 M@1.7A smaller grain	3.0	21	19.04	3.55	0.093	371	4.49342	0.07519	0.303361	0.001005	0.745479	0.107428	0.001552	1708.0	5.0	1729.8	13.9	1756.2	26.5	3.1
T6	1 M@1.0A medium grain	3.9	10	11.65	2.04	0.136	389	4.51556	0.07260	0.306305	0.001184	0.683772	0.106919	0.001469	1722.5	5.8	1733.8	13.4	1747.6	25.3	1.6
T7	1 M@1.0A larger grain	10.1	10	36.78	15.64	0.240	140	4.59170	0.16963	0.307776	0.004342	0.587394	0.108202	0.003342	1729.8	21.4	1747.8	31.0	1769.4	56.8	2.6
T8	1 M@1.0A medium grain	5.0	11	16.26	9.02	0.075	137	4.45250	0.21738	0.302363	0.002033	0.931143	0.106801	0.004567	1703.0	10.1	1722.2	40.9	1745.5	79.3	2.8
SAN-C13-GC5 - Santoy pegmatite																					
Z1	1 clr, cls	0.5	266	279.37	0.66	28.2	3400	1.90748	0.00552	0.130307	0.000250	0.795349	0.106167	0.000190	789.6	1.4	1083.7	1.9	1734.6	3.3	57.8
Z2	1 cloudy white, irreg	0.6	100	31.34	3.17	0.292	637	4.48829	0.04405	0.305843	0.000780	0.667706	0.106434	0.000887	1720.2	3.9	1728.8	8.2	1739.2	15.3	1.2
Z3	1 small, clr, cls	0.4	206	115.35	0.57	26.3	1735	1.08379	0.00470	0.073869	0.000153	0.674442	0.106410	0.000352	459.4	0.9	745.5	2.3	1738.8	6.1	76.1
Z4	1 clr, cls	0.5	350	394.15	0.45	29.4	6795	1.97299	0.00483	0.134657	0.000260	0.854718	0.106266	0.000136	814.4	1.5	1106.3	1.6	1736.3	2.3	56.4

Notes:

All analyzed fractions represent least magnetic, chemically-abraded zircon grains, free of cores or cracks unless stated otherwise, or fresh, clear titanites (without abrasion pretreatment).

Abbreviations: clr - clear; cls - colourless; sl cldy - slightly cloudy; irreg - irregular or anhedral; el - elongate; brkn - broken; pr - prism; M@1.7A and M@1.0A = magnetic fraction for current setting on Frantz separator.

Pb^T is total amount (in picograms) of Pb.

Pb_c is total measured common Pb (in picograms) assuming the isotopic composition of laboratory blank: 206/204 - 18.221; 207/204 - 15.612; 208/204 - 39.360 (errors of 2%).

Pb/U atomic ratios are corrected for spike, fractionation, blank, and, where necessary, initial common Pb; 206Pb/204Pb is corrected for spike and fractionation.

Th/U is model value calculated from radiogenic 208Pb/206Pb ratio and 207Pb/206Pb age, assuming concordance.

Disc. (%) - per cent discordance for the given 207Pb/206Pb age.

Uranium decay constants are from Jaffey et al. (1971).

7.4 Geochronology results

Sample: SAN C12 GC2- Lizard Lake pluton (UTM 600031E, 6169532N)

The Lizard Lake pluton yielded a relatively homogeneous population of elongate zircon prisms and needles. The zircons were clouded, slightly cracked, and some had vestiges of internal zoning with preserved cores (which were avoided). Following chemical abrasion, many crystals were very clouded or only had small traces of clear domains. Five single grain fractions were analyzed and yielded fairly uniform $^{207/206}$Pb ratios that gave ^{207}Pb/^{206}Pb ages ranging from 1868 to 1876 Ma, with only a small amount of discordance (Table 1). Due to Pb-loss for fractions Z1, Z3, and Z5, only the oldest two fractions (Z2 and Z4) were regressed, resulting in an upper intercept age of 1874.6 ± 1.9 Ma (anchored at 0 Ma) (Figure 7.5). The inclusion of one more fraction (Z1, Z3 and Z5) gives a more precise age of 1870.3 ± 1.6 Ma, but may skew the age too low and thus be less accurate. The older 1874.6 ± 1.9 Ma result from fractions (Z2 and Z4) is therefore considered to be the best estimate for the crystallization age of this tonalite.

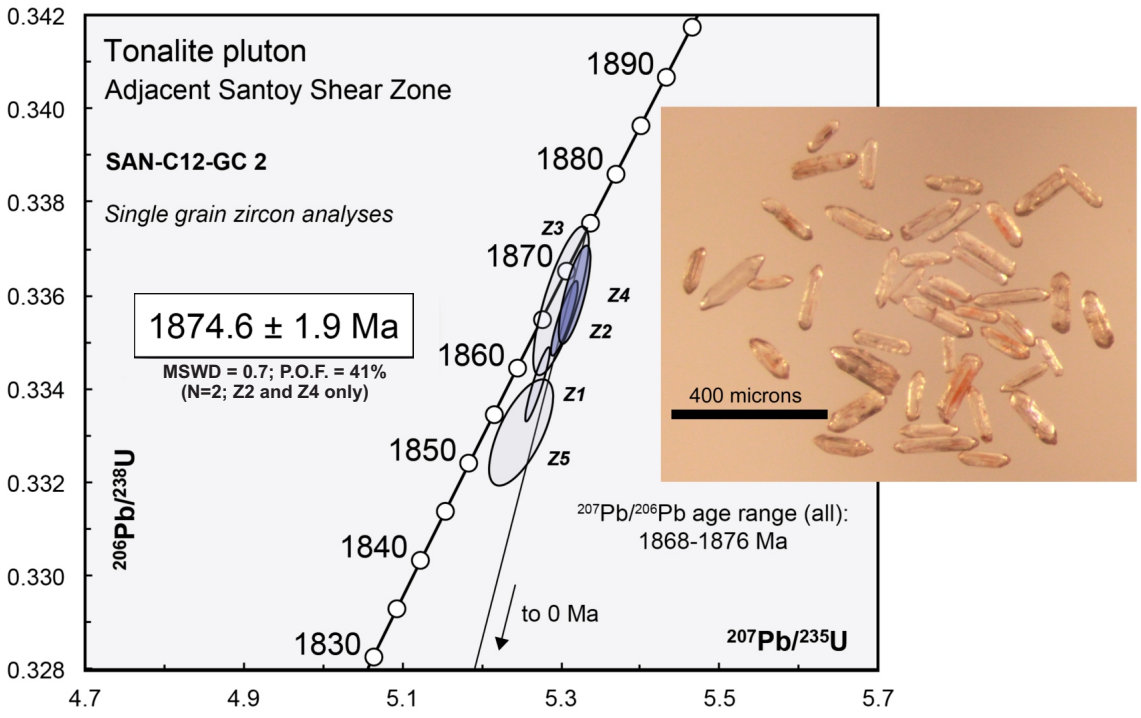

Figure 7.5: Lizard Lake pluton concordia diagram. Z2 and Z4 fractions are included in the regression, resulting in an upper intercept age of 1874.6 ± 1.9 Ma. Photo of the zircon fractions before annealing and chemical abrasion. (original in colour)

Sample: SAN C12 GC3- Tonalite dyke, Santoy 8A subsurface (UTM 599706E, 6169688N)

The tonalite dyke adjacent to the Santoy 8A ore zone yielded a limited number of small, poor quality zircons. A total of six zircon fractions were analyzed, comprising single grains, except for fraction Z6, which consisted of three grains. Fraction Z1 suffered from high common Pb (6 pg) and fraction Z4 was too weak to yield useable data. These fractions were therefore rejected from the final analysis. The remaining four fractions were regressed and yield an upper intercept age of 1874.6 ± 2.9 Ma (lower intercept age = 38 ± 140 Ma) whereas a regression anchored at the origin gives an approximately equal

upper intercept age of 1874.0 ± 2.1 Ma. The former age is considered the most reasonable estimate of the age of crystallization age of the dyke (Figure 7.6).

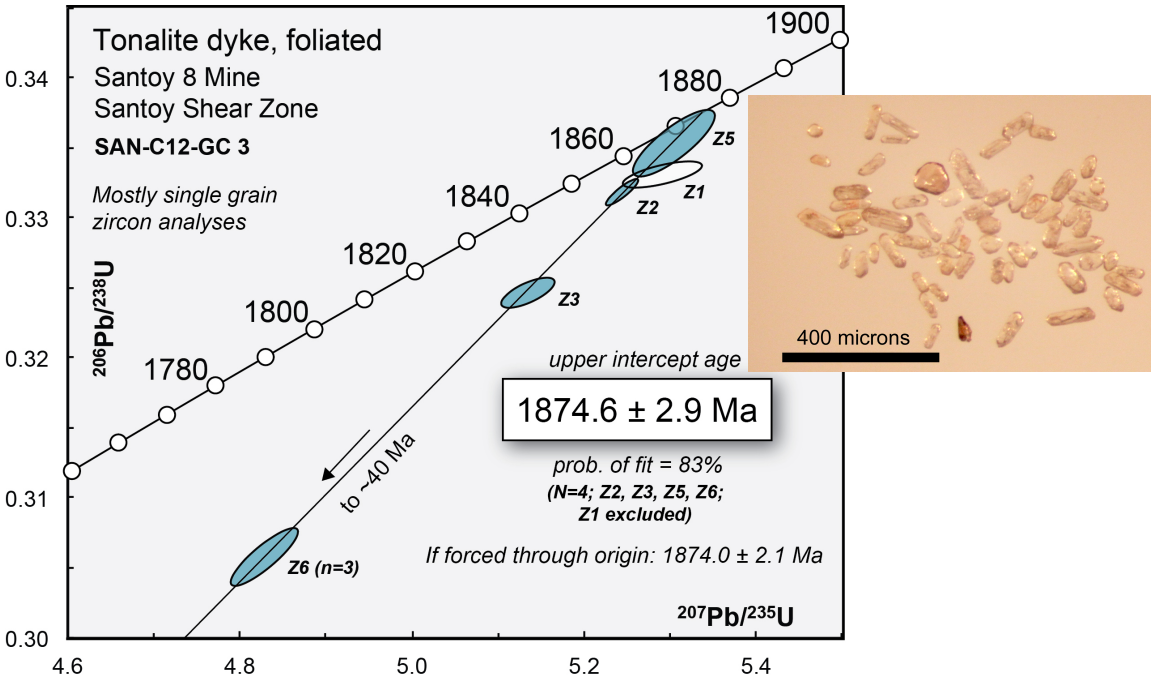

Figure 7.6: Santoy 8A ore zone dyke concordia diagram. Z2, Z3, Z5 and Z6 were regressed and yielded an upper intercept age of 1874.6 ± 2.9 Ma. Photo of the zircon fractions before annealing and chemical abrasion. (original in colour)

Sample: SAN C12 GC4- Packman Lake pluton (UTM 599425E, 6169271N)

This sample of quartz syenite yielded a small but uniform population of ~100 μm, cloudy zircon grains with short prismatic (2:1-3:1) forms. Three of the clearest single grain fractions (Z1, Z2, Z3) were analyzed yielding strongly discordant $^{207}Pb/^{206}Pb$ ages of 1802.6, 1812.0, and 1812.4 Ma respectively (Table 1). A regression through these analyses produces an upper intercept age of 1802 ± 10 Ma, with a negative lower intercept at -33 ± 49 Ma. However, forcing the regression through the origin yields an

upper intercept age of 1806.8 ± 6.6 Ma, and is currently taken as the best estimate of the crystallization age of the quartz syenite pluton (Figure 7.7).

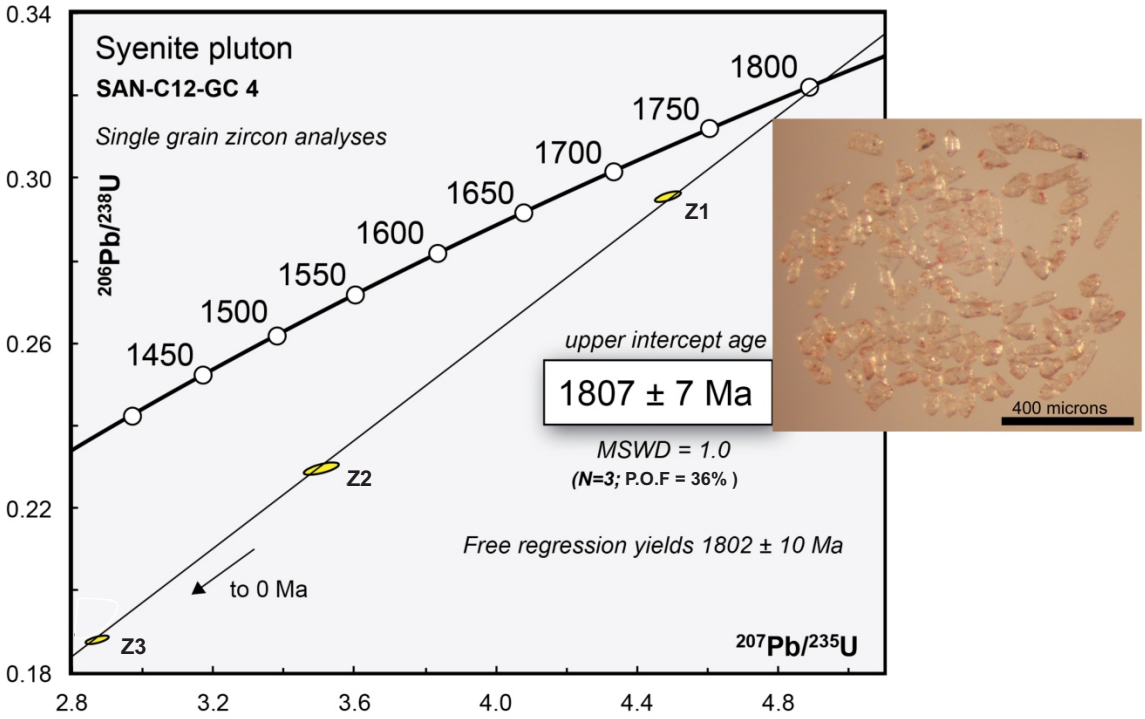

Figure 7.7: Packman Lake pluton concordia diagram. Z1, Z2, and Z3 were regressed and yield an upper intercept age of 1806.8 ± 6.6 Ma. Photo of the zircon fractions before annealing and chemical abrasion. (original in colour)

Sample: SAN C12 GC1- Calc-silicate alteration (UTM 599706E, 6169688N)

As discussed in Chapter 6 (Nature of gold mineralization) the calc-silicate alteration assemblage includes abundant titanite. Crushing and mineral separation yielded plentiful ~100 μm, anhedral, clear titanite grains (Figure 7.8). To our surprise, a population of elongate (3:1, length:breadth) zircon grains were also recovered but both the quality and morphology of the zircons were quite variable; however, the clearest, least cloudy and most prismatic forms were chosen. As these had not been detected under the microscope,

SEM analysis was performed and revealed that the zircon, along with diopside texturally sits within the titanite crystals (Figure 7.9). The U-Pb results yielded from the titanite are fairly straightforward. For example, a total of 8 single-grain titanite fractions were analyzed and were regressed yielding an intercept age 1755.5 ± 8.4 Ma, with a MSWD of 0.3 and a probability of fit of 95% (Figure 7.8). In contrast, the U-Pb results from the zircon within the same assemblage are more variable. Fraction Z3 was too weak to yield usable data; however, three single-grain fractions, (Z2, Z4 and Z5) yielded distinctly older $^{207}Pb/^{206}Pb$ ages than those derived from the titanite. Of these, the least discordant, (Z2 and Z4) yielded $^{207}Pb/^{206}Pb$ ages of ca.1777 Ma and ca.1784 Ma respectively and are characterized by Th/U ratios that are higher than the others (~0.10, 0.12). Regressing the two analyses together yields an age of 1782 ± 6.5 Ma with an MSWD of 0.83 and a probability of fit of 36%. In contrast, Z1 is only 0.65% discordant, and has a much younger $^{207}Pb/^{206}Pb$ age of 1754 ± 1.8 Ma, and a Th/U ratio of only 0.01. This age is identical within error of the age of the titanite upper intercept age of 1755.5 ± 8.4 Ma. Zircon fraction (Z6) is slightly reverse discordant but has a similarly young $^{207}Pb/^{206}Pb$ age (1758 Ma) and low Th/U ratio (0.04). Zircon fraction Z5 is the most discordant with a low Th/U ratio (0.02) and an intermediate $^{207}Pb/^{206}Pb$ age (1767 Ma) (Figure 7.10). There is a seventh zircon analysis, (Z7), but this grain yielded a Neoarchean age 2683.1 ± 1.6 Ma (0.7% discordant). As this age was not reproduced, we are highly suspicious that it indicates contamination during sample processing; it was therefore not considered further in this analysis.

As discussed above, the age determined from the titanites yielded an upper intercept age 1755.5 ± 8.4 Ma (2s), with a good MSWD of 0.3 and a probability of fit of 95%. The

information yielded from the zircons is less straightforward and seem to indicate two zircon populations of different ages and U/Th ratios. The agreement of the younger zircon age in the same sample (Z1 and Z6) along with corroborating textural evidence of growth contemporaneous with gold mineralization (thin section analysis and SEM) gives high confidence that (1755.5 ± 8.4 Ma) is the age of the calc-silicate assemblage and gold mineralization. The interpretation of the older (~1782 ± 6.5 Ma) zircon population that is associated with higher U/Th ratios (Z2 and Z4) is more enigmatic and may represent evidence for growth during the M_2 metamorphic event thought to have been caused by rapid uplift and cooling at ca. 1770 Ma (Schneider et al., 2007).

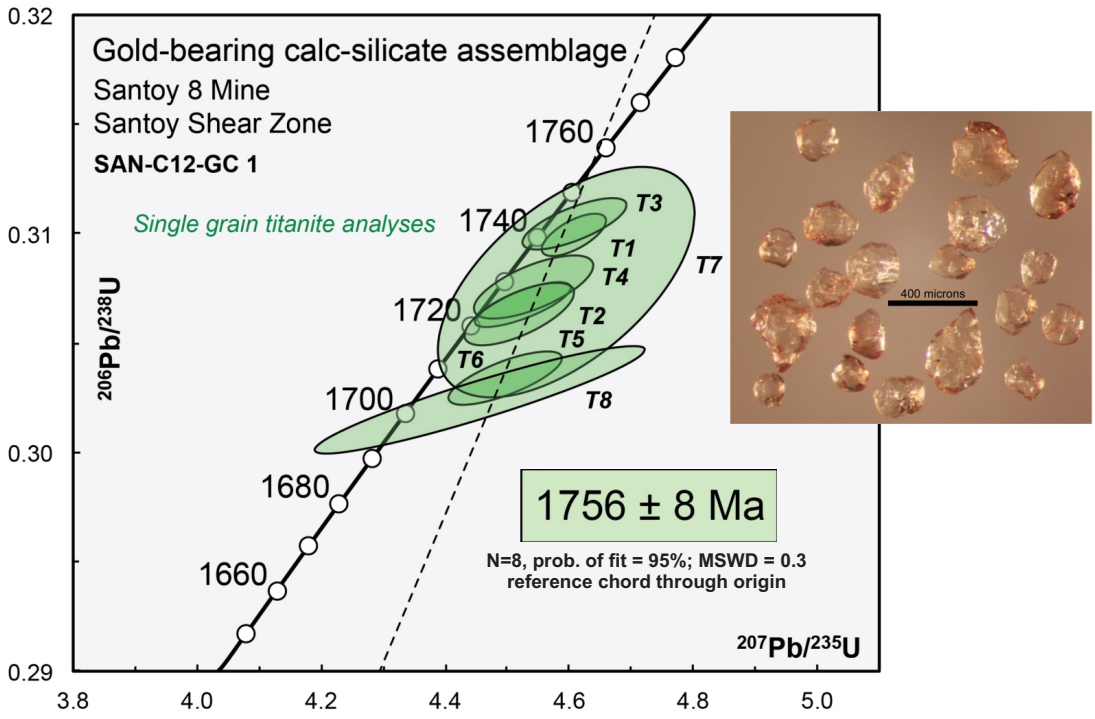

Figure 7.8: Calc-silicate alteration: titanite concordia diagram. T1-T8 were regressed and produced an upper intercept age of 1755.5 ± 8.4 Ma. Photo of titanite fractions before dissolution. (original in colour)

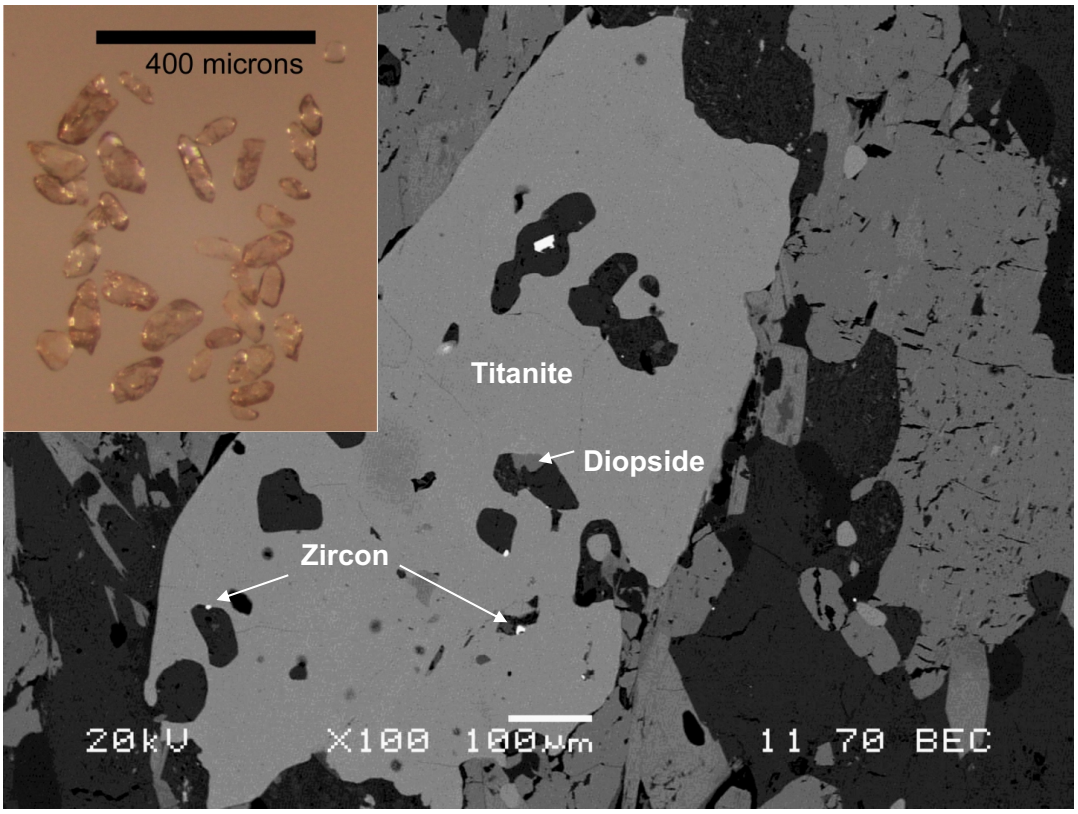

Figure 7.9: Textural setting of zircon within calc-silcate alteration. SEM-photomicrograph of zircon and diopside inclusions within titanite. Upper-left: Photo of the zircon fractions from the calc-silicate before annealing and chemical abrasion. (original in colour)

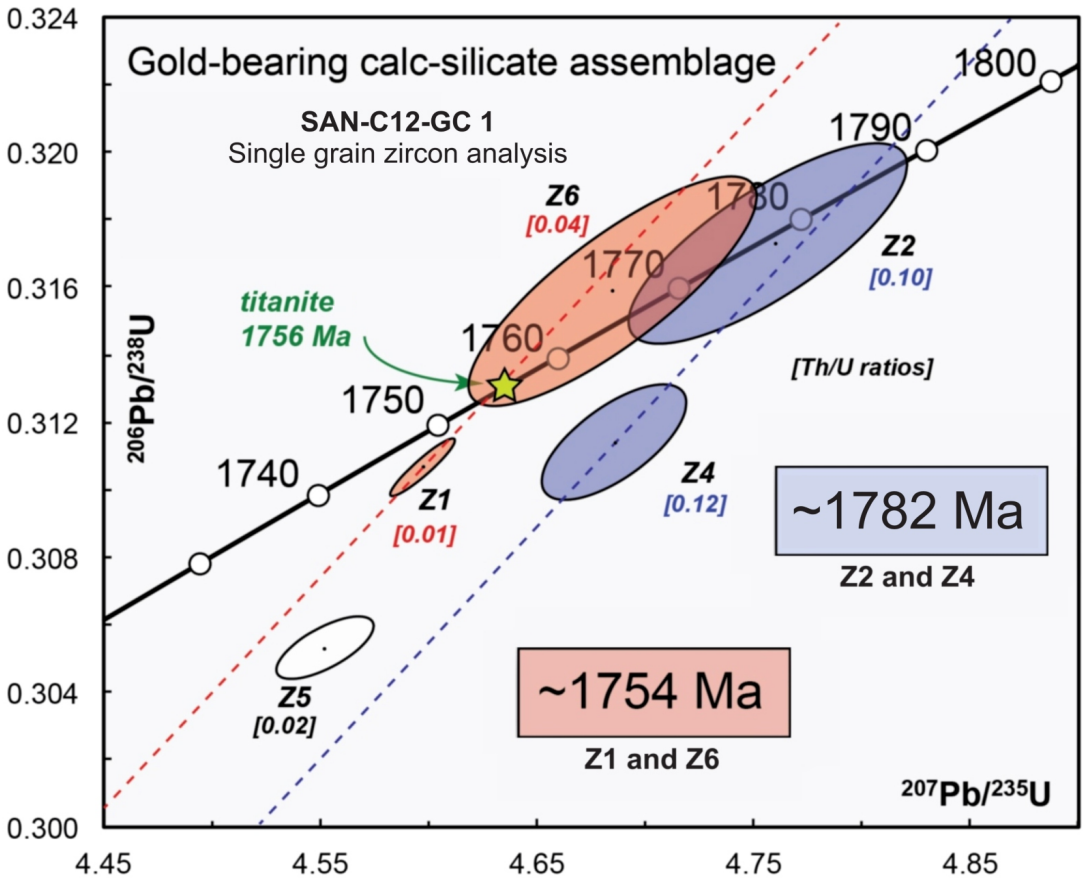

Figure 7.10: Calc-silicate alteration: zircon concordia diagram. Z1 and Z6 were regressed as well as Z2 and Z4 producing upper intercept ages of 1754 ± 1.8 Ma and 1782 ± 6.5 Ma respectively. (original in colour)

Sample: SAN C12 GC5 Beryliferous granitic pegmatite dyke (UTM 599706E, 6169688N)

Four of the clearest, well formed, prismatic grains (~100 μm long) that were free of cloudiness and fractures were selected for analysis. The data ranges between 1.3% (Z2) and 76.1% (Z3) discordant however all four fractions yield very similar $^{207}Pb/^{206}Pb$ ages, near 1735 Ma. A free regression through these four analysis produces an upper intercept age of 1734.3 ± 5 Ma, and a negative lower intercept at -2.3 ± 6.1 Ma, with an MSWD = 0.64 and a probability of fit of 53%. However, forcing the regression through the origin

yields an upper intercept age of 1736.1 ± 1.9 Ma, with an MSWD = 0.6 and a probability of fit of 61% and is interpreted as the crystallization age of this pegmatite (Figure 7.11).

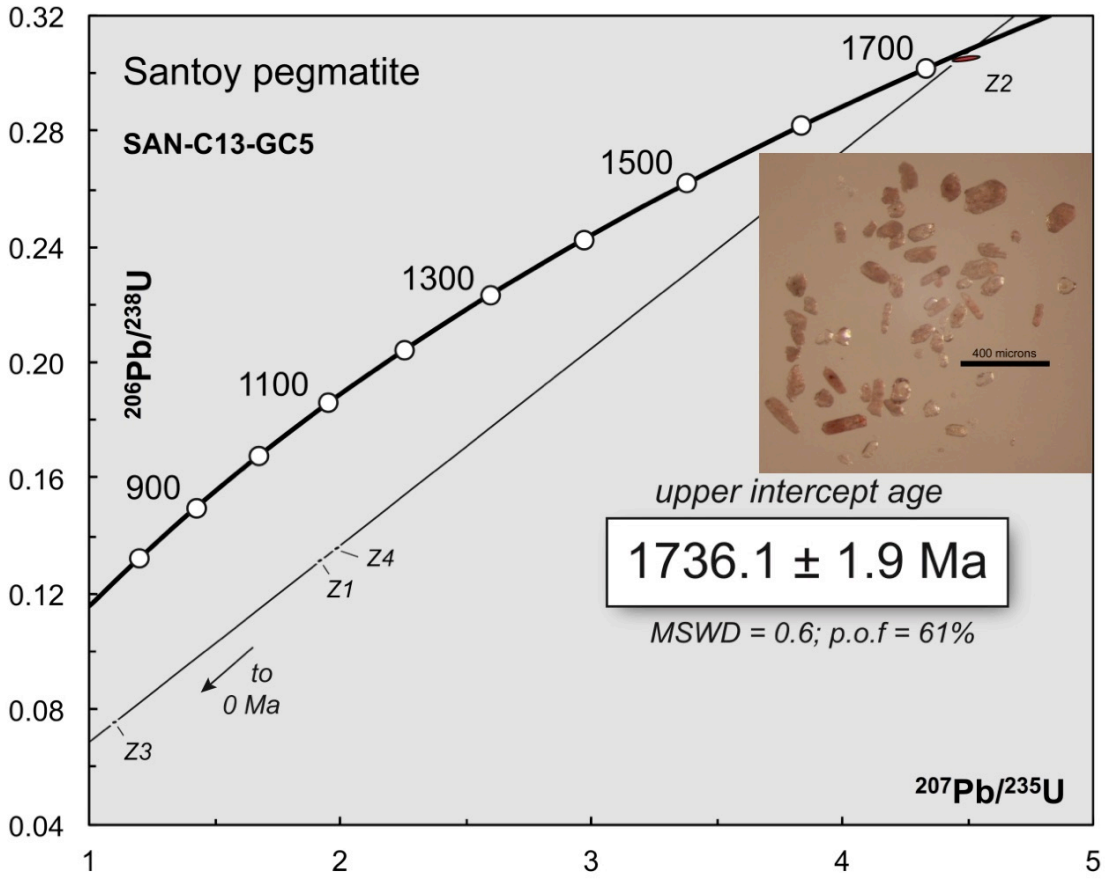

Figure 7.11: Beryliferous pegmatite concordia diagram. Z1-Z4 was regressed and produced an upper intercept age of 1736.1 ± 1.9 Ma. Photo of the zircon fractions before annealing and chemical abrasion. (original in colour)

7.5 Summary and conclusions

The geochronologic component of this study yielded some important information/conclusions about the study area. Each sample will be discussed briefly below as well as its significance with respect to regional and local geology, as summarized in Figure 7.12.

1. The Lizard Lake pluton yielded an age of 1874.6 ± 1.9 Ma. As discussed above, plutonism in the Glennie domain is episodic and is divided into five main suites. The age of this pluton therefore corresponds to suite A (syn-volcanic arc intrusions) emplaced during the amalgamation of the Flin Flon-Glennie Complex. This age also provides a maximum age constraint for the Santoy shear zone and the gold mineralization hosted therein (Figure 7.12).
2. The tonalite dyke from the Santoy 8A subsurface yielded an age of 1874.6 ± 2.9 Ma and also corresponds to suite A (syn-volcanic arc intrusions) (Figure 7.12). This age is identical within error to the age for the Lizard Lake pluton discussed above, and strongly suggests that the dyke is a magmatically related offshoot.
3. The 1807 ± 7 Ma age for the Packman Lake pluton indicates that it belongs to suite D, syn-collisional anatectic granites and pegmatites formed during peak metamorphism in the Glennie domain (Figure 7.12). It also indicates, that warping/flexuring of the Carruthers Lake synform occurred after ca. 1807 Ma.
4. Petrographic and macroscopic observations indicate that calc-silicate alteration is synchronous with quartz vein development and gold mineralization hosted therein. Independent U-Pb titanite and zircon ages (Z1 and Z6 Fraction) indicate that alteration and mineralization occurred at ~1755.5 ± 8.4 Ma (Figure 7.12). The older (~1782 ± 6.5 Ma) zircon population that is associated with higher U/Th ratios (Z2 and Z4) may represent evidence for growth during the M_2 metamorphic event. The large amount of time between pluton/dyke emplacement and alteration (potentially ~120 Ma) suggests that the relationship between the dykes and ore is a structural one; that is, they are not genetically related to one another. This

dispels the notion that the gold has a syngenetic origin with the plutonic rocks in the area.

5. The syn-D_3 beryliferous pegmatite age of 1736 ± 1.9 Ma provides a minimum age of gold mineralization for the Santoy deposits. This age is within error of and confirms a previous ~1727 ± 17 Ma zircon age (e.g., Durocher et al., 2001) from a pegmatite which crosscuts Santoy Zone 3. The significance of this age was never fully interpreted due to zircon inheritance and lack of reproducible zircons. This age also confirms that Durocher (1997) estimate for mineralization in this region of ~1715 Ma is not valid. As mentioned above, the results from dating titanite and zircon of the alteration assemblage indicate that mineralization is ~ 40 m.y. older. Elliot (1995) dated a pegmatite dyke that was deformed during the final stages of ductile movement in the Tabbernor fault to 1737 ± 2 Ma and inferred that this represents a minimum age for ductile (sinistral) movement. This also suggests that these pegmatites are recording the final stages of D_3 deformation (~1800-1736 Ma) in the northern Glennie domain that were previously thought to be around 1800-1770 Ma (Ashton et al., 2005). This extends known tectonic activity in the Flin Flon-Glennie complex by a large margin (Figure 7.12).

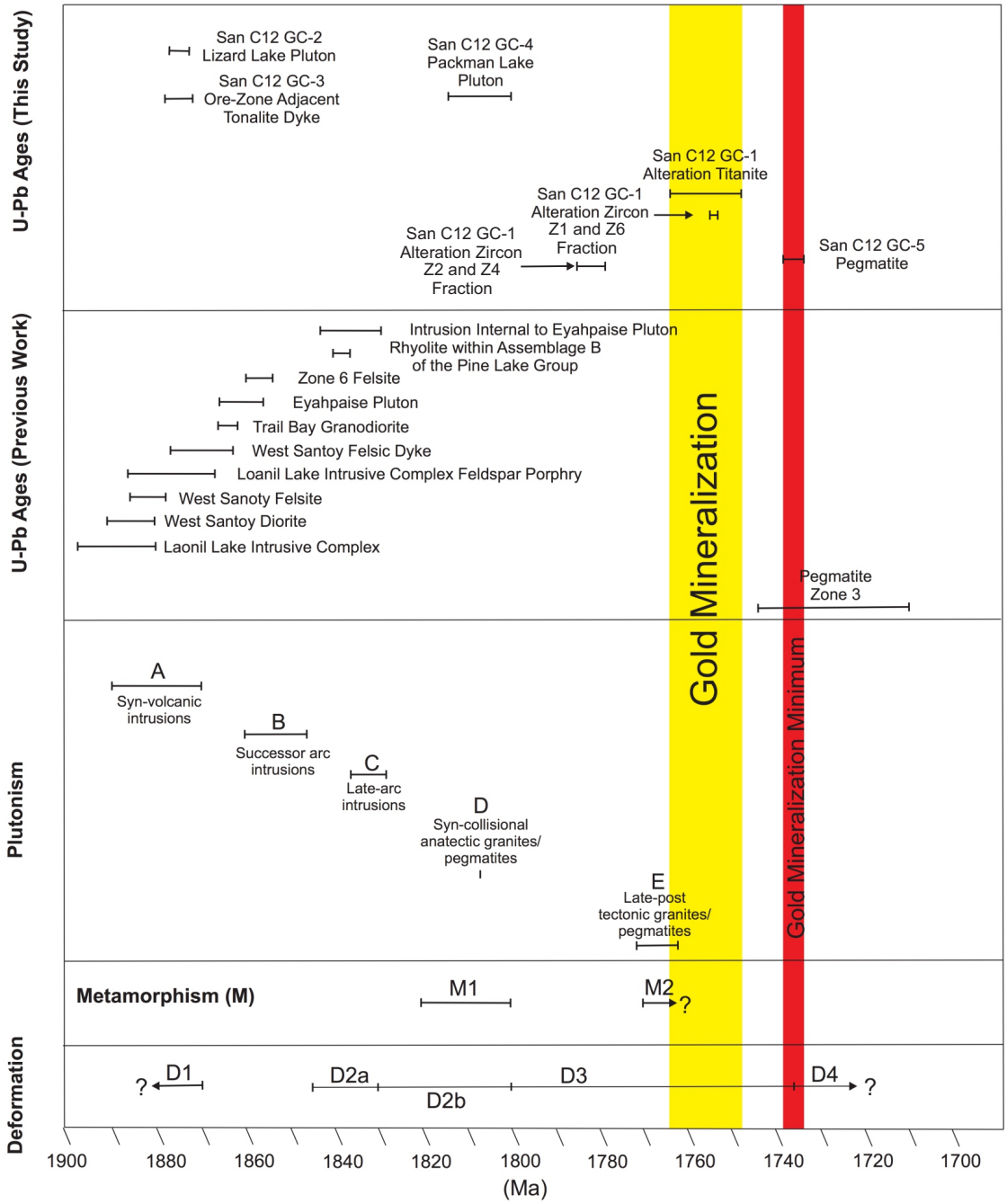

Figure 7.12: Summary of age constraints for this study. (original in colour)

CHAPTER 8

KINEMATIC & DYNAMIC MODEL

8.1 Introduction

In Chapter 5 observations of attenuated layers and lenses of quartz and calc-silicate that have been boudinaged along the L_3 lineation as well as diopside porphyroclasts that display symmetrical Φ type geometries were reported. The boudinage and lack of asymmetry point to a strong component of flattening (or normal stress) within the shear zone, however there is also a significant component of shear stress and non-coaxial deformation. A major curiosity with regard to this relationship is how the fault-fill quartz veins and calc-silicate alteration came to be emplaced in such a potentially unfavourable orientation (relative to $\sigma 1$) during D_3 deformation. The following discussion combines field and structural observations from within and well outside of the Santoy shear zone along with the petrographic relationships and geochronological data described in previous chapters to develop an updated step-by-step model for the development of the Santoy shear zone.

8.2 Ground preparation

The foundation for the Santoy deposits was created when the Lizard Lake pluton and ore zone adjacent dykes were emplaced ca. 1877 Ma during the structural amalgamation of the Flin Flon-Glennie complex. Subsequent D_2 deformation, caused by the collision and underplating of the Flin Flon-Glennie complex with the Sask craton, was responsible for the creation of the dominant structural (S_2) fabrics of the region. In response to this phase of deformation, the dykes became highly strained internally with their margins paralleling

the S_2 foliation. The Packman Lake pluton was also emplaced during this deformation phase, albeit at a much later time, during peak metamorphism at ~1807 Ma.

The large amount of time between pluton emplacement and development of calc-silicate alteration and gold mineralization (potentially ~120 Ma) suggests that the relationship between the dykes and fault-fill vein ore zones is a structural one, whereby the foliation-parallel dykes and intrusions acted as a mechanical anisotropy and ultimately localized auriferous ore zones along these structures during D_3 (Figure 8.1).

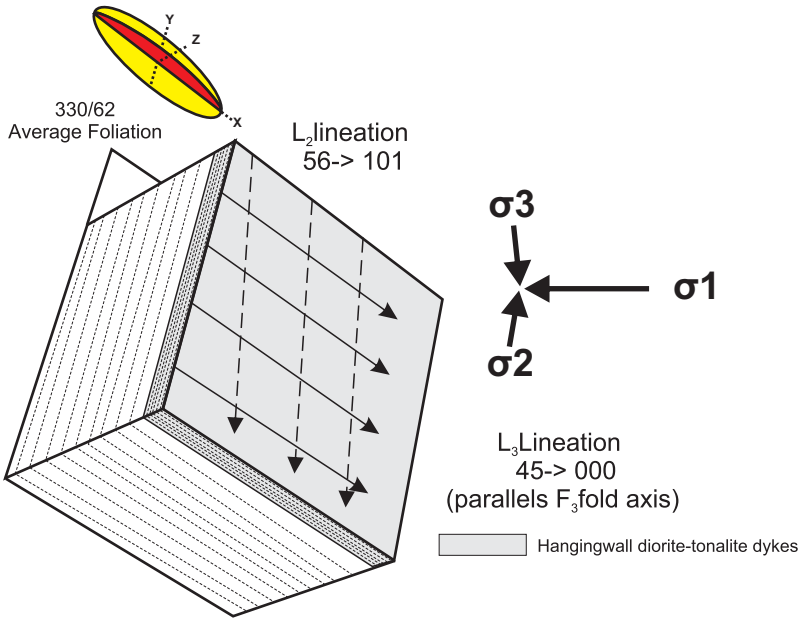

Figure 8.1: Foliation parallel dyke during pre-mineralization stage. (original in colour)

8.3 D_3 Folding and strain localization

Early deformation (D_3) in the near vertical, north-trending, Tabbernor fault zone was initiated by upper crustal level reactivation of an older Archean structure in the underlying Sask Craton (Ashton et al., 2005). This structure formed sheath-like F_3 folds

that parallel the fault with curvilinear, fold-axis parallel, stretching lineations (Ashton et al., 2005). Asymmetrical kinematic indicators and down-dip stretching lineations indicate that the youngest phase of ductile deformation within the Tabbernor fault zone was high-angle reverse (east side up) (Wilcox, 1990, 1991; Ashton and Balzer, 1995; Saskatchewan Geological Survey, 2003). As discussed in Chapter 3, D_3 shears (e.g., the Santoy shear zone) curve into parallelism with the Tabbernor fault zone. This relationship suggests that the Santoy shear zone may have developed as a splay off the main Tabbernor fault as folding progressed, localizing strain along the western limb of the Carruthers Lake synform and the ore zone parallel dykes contained therein. The strain gradient of the Santoy shear zone is expressed by openly folded quartz veins marginal to the main shear (zone 8 East), which reflects relatively low levels of shear strain, with strongly transposed isoclinally folded quartz veins within the main shear (Santoy 8A). A major curiosity regarding the tectonic/structural evolution of the Santoy shear zone is this relationship to strain localization as well as regional and local folding. The geometry of the folds is unusual in that they do not appear to represent shear folds and are controlled by the regional L_3 lineation. Stretching lineations that parallel fold axes can develop in a number of ways and this phenomenon is well documented in shear zones and gold deposits around the world (Robert et al., 2001). For example, as discussed by Robert et al. (1994) shear folds initially develop with their axis perpendicular to the stretching lineation and transport direction (Figure 8.2). Over time however, the fold axis may rotate into near parallelism with the transport direction and stretching lineation. This requires high shear strains and produces folds of isoclinal character. While isoclinal folds have been recognized, the similar attitudes

(plunge→trend) of the isoclinal folds in Santoy 8A and the open to close character of the folds at Santoy 8 East indicates that progressive fold rotation did not occur.

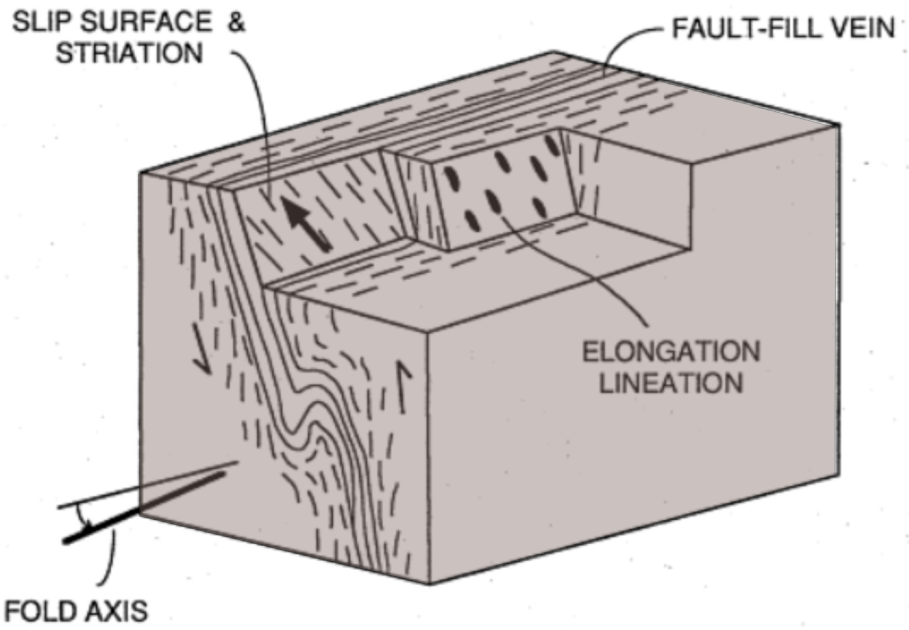

Figure 8.2: Fold axis and stretching lineation relationships in shear zones. (modified from Robert et al., 1994)

Another way to create parallel fold axis and mineral stretching lineations is shown in Figure 8.3 (below). In this manner the lineation is genetically related to folding, and will produce folds with the same character observed at Santoy. This mechanism is favoured because it accounts for the observed geometries of structures described above.

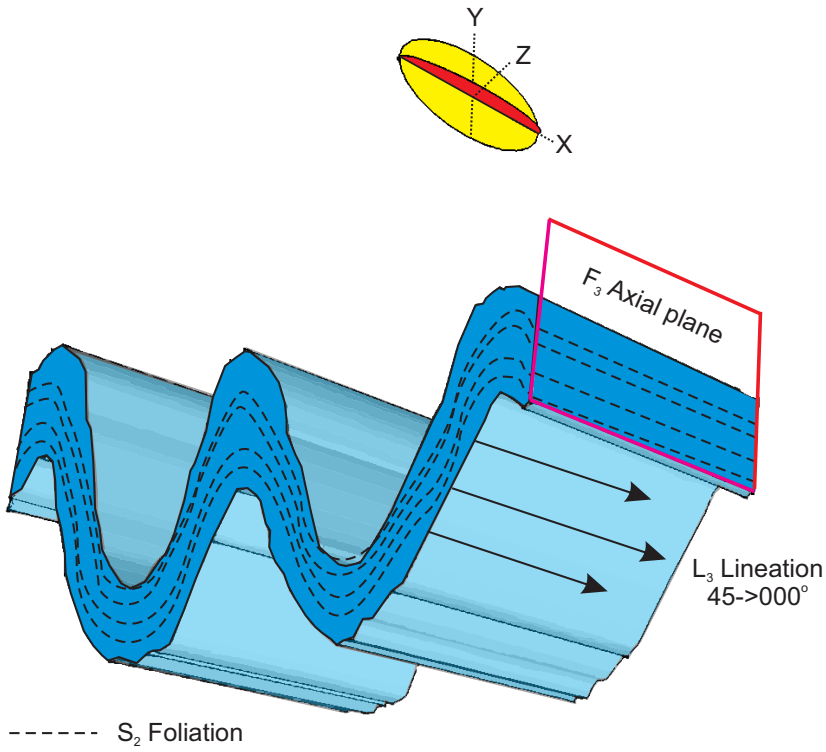

Figure 8.3: Fold axis and stretching lineation relationship in the Carruthers Lake synform. (original in colour)

8.4 Fault valve behaviour and foliation-parallel vein formation

The creation of faults and fractures (as well as veins) is dependent on the interplay between differential stress ($\sigma 1 - \sigma 3$), fluid pressure (P_{Fluid}), and fracture/fault orientation (2θ) (where θ is the angle between the fracture plane and $\sigma 3$ or the angle between $\sigma 1$ and the pole to the fracture plane) and can be represented graphically on the Mohr diagram (Ramsay & Hubert, 1983). Sibson et al. (1988) reasoned that because high-angle reverse faults are typically unfavourably oriented with respect to the compressional stress field (horizontal $\sigma 1$), fault formation, or reactivation can only occur when the fluid pressure

exceeds the lithostatic load; he incorporated these observations into the fault valve model, described below.

In order for faults and fractures to form, high fluid pressures act to counter the lithostatic confining pressure thereby shifting the Mohr circle to the left, and intersecting the Coulomb-Griffith failure envelope (Cox et al., 2001; Liu et al., 2011; Bons et al., 2012). In the Santoy region, foliation sub-parallel dykes and shear zones are pervasive mechanical anisotropies in this system and should also be accounted for. If these anisotropies are considered on a Mohr diagram, two Coulomb-Griffith failure envelopes can be derived, one for failure perpendicular (T ⊥) to the anisotropy and one for failure parallel to it (T ⊥) (Kerrich, 1989) (Figure 8.4).

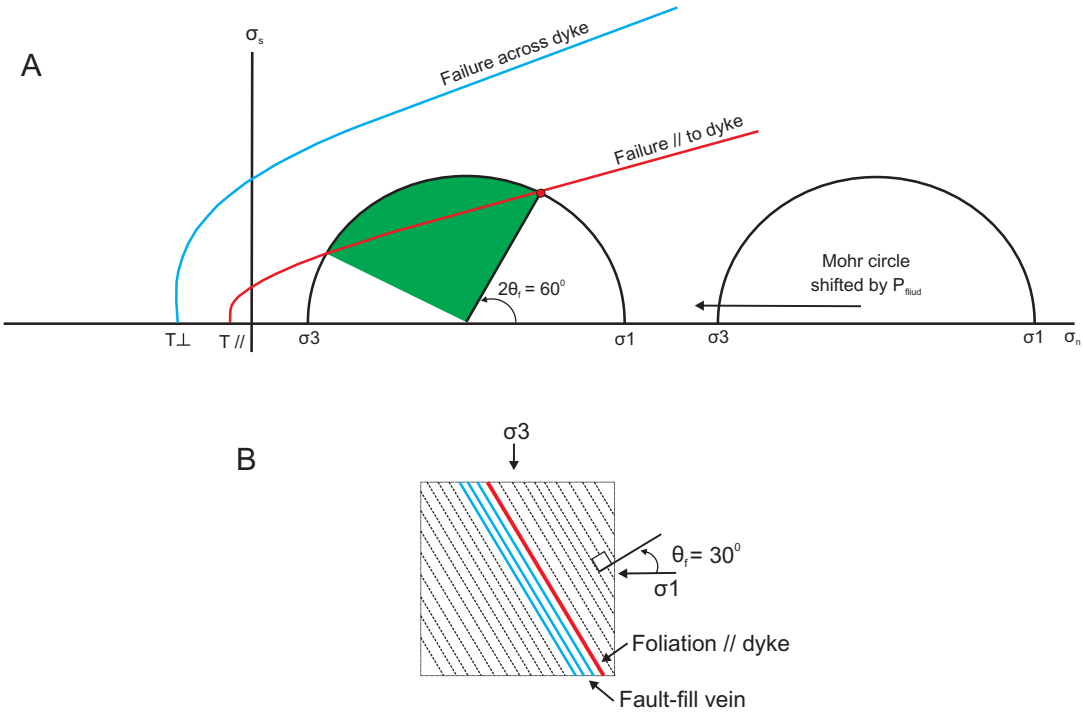

Figure 8.4: Mohr diagram stress-fluid pressure relationships during mineralization. A) Stress conditions for activation of a fault, which is unfavourably oriented to $\sigma 1$. Increasing fluid pressure builds and shifts the Mohr circle towards the left, and intersects the Coulomb-Griffith failure envelope. The failure envelope of the foliation-parallel dyke lies below the failure envelope of the isotropic rock and requires less differential stress to form a fault. B) This stress state will form a fault-fill vein along the foliation-parallel dyke dipping 60° ($\theta_f = 30^o$). A range of foliation-parallel dyke orientations could form fault-fill veins along their margins (shaded green area), with dips ranging from 60° to 13.5° (Cox et al., 2001; Fossen, 2010; Bons et al., 2012). (original in colour)

The resultant fault failure under supralithostatic fluid pressures results in the near total relief of shear stress and a large reduction in normal (differential) stress across the rupture zone, allowing fluids to drain along the fault. This abrupt drop in fluid pressure instigates the precipitation of hydrothermal auriferous veins (Figure 8.5). Subsequent "self-healing" of the rupture zone ultimately leads to a re-accumulation of fluid pressures and a repetition of the process. Once fault failure has started along the length of a finite structure such as an appropriately oriented dyke, it is unlikely to stop there and will

continue propagating along similarly oriented foliation planes. As a consequence of this, the absence of dykes within some portions of the ore zones should be expected.

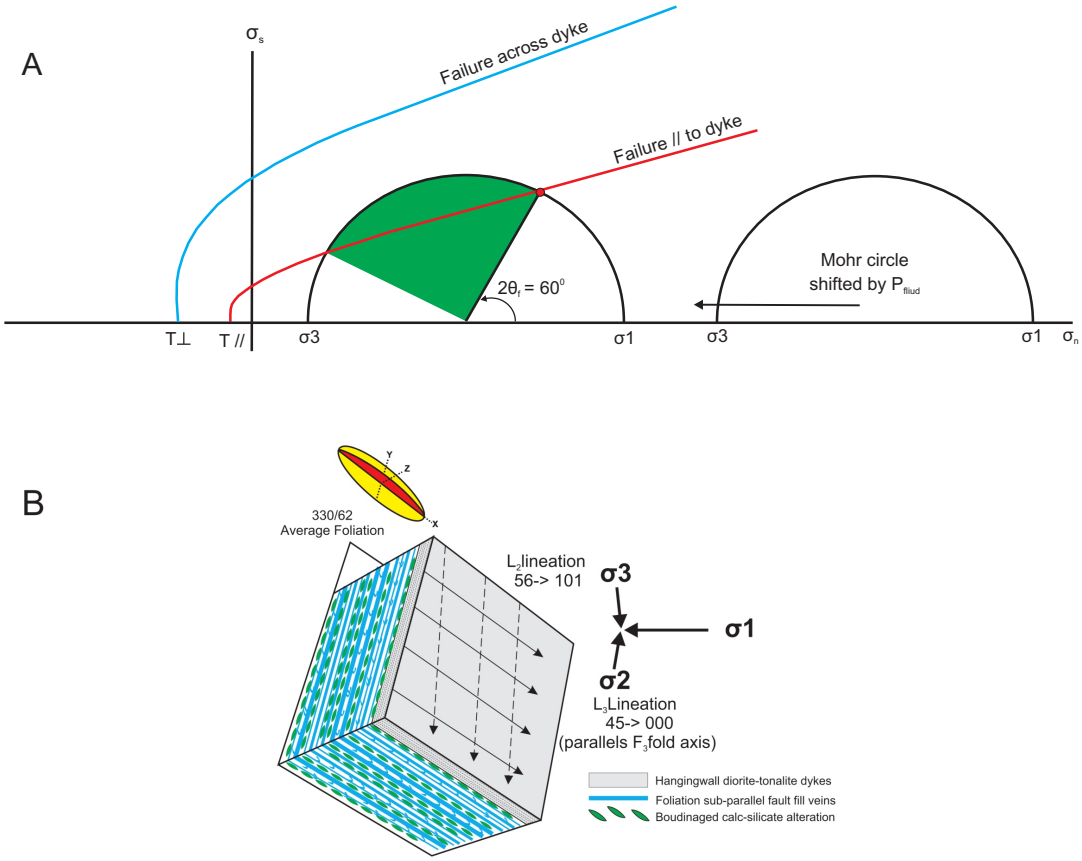

Figure 8.5: Vein formation parallel to foliated dykes. A) Mohr circle shifted left by increased fluid pressure (P_{fliud}). Failure along the dyke will occur and will result in foliation-parallel vein formation. B) As a result of these conditions, foliation-parallel veins and associated calc-silicate alteration developed adjacent to the dyke. (original in colour)

8.5 Post-mineralization ductile deformation

As discussed in Chapter 7, the syn-D_3 1736 ± 1.9 Ma beryliferous pegmatite that crosscuts the Santoy 8 deposit provides a minimum age of gold mineralization for the

Santoy system and records the final stages of D_3 deformation (ca. 1800 Ma - 1736 Ma) in the northern Glennie domain. Thus D_3 deformation appears to have continued after calc-silicate alteration and gold mineralization had ceased, overprinting, obscuring, and remobilizing the original deposit characteristics (Figure 8.6).

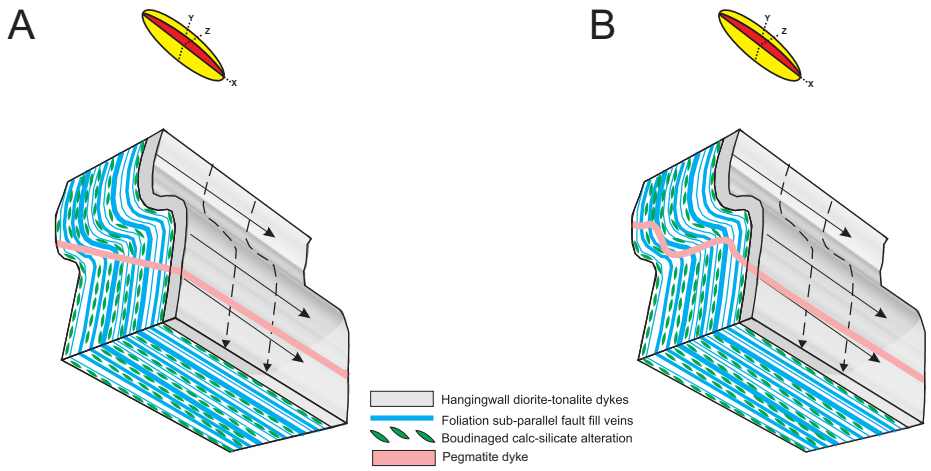

Figure 8.6: Post-mineralization ductile deformation and pegmatite emplacement. A) D_3 deformation post-1755 Ma continued folding the ore zones and pegmatite emplacement occurred at approximately 1736 Ma. B) D_3 deformation continued post-1736 Ma, further straining the deposits and folding the pegmatite dyke. (original in colour)

There is clearly a strong structural influence of regional F_3 folding on the Santoy deposits when the broad structural position of these deposits is accounted for. The deposits are located within the bounding Carruthers Lake synform. Santoy 7, 8 and Gap are situated along the strongly sheared western limb of this regional structure, whereas Santoy 8 East occurs near the hinge zone of the Carruthers Lake synform and the contact between the Lizard Lake pluton and mafic volcanic amphibolites of Assemblage A. Strain relationships discussed above suggest dominant flattening and extension parallel to

the stretching lineation. The changes in strike along the 8A orebody in a horizontal plane also reflect that it was moderately affected by F_3 folding, crenulating fabrics and warping the ore lens into an "S" shaped curve. The structural character and complexity of Santoy 8 East is largely caused by the reorientation of the system by 45→000º plunging S-folds marginal to the main shear along the western limb/hinge of the Carruthers Lake synform. The plunge of these folds controls the plunge of the deposit in this location. The structural position of the deposits within the Carruthers Lake synform may also explain the apparent discontinuity between Santoy 8 and Gap, which dips steeply towards the northeast, and Santoy 7 which is much flatter lying. F_3 folds in the vicinity of Santoy 7 are open and upright suggesting that F_3 strain is much lower in this location. This may be due to the strain shadow formed by the three F_3 regional folds (Ray Lake fold, Carruthers Lake antiform, Carruthers Lake synform) and the Packman Lake pluton (Figure 8.7). This pluton effectively buttressed the Carruthers Lake synform and auriferous deposits such that the attitude of structures close to its contact are relatively steep but become shallower and more flat lying (Santoy 7) to the north (Figure 8.8).

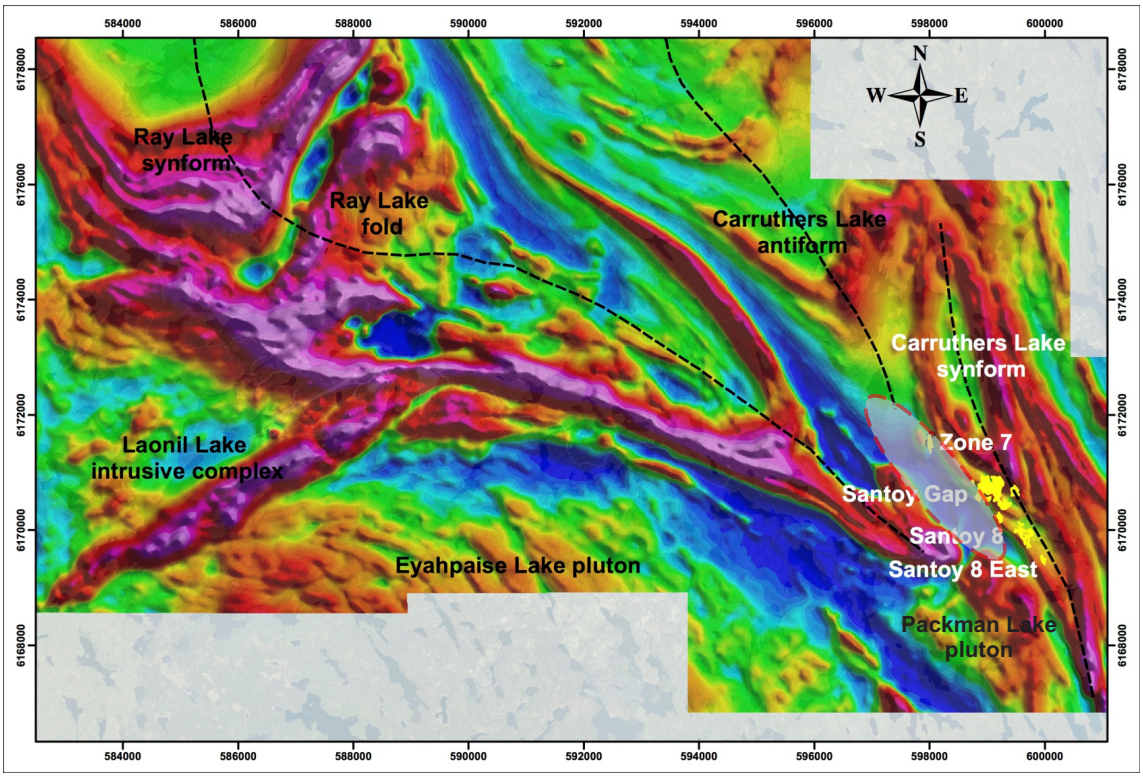

Figure 8.7: Santoy shear zone low-strain zone. The approximate location of lower strain area is highlighted in grey. (original in colour)

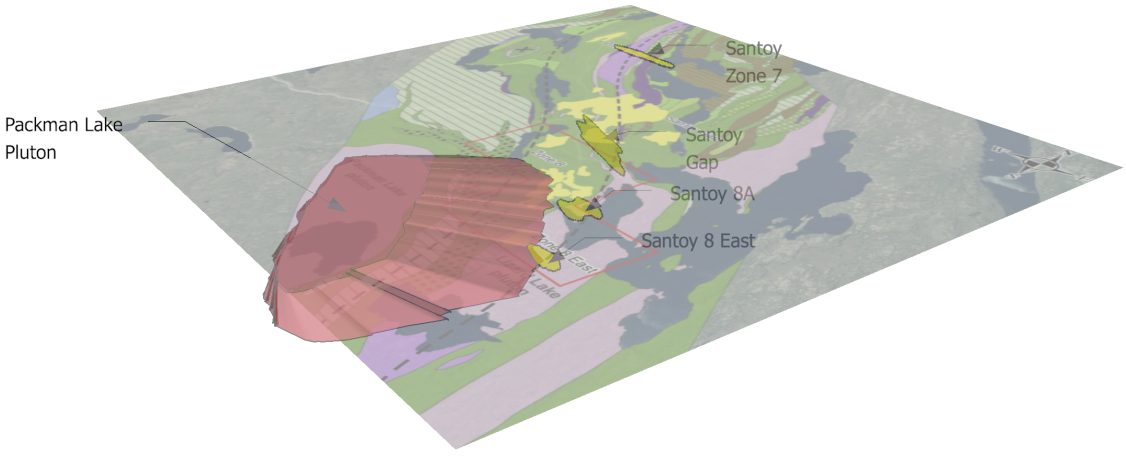

Figure 8.8: Buttressing effect of the Packman Lake pluton. This pluton buttresses the Carruthers Lake synform and auriferous deposits contained therein, while north of this pluton, the folds and Santoy zone 7 assume a shallower dip. (original in colour)

8.6 Brittle deformation

Brittle deformation, as expressed by three dominant sets of brittle faults, were measured and are described in detail below. The relative timing between these fault sets, however, remains relatively uncertain, as critical crosscutting relationships between them were not directly observed in the field.

Average fracture orientations obtained while mapping the surface exposure of Santoy 8A, described in Chapter 5, define a conjugate set oriented at approximately 106/84º and 227/73º. As shown in Figure 8.9, these fracture orientations can be used to determine the stress field at the time of fracture formation, and indicate that $\sigma 1$ was oriented at 22→074º, $\sigma 2$ 68→273º, and $\sigma 3$ 05→166º. The stress field is compatible with SW-NE directed shortening, and may be an expression of the latest stages of D_3 deformation.

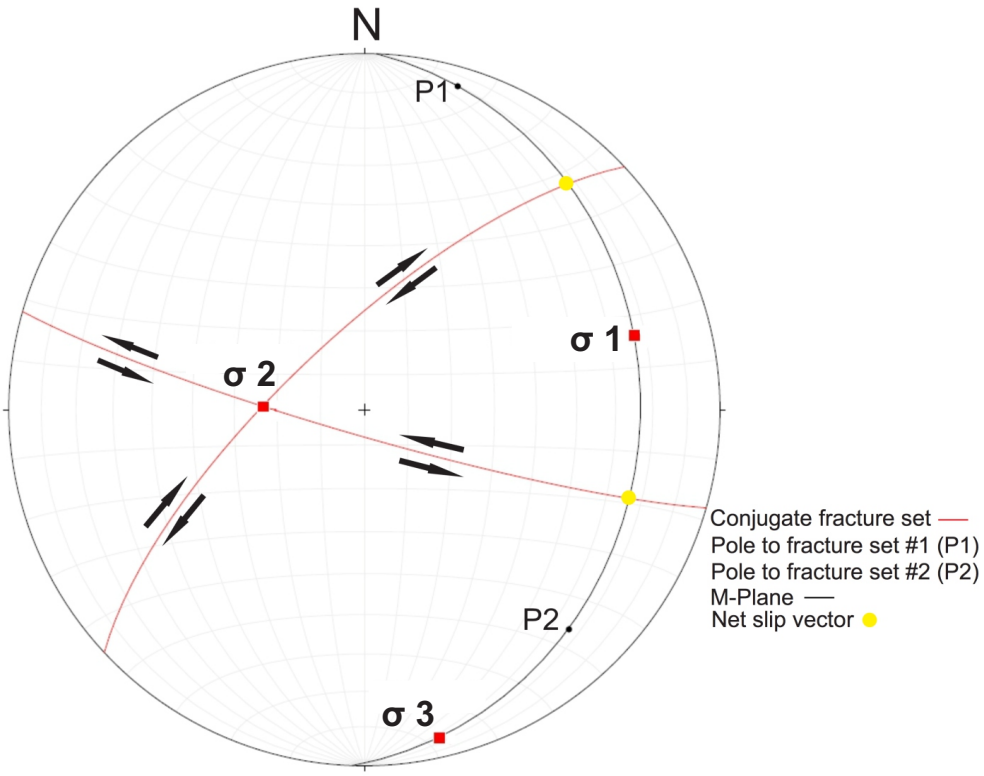

Figure 8.9: M-plane solution for late conjugate fractures interpreted to have formed during D_3 deformation. (original in colour)

These fractures also have the potential to offset the ore zones at depth. The intersection of the M-Plane with the fracture sets defines the net slip vector that is crucial for predicting possible ore zone displacements. The net slip vector on fractures oriented approximately 106/84º is predicted to be 22→108º and the net slip vector on fractures oriented approximately 227/73º is predicted to be 16→042º. This translates into sinistral-normal-strike-slip movement on fractures oriented 106/84º and dextral-normal-strike-slip movement on fractures oriented 227/73º (Figure 8.10).

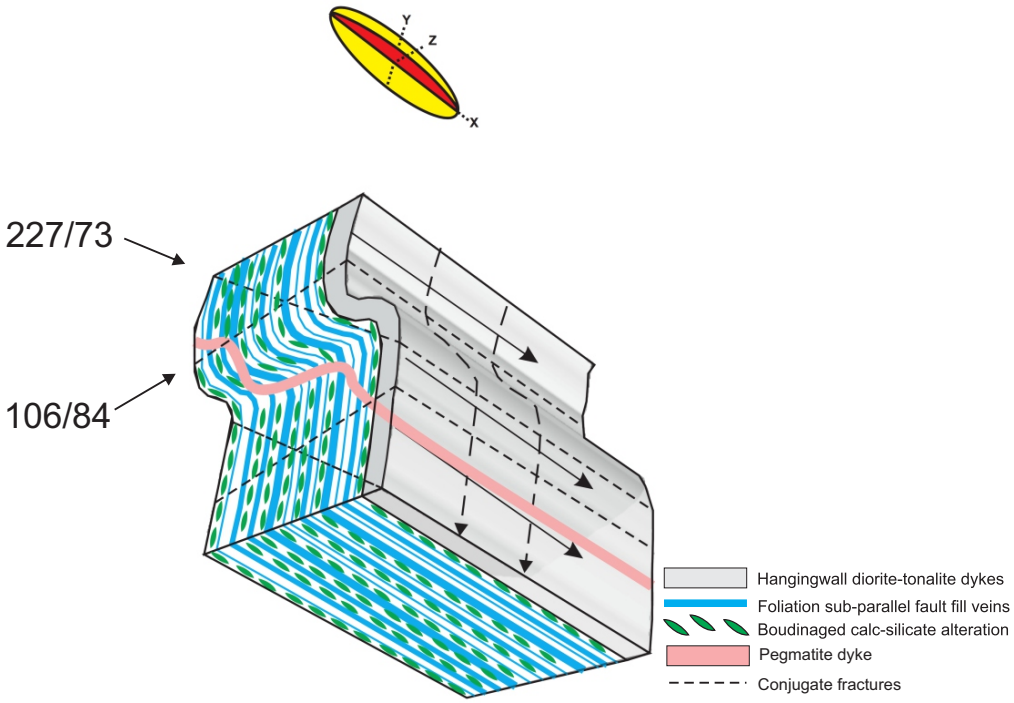

Figure 8.10: Conjugate fractures formed during the final stages of D_3 deformation. The area may have undergone compression in a strike-slip regime during the latter stages of D_3 deformation. (original in colour)

Late, NNW-striking, moderately to steeply east-dipping discrete brittle faults occur sub-parallel to the ore zones and foliation. Approximately 55 km to the SSE of the study area, Tran (1997) investigated sinistral shears and faults associated with the Tabbernor fault zone east of Grassy Narrows. The orientation of these faults discussed in Chapter 5 (Figure 5.14) are remarkably similar to those measured by Tran (1997) and links the development of these faults to the brittle reactivation of the Tabbernor fault zone during D_4 deformation (Figure 8.11 and Figure 8.12A).

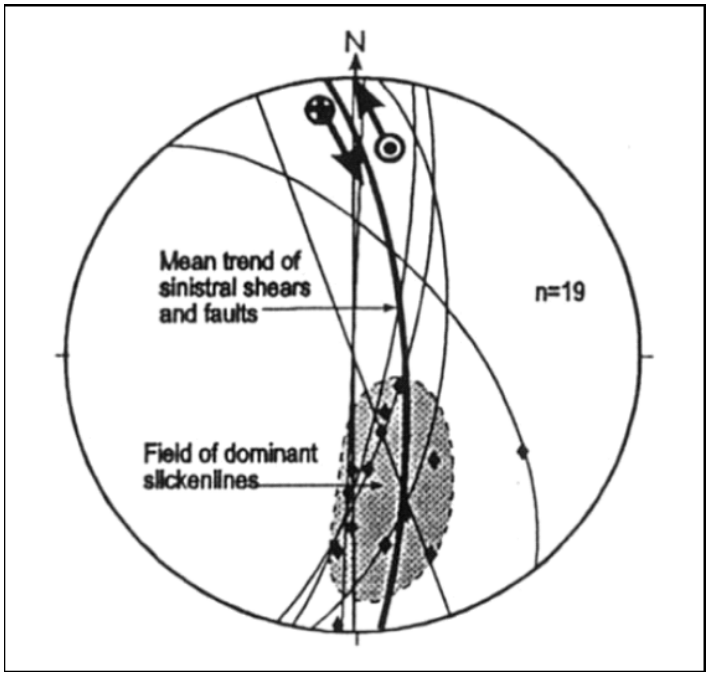

Figure 8.11: Lower hemisphere stereographic projection of sinistral faults and shear zones with slickenlines on faulted surfaces. Figure modified from Tran (1997).

The E-W set of moderately south-dipping brittle faults dissecting the Santoy 8A orebody post-dates the development of the crosscutting pegmatite dykes and were developed some time after 1736 ± 1.9 Ma. These faults may be associated with NW-SE directed shortening, and represent a brittle expression of D_4 deformation (Figure 8.12B).

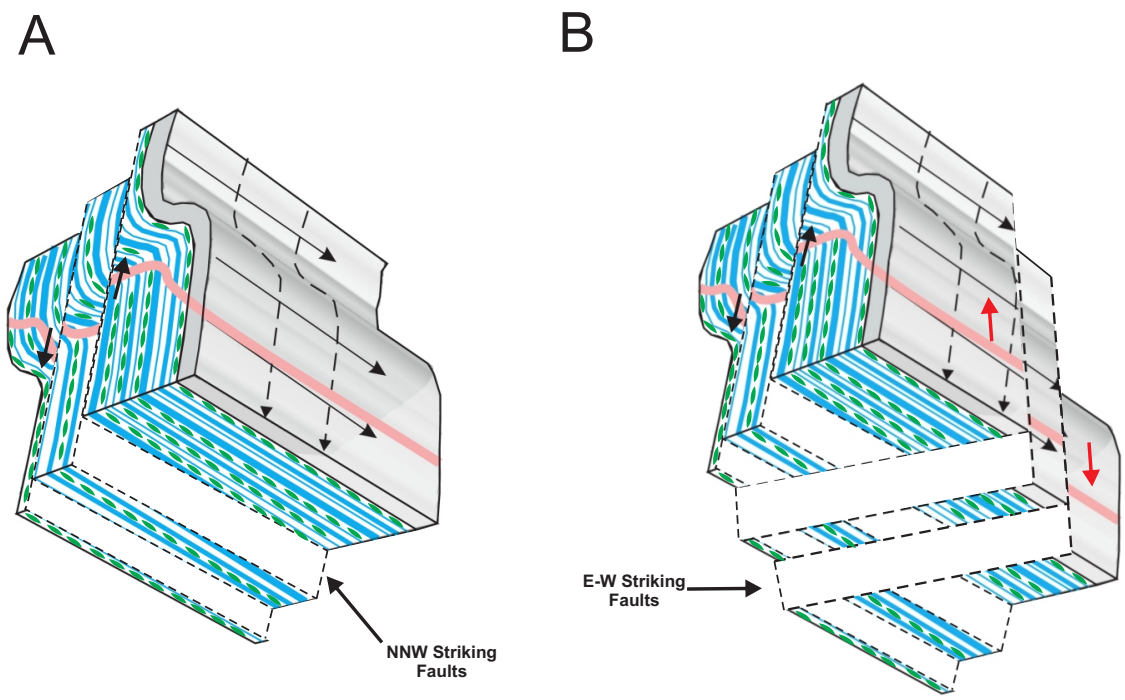

Figure 8.12: Development of NNW-striking and E-W striking brittle faults. A) NNW-striking sinistral ore zone parallel faults associated with the Tabbernor fault zone. B) E-W striking, post-pegmatite, reverse faults developed some time after 1736 ± 1.9 Ma. (original in colour)

8.7 The role of D_4 folding

As discussed in Chapter 3, the F_3 folds that dominate the map area are generally highly non-cylindrical with curvilinear axial planes and variable plunges. While interference between NE-trending F_4 folds and NW-trending F_3 folds is thought to have generated the regional dome-and-basin structure of the Glennie domain and greater Reindeer zone (Lewry et al., 1990), the influence of this structural superposition in the study area is debatable. Some of the irregularity of the F_3 folds may relate to interference between the earlier generation folds (F_2) and F_3 however most if it appears to be caused by naturally occurring non-cylindrical F_3 folding that has been influenced by interaction with the Eyahpaise and Packman Lake plutons.

8.8 Regional tectonic model

In order to aid with visualization, the structural relationships responsible for forming the deposits discussed in detail above are also discussed for the map region (below) beginning with the early stages of D_3 formation and folding.

Stage 1: Early D_3, ca. 1800-1780 Ma:

The major regional F_3 folds in the area began to develop and fold the S_2 parallel dykes and intrusions (e.g., the Lizard Lake pluton) (Figure 8.13).

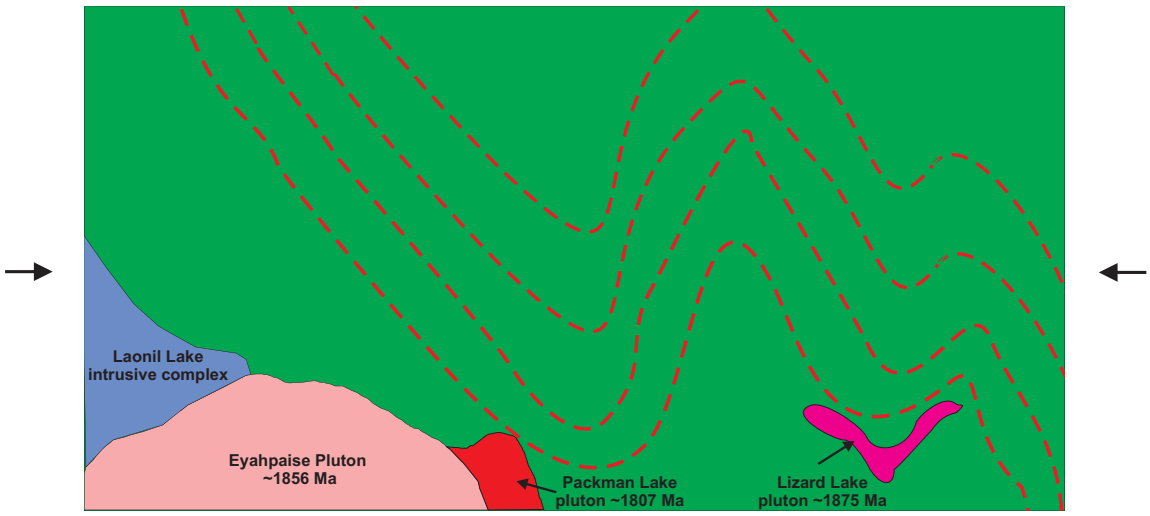

Figure 8.13: Stage 1, early-D_3 deformation circa 1800-1780 Ma. The Lizard Lake pluton, Packman Lake pluton, and regional foliation (S_2) during the early stages of F_3 folding. (original in colour)

Stage 2: Syn-to late-D_3, ca. 1780-1755 Ma:

During this time, the major F_3 folds in the area (Ray Lake fold, Carruthers Lake antiform, and Carruthers Lake synform) have formed and began warping around the Packman Lake/Eyahpaise plutons. The S_2-parallel Lizard Lake pluton and related intrusions were tightly folded and early ductile deformation in the near vertical, north-trending, Tabbernor fault zone (located approximately 8 km to the east of Santoy) was initiated. A

splay off of the main Tabbernor fault localized strain along the western limb of the Carruthers Lake synform (Figure 8.14).

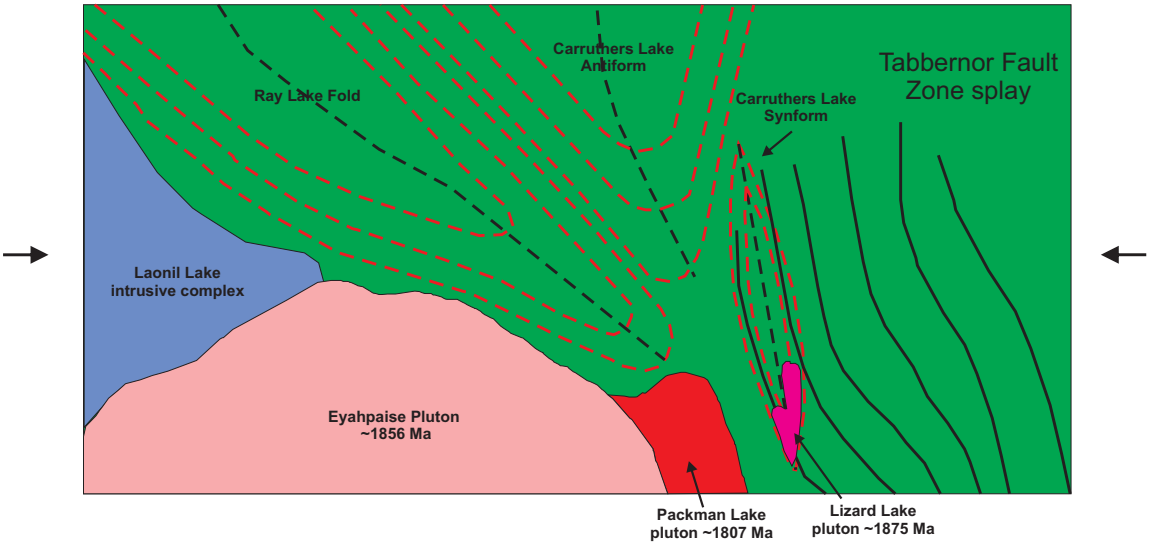

Figure 8.14: Stage 2, syn-to late-D_3 deformation circa 1780-1755 Ma. The major regional F_3 folds in the area have developed and a splay of the Tabbernor fault localized strain along the limb of the Carruthers Lake synform. (original in colour)

Stage 3: Late-D3, ca. 1755-1736 Ma:

The Santoy deposits developed under conditions of elevated fluid pressure. Santoy 8 East developed marginal to the main shear and is expressed by openly folded quartz veins, reflecting relatively low levels of shear strain. Santoy 8A developed within the main shear and displays strongly transposed isoclinally folded quartz veins. The compressional jog created as the Carruthers Lake synform warped around the Packman Lake pluton, may have further influenced fracture density and promoted fluid flow in this zone (Cox et al., 2001). D_3 deformation continued after the creation of the deposits and caused the folding and reorientation of some zones (Santoy zone 7, Santoy 8A and 8 East) discussed in section 8.5 (Figure 8.15).

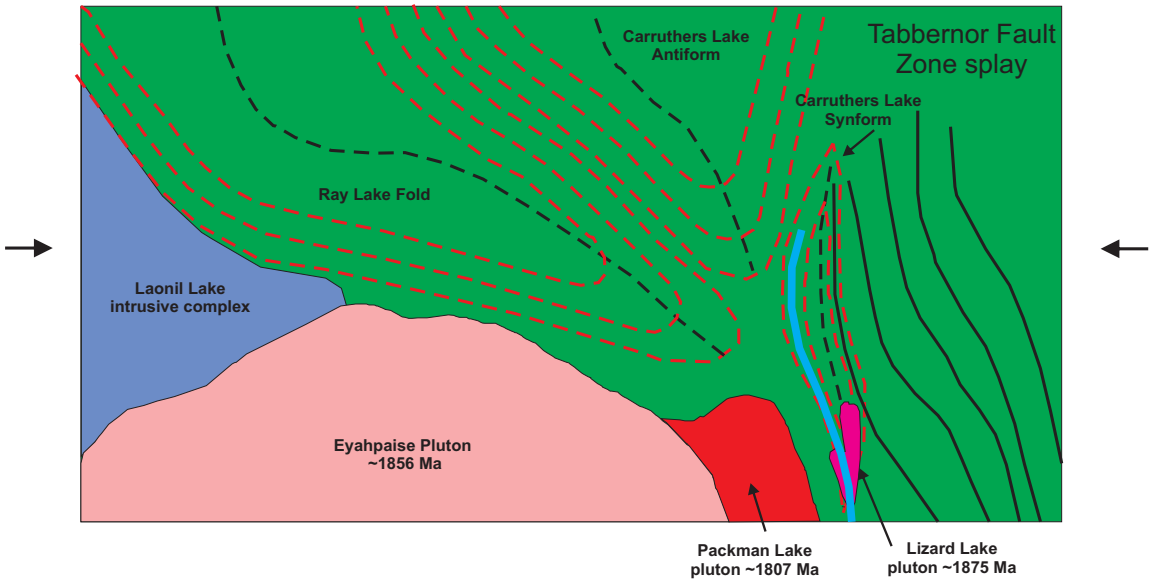

Figure 8.15: Stage 3, late-D_3 deformation circa 1755 Ma. Auriferous veins (blue) develop parallel to the foliation within the Santoy shear zone (western limb of the Carruthers Lake Synform) which, with continued shortening warps around the Packman Lake pluton (original in colour)

Stage 4: Continued late-D_3 shortening, ca. 1736 Ma:

F_3 folding continued from ~1755 Ma to at least ~1736 Ma when the beryliferous pegmatite crosscut the F_3 folds and auriferous ore zones at Santoy. The pegmatites were subsequently weakly folded during D_3 deformation, imparting an S_3 axial planar foliation within them (Figure 8.16).

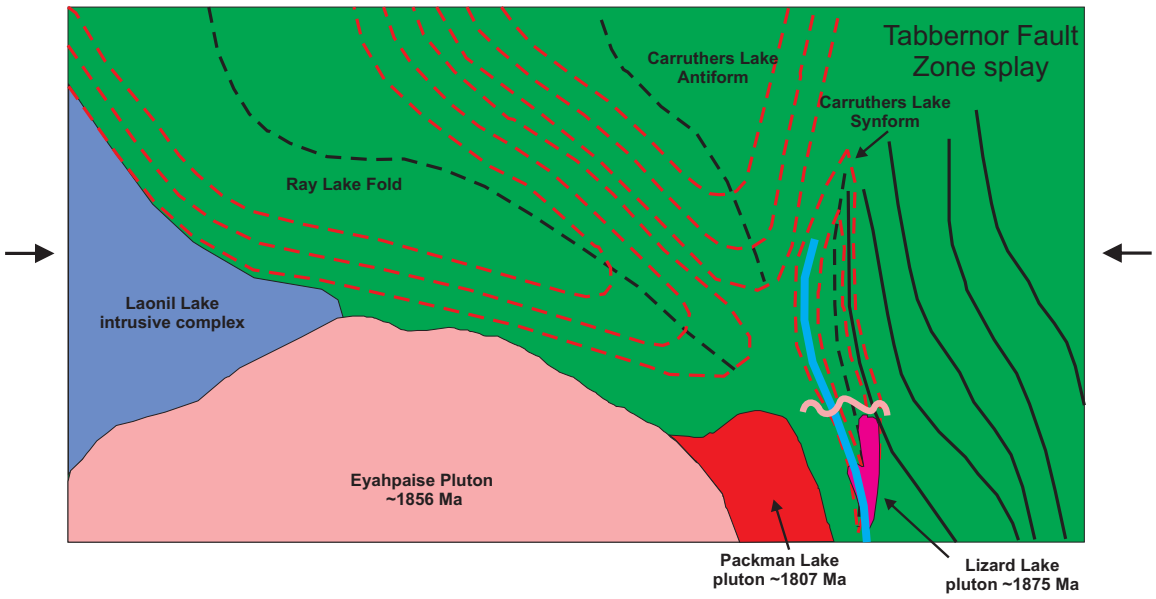

Figure 8.16: Stage 4, D_3 deformation circa 1736 Ma. Auriferous veins and F_3 folds are crosscut by the syn-D_3 beryliferous pegmatite dykes (Pink). The beryliferous pegmatite dykes were then weakly folded < 1736 Ma. (original in colour)

Stage 5: < 1736 Ma - D_4:

The final stages of D_3 shortening was expressed by the development of the conjugate fracture set compatible with NNE-WSW directed shortening described in section 8.6 (Figure 8.17 A). The Tabbernor fault zone was subsequently reactivated during D_4 and produced narrow brittle (sinistral strike-slip) faults parallel to the ore zones (Figure 8.17 B). The inferred NW-SE-directed shortening may also have been responsible for the creation of the E-W striking reverse brittle faults that crosscut the ore bodies (Figure 8.17 C).

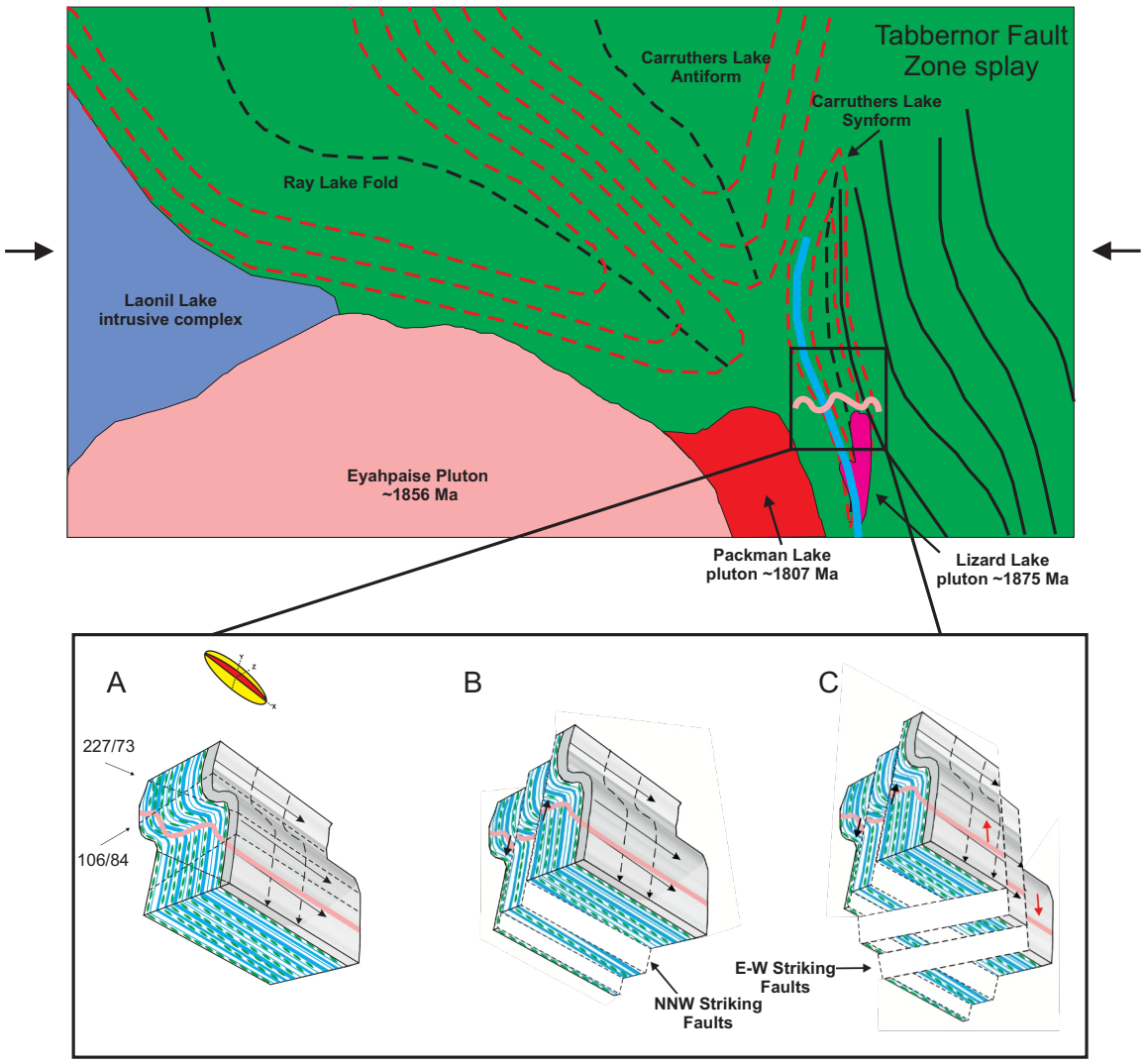

Figure 8.17: Stage 5, final stages of D_3 transitional to D_4 deformation. A) NNE-SSW directed shortening created the conjugate fractures during the final stages of D_3 shortening. B) Narrow ore zone sub-parallel brittle faults are associated with brittle reactivation of the Tabbernor fault zone during D_4. C) NW-SE directed shortening during D_4 may also be responsible for the creation of the E-W striking reverse brittle faults that crosscut the ore bodies. (original in colour)

8.9 Comparison with SRK model

The development of the model above was aided greatly by the geochronological component of the study that added a temporal constraint to the structural scenario at

Santoy. The preliminary structural model developed by SRK Consulting (Canada) Ltd. has many similarities with the updated model, however there are also several very significant differences that may have an impact on current exploration strategies.

1) Nature of alteration: As reported in Chapters 5, 6, and 7, it is clear from this study that the calc-silicate alteration occurs synchronously with ore related quartz veining and is a very important feature to this deposit system. The SRK model largely ignores the presence and importance of this assemblage as an alteration product of the quartz veining and associated mineralization.

2) Zone 8 East: The most obvious structural difference between the two models is the influence of strain localization along the limb of the Carruthers Lake synform, D_3 folding, and late-F_3 shortening. As reported in Chapter 1, the presence of folding of the fault-fill vein system of Santoy 8 East was recognised, however no explanation for this folding was offered. In the updated model and in the mapping of Delaney and Cutler (1992), F_3 folds that are related to the Carruthers Lake synform and strain localization within this structure, account for the dominant structural character of Santoy 8 East reported in Chapter 5.

3) Orebody orientation: In the previous model, the Santoy deposits were localized along the contractional jog (left-stepping) in a D_3 dextral-reverse shear zone. The plunges of the orebodies along this compressional jog were interpreted to vary with steeper ore plunges along the maximum strike curvature of the zone with Zone 7, forming a flatter lying orebody, and Santoy 8 and Gap forming steeper dipping orebodies. Fold and boudin axis subsequently rotated into parallelism with the L_3 stretching lineation in a

high strain environment. In this study, however, the orientation of the orebodies is interpreted to reflect both the conditions under which they were formed (i.e. shearing along appropriately oriented dykes under the influence of high fluid pressures) and the subsequent, late-D_3 deformation they underwent, responsible for highly straining and tilting the orebodies.

4) Foliation dip and ore zone localization: Due to the fact that the deposits are known to have undergone F_3 folding, observations of the foliation shallowing and steepening is not surprising. Due to this, it is very difficult to determine whether or not changes in the dip of the foliation alone controlled shear zone dilatency or not. In the model presented above, the role of increased fluid pressure as well as differential stresses and appropriately oriented foliation-parallel dykes are suggested to have played a role in shear zone dilation. In general, for ore bodies formed in dilational jogs (e.g., SRK model), the plunges of ore bodies are expected to be perpendicular to the shear zone movement direction (except under very high shear strain conditions), which in this case does not appear to accurately describe or predict the observed structural relationships at Santoy (Figure 8.18).

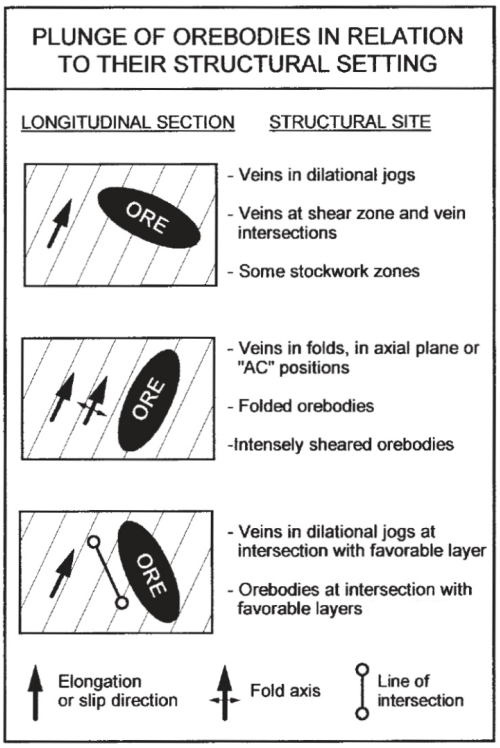

Figure 8.18: Plunge of orebodies in relation to their structural setting. Ore bodies formed in dilational jogs are expected to be perpendicular to the shear zone movement. In the case of Santoy the orebody plunges are parallel to fold axes and the elongation lineation of the shear zone and is more representative of a folded orebody (Robert and Poulsen, 2001).

5) Faulting: The presence of three sets of post-ore faults was confirmed, however they were not observed to have any major structural influence on the deposit itself (i.e. truncated or displaced ore zones). Possible displacements and expected net slip vectors are discussed above in section 8.6.

CHAPTER 9

SYNTHESIS & CONCLUSIONS

9.1 Introduction

The structural and geochronological analysis of the Santoy shear zone and Santoy 8 gold deposit was undertaken with five main questions in mind. The results of the study are summarized below. In addition to this, the exploration significance of this work will be discussed along with suggestions for further study in this area.

1: What are the kinematics, structures, and deformational events pertinent to the development and evolution of the Santoy shear zone?

The Santoy shear zone is a dextral-reverse oblique-slip structure comprising auriferous fault-fill veins and calc-silcate alteration emplaced along the margins of appropriately oriented dykes under high fluid pressure conditions. Strain localization began during D_3 as a splay off the Tabbernor fault developed along the western limb of the Carruthers Lake synform. Subsequent deformation was responsible for imparting a significant amount of post-vein strain that overprints and remobilizes the deposit system.

2: Ore zones occur within and along the contact of mafic volcanic amphibolites and the Lizard Lake pluton. Structural relationships also suggest that the Carruthers Lake synform has warped around the Packman Lake pluton during progressive D_3 deformation. What are the ages of these intrusions?

The Lizard Lake pluton age is ~1874.6 ± 1.9 Ma, emplaced during the amalgamation of the Flin Flon-Glennie Complex. The age of the tonalite pluton provides a maximum age constraint for mineralization in the Santoy shear zone. The 1807 ± 7 Ma

age for the Packman Lake pluton indicates that warping/flexuring of the Carruthers Lake synform occurred after ca. 1807 Ma and served as a competent buttress that helped localize strain along the Santoy shear zone during D_3. The compressional jog created may have further influenced fracture density and promoted fluid flow (Cox et al., 2001).

3: Ore zones within the Santoy system are closely spatially associated with tonalite, diorite, and quartz diorite dykes. Are these dykes and plutonic bodies discussed above related genetically and/or temporally? Additionally, are these magmatic events in some way related to the formation of the ore zones themselves?

The age of one of the ore zone adjacent dykes dated at Santoy is 1874.6 ± 2.9 Ma. This age is identical within error to the age for the Lizard Lake pluton discussed above, and strongly suggests that the dyke is a magmatically related offshoot. The large amount of time between pluton/dyke emplacement and alteration (potentially ~120 Ma) suggests that the relationship between the dykes and ore is a structural one; that is, they are not genetically related to one another. This dispels the notion that the gold has a syngenetic origin with the plutonic rocks in the area.

4: What is the age of the alteration package associated with gold mineralization?

Petrographic and macroscopic observations indicate that calc-silicate alteration is synchronous with quartz vein development and gold mineralization hosted therein. Independent U-Pb titanite and zircon ages (Z1 and Z6 Fraction) indicate that alteration and mineralization occurred at ~1755 ± 8 Ma.

5: What is the age of the beryliferous pegmatites that crosscut Santoy Zone 3 and Zone 8?

The syn D_3 beryliferous pegmatite age of 1736 ± 1.9 Ma provides a minimum age of gold mineralization for the Santoy deposits. This age is within error of and confirms a previous ~1727 ± 17 Ma age zircon from a pegmatite which crosscuts Santoy Zone 3. Structural relationships discussed in Chapter 5 suggest these pegmatites are recording the final stages of D_3 deformation (~1800-1736 Ma) in the northern Glennie domain that were previously thought to be around 1800-1770 Ma (Ashton et al., 2005). This extends known tectonic activity in the Flin Flon-Glennie complex by a large margin.

9.2 Exploration significance

1. The Santoy gold deposits and other showings in the area show spatial association with metavolcanic/amphibolitic rocks of Assemblage A where they are marginal to plutonic bodies and invaded by dykes. This may be a reflection of the orientation and competency of these dykes with respect to the host rocks. These dykes are not found in the younger package of rocks in the Pine Lake greenstone belt (Assemblage B). However, the age of mineralization (~1755 Ma) suggests that similar structural relationships between younger appropriately oriented intrusions and related dykes within Assemblage B may exist.

2. As suggested by (Tourigny et al., 2004), dyke density mapping may be beneficial for targeting mineralization; in addition to this, the mere presence of dykes may increase potential. The absence of dykes, however, does not preclude the formation of ore zones, as the faults are likely to extend further than the anisotropy itself, once it has nucleated.

3. The presence of the calc-silicate assemblage and or sporadic quartz veins down hole may indicate the proximal development of fault-fill veins. Barren segments along auriferous structures are to be expected and are a natural expression of fault-fill vein systems.

4. The potential for deposits north of zone 7 and south of Santoy 8 is high and will show a close relationship to D_3 structures as a result of deposit formation and deformation. Vein systems are largely foliation/dyke parallel due to emplacement conditions and ductile deformation in the Pine Lake greenstone belt.

5. The age of syn-D_3 mineralization and proximity to the Tabbernor fault to the east suggests this fault zone may have played a role in sourcing auriferous fluids and may be an attractive exploration target.

6. The 1807 Ma age for the buttressing quartz syenite pluton indicates that flexure around this pluton developed after 1807 Ma. Large flexures in the Ray Lake fold and other (D_3) fold limbs may also be prospective.

9.3 Future questions

There are obviously many questions for future study/research in this area, however, a few that stand out are as follows:

1. The timing of D_3 deformation in the Northern Glennie domain may be somewhat different than other parts of the Flin Flon-Glennie Complex. What are the age constraints of the other deformation events? If the D_3 minimum age is ~1736 Ma what is the role of D_4 deformation?

2. What are the geochemical-fluid conditions that produce the calc-silicate alteration?

3. It is unknown at this time how much gold is concentrated within the sulphide assemblages as “invisible gold” however laser ablation work on the sulphides would enhance our understanding of the distribution and textural setting of gold within the sulphide phases.

References

Allmendinger, R. W., Cardozo, N. C., and Fisher, D., 2013, Structural Geology Algorithms: Vectors & Tensors: Cambridge, England, Cambridge University Press, 289 pp.

Ansdell, K.M. (2005): Tectonic evolution of the Manitoba-Saskatchewan segment of the Paleoproterozoic Trans-Hudson Orogen, Canada: Canadian Journal of Earth Sciences, v. 42 p. 741-759

Ashton, K.E. (1999): A proposed lithotectonic domainal re-classification of the southeastern Reindeer Zone in Saskatchewan; in Summary of Investigations 1999, Volume 1, Saskatchewan Geological Survey, Sask. Energy Mines, Misc. Rep. 99-4.1, p92-100.

Ashton, K.E. and Balzer, S. (1995): Wildnest-Tabbernor transect: Pelican Lake–Tabbernor fault area (part of 63M-3); in Summary of Investigations 1995, Saskatchewan Geological Survey, Sask. Energy Mines, Misc. Rep. 95-4, p13-22.

Ashton, K.E., Lewry, J.F., Heaman, L.M., Hartlaub, R.P., Stauffer, M.R., and Tran, H.T. (2005): The Pelican Thrust Zone: basal detachment between the Archean Sask Craton and Paleoproterozoic Flin Flon–Glennie Complex, western Trans-Hudson Orogen; Can. J. Earth Sci., v42, no4, p685-706.

Bickford, M.E. and Hill, B.M. (2007): Does the arc accre- tion model adequately explain the Paleoproterozoic evolution of southern Laurentia?: An expanded interpretation. Geology, 35, p167–170.

Bickford, M.E., Collerson, K.D., Lewry, J.F. and Orrell, S.E. (1992): Pegmatites and leucogranites as probes of crust beneath allochthonous orogenic rocks in the Glennie and La Ronge domains; in Summary of Investigations 1992, Saskatchewan Geological Survey, Sask. Energy Mines, Misc. Rep. 92-4, p124-129.

Bickford, M.E., Van Schmus, W.R., Collerson, K.D. and Macdonald, R. (1987): U-Pb zircon geochronology project: new results and interpretations; in Summary of Investigations 1987, Saskatchewan Geological Survey, Sask. Energy Mines, Misc. Rep. 87-4, p76-79.

Bickford, M.E., Van Schmus, W.R., Macdonald, R., Lewry, J.F., and Pearson, J.G. (1986): U-Pb zircon geochronology project for the Trans-Hudson Orogen: current sampling and recent results; in Summary of Investigations 1986, Saskatchewan Geological Survey, Sask. Energy Mines, Misc. Rep. 86-4, p101-107.

Bons, P.D., Elburg, M.A., Gomez-Rivas E. (2012): A review of the formation of tectonic veins and their microstructures. Journal of Structural Geology, 43 (2012), pp. 33–62

Bucci, L.A., Hagemann, S.G., Groves, D.I. and Standing, J.G. (2002) The Archean Chalice gold deposit: a record of complex, multistage, high-temperature hydrothermal activity and gold mineralisation associated with granitic rocks in the Yilgarn Craton, Western Australia. Ore Geology Reviews, 19, 23-67.

Bucci, L.A., McNaughton, N.J., Fletcher, I.R., Groves, D.I., Kositcin, N., Stein, H.J., Hagemann, S.G. (2004): Timing and duration of high-temperature gold mineralization and spatially associated granitoid magmatism at Chalice, Yilgarn Craton, Western Australia. Economic Geology, 99, pp. 1123–1144

Budding, A.J. and Kirkland, S.J.T. (1956): The geology of the Reindeer River area; Sask. Dep. Miner. Resour., Rep.22, 42p.

Byers, A.R. (1962): Major faults in western part of Canadian Shield with special reference to Canada; in Stevenson, J.S. (eds.), The Tectonics of the Canadian Shield, Roy. Soc. Can., p40-59.

Cardozo, N., and Allmendinger, R. W., 2013, Spherical projections with OSXStereonet: Computers & Geosciences, v. 51, no. 0, p. 193 - 205

Chiarenzelli, J.R. (1989): The Nistowiak and Guncoat Gneisses: implications for the tectonics of the Glennie and La Ronge domains, northern Saskatchewan, Canada; unpub. Ph.D. thesis, Univ. Kansas, 229p.

Chiarenzelli, J.R., Aspler, L.B., Villeneuve, M., and Lewry, J. (1998): Early Proterozoic evolution of the Saskatchewan Craton and its allochthonous cover, Trans-Hudson Orogen; J. Geol., v106, p247-267.

Corrigan, D, Hajnal, Z., Németh, B. and Lucas, S.B. (2005): Tectonic framework of a Palaeoproterozoic arc-continent to continent-continent collisional zone, Trans-Hudson Orogen, from geological and seismic reflection studies. Canadian Journal of Earth Sciences, 42, p421–434.

Corrigan, D., Galley, A. G. and Pehrsson, S. (2007): Tectonic evolution and metallogeny of the southwestern Trans-Hudson Orogen. In: Goodfellow, W. D. (ed.) Mineral Deposits of Canada: A Synthesis of Major Deposit-types, District Metallogeny, the Evolution of Geological Provinces, and Exploration Methods. Geological Association of Canada, Mineral Deposits Division, Special Publication, 5, p881–902.

Corrigan, D., Pehrsson, S., Wodicka, N., and DeKemp, E. (2009): The Palaeoproterozoic Trans-Hudson Orogen; a prototype of modern accretionary processes. In Ancient orogens and modern analogues. Edited by J.B. Murphy, J.D. Keppie, and A. Hynes. Geological Society (of London), Special Publication 327. p457–479.

Cox, S.F., M.A. Knackstedt, M.A., and Brown J. (2001): Principles of structural control on permeability and fluid flow in hydrothermal systems; Chapter 1 in Richards, J.P. and Tosdal, R.M. (eds.), Structural Controls on Ore Genesis, Rev. Econ. Geol., v14, p1-24.

Delaney, G.D. (1986): Bedrock geological mapping, Laonil Lake area (part of NTS 63M-11 and -12); in Summary of Investigations 1986, Saskatchewan Geological Survey, Sask. Energy Mines, Misc. Rep. 86-4, p32-41.

Delaney, G.D. (1987): Bedrock geological mapping, Carruthers – Uskik Lakes area; in summary of investigations 1987, Saskatchewan Geological Survey. Sask. Energy Mines Misc. Rep. 87–94, 8–17.

Delaney, G.D. (1992): Gold in the Glennie Domain; Sask. Energy Mines, Misc. Rep 92-5, 71p.

Delaney, G.D. (1995): Gold in the Glennie Domain, Trans-Hudson Orogen; in Richardson, D.G. (ed.), Investigations Completed by the Saskatchewan Geological Survey and the Geological Survey of Canada Under the Geoscience Program of the Canada-Saskatchewan Partnership Agreement on Mineral Development (1990-1995), Geol. Surv. Can., Open File 3119 / Sask. Energy Mines, Open File Rep. 95-3, p53-58.

Delaney, G.D. (2016): Geology of the Pine Lake Greenstone Belt Laonil-Uskik Lakes Area (part of NTS 63M-11 and 12; Saskatchewan Geological Survey, Sask Ministry of the Economy, Geoscience Map 240

Delaney, G.D. and Cutler, S.A. (1992): Geological setting of the 'Santoy Lake' gold camp (part of NTS 63M-11 and -12); in Summary of Investigations 1992, Saskatchewan Geological Survey, Sask. Energy Mines, Misc. Rep. 92-4, p30-40.

Delaney, G.D., Carr, S.D. and Parrish, R.R. (1988): Two U-Pb zircon ages from eastern Glennie Lake Domain, Trans-Hudson Orogen, Saskatchewan; in Radiogenic Age and Isotopic Studies: Rep. 2, Geol. Surv. Can., Pap. 88-2, p51-58.

Dubé, B. and Gosselin, P. (2007): Greenstone-hosted quartz-carbonate veins; in Goodfellow, W.D. (ed.), Mineral Deposits of Canada: A Synthesis of Major Deposit-Types, District Metallogeny, the Evolution of Geological Provinces, and Exploration Methods, Geol. Assoc. Can., Miner. Dep. Div., Spec. Publ. No. 5, p49-73.

Durocher, K.E. (1997): A study of the P-T-t fluid evolution of the Glennie Domain, Trans-Hudson Orogen; unpubl. Ph.D. thesis, Univ. Saskatchewan, Saskatoon, 302p.

Durocher, K.E., Cutler, S.A., Delaney, G.D., and Kyser, T.K. (1992): Gold occurrences in the 'Santoy Lake' area, Glennie Domain, Trans-Hudson Orogen; in Summary of Investigations 1992, Saskatchewan Geological Survey, Sask. Energy Mines, Misc. Rep. 92-4, p41-50.

Durocher, K.E., Kyser, T.K. and Delaney, G.D. (1993): The pressure-temperature-time fluid history of the Santoy Lake area, Glennie Domain, Trans-Hudson Orogen: preliminary petrogenetic, geothermometric results and ^{207} Pb/^{206} Pb zircon ages; in Summary of Investigations 1993, Saskatchewan Geological Survey, Sask. Energy Mines, Misc. Rep. 93-4, p97-104.

Durocher, K.E., Kyser, T.K., and Delaney, G.D. (2001): Thermotectonic studies in the Paleoproterozoic Glennie Domain, Trans-Hudson orogen, Canada; Precamb. Resear., v109, p175-202.

Elliott, C.G. (1995): The Tabbernor fault and Proterozoic and Phanerozoic movements in Saskatchewan and Manitoba; in LITHOPROBE Trans-Hudson Orogen Transect, 5th Transect Meeting, LITHOPROBE Secret., Univ. Brit. Colum., Rep. 48, p148-155.

Fossen, H. (2010): Structural Geology. New York: Cambridge University Press.

Fumerton, S.L., Stauffer, M.R. and Lewry, J.F. (1984): The Wathaman Batholith: largest known Precambrian pluton; Can. J. Earth Sci., v21, p1082-1097.

Giroux, D.L. (1995): Location and Phanerozoic history of the Tabbernor fault; in Summary of Investigations 1995, Saskatchewan Geological Survey, Sask. Energy Mines, Misc. Rep. 95-4, p153-155.

Heaman, L.M., Kamo, S.L., Ashton, K.E., Reilly, B.A., Slimmon, W.L., and Thomas, D.J. (1992): U-Pb geochronological investigations in the Trans-Hudson Orogen, Saskatchewan; in Summary of Investigations 1992, Saskatchewan Geological Survey, Sask. Energy Mines, Misc. Rep. 92-4, p120-123.

Heaman, L.M., Kamo, S.L., Delaney, G.D., Harper, C.T., Reilly, B.A., Slimmon, W.L., and Thomas, D.J. (1991): U-Pb geochronological investigations in the Trans-Hudson Orogen, Saskatchewan: preliminary results by the ROM Laboratory in 1990-91; in Summary of Investigations 1991, Saskatchewan Geological Survey, Sask. Energy Mines, Misc. Rep. 91-4, p74-75.

Helmstaedt, H. (1986): Report on the geology and structure of the Seabee and Currie Rose properties, Laonil Lake, Saskatchewan; Placer Development Ltd., internal report, 14p.

Helmstaedt, H. (1987): Report on the geology and structure of the Seabee and Currie Rose properties, Laonil Lake, Saskatchewan; Placer Development Ltd., internal report, 14p.

Hoffman, P., (1988): United Plates Of America, The Birth Of A Craton: Early Proterozoic Assembly And Growth Of Laurentia: Annual Review of Earth and Planetary Sciences, v. 16, no. 1, p. 543-603

Jaffey, A.H., Flynn, K.F., Glendenin, L.E., Bentley, W.C. and Essling, A.M. (1971): Precision measurement of half-lives and specific activities of ^{235}U and ^{238}U. Physical Review 4: 1889-1906.

Johnston, W.G.Q (1968): The geology of the Kelly Lake area; Sask. Dep. Miner, resour., Rep. 106, 64p.

Kerrich, R (1989): Geodynamic setting and hydraulic regimes: Shear zone hosted mesothermal gold deposits. In: Mineralization and Shear Zones (ed. Bursnall JT), Geological Association of Canada, Short Course Notes, 6, 89–128.

Krogh, T.E. (1973): A low contamination method for hydrothermal decomposition of zircon and extraction of U and Pb for isotopic age determinations. Geochimica et Cosmochimica Acta 37: 485-494.

Kyser, T.K., Fayek, M. and Sibbald, T.I.I. (1992): Geochronologic studies in the La Ronge and Glen- nie domains; *in* Summary of Investigations 1992, Saskatchewan Geological Survey, Sask. Energy Mines, Misc. Rep. 92-4, p130-134.

Lewry, J., MacDonald, R., Livesey, C., Meyer, M., Van Schmus, R., and Bickford, M., (1987): U-Pb Geochronology of Accreted Terranes in the Trans-Hudson Orogen, Northern Saskatchewan, Canada: Geological Society, London, Special Publications, v. 33, no. 1, p. 147-166.

Lewry, J.F. (1977): The Geology of the Glennie Lake Area; Sask. Dep. Miner. Resour., Rep. 143, 59p.

Lewry, J.F. and Collerson, K.D. (1990): The Trans- Hudson Orogen: extent, subdivisions and problems. In: Lewry, J. F. and Stauffer, M. R. (eds) The Early Proterozoic Trans-Hudson Orogen of North America. Geological Association of Canada, Special Paper, 37, 1–14.

Lewry, J.F., and Macdonald, R. (1988): Observations on deformation in the Glennie Domain and Hanson Lake Block. In Summary of investigations 1988. Saskatchewan Geological Survey, Saskatchewan Energy and Mines, Miscellaneous Report, 88-4, p. 35–41.

Lewry, J.F., Hajnal, Z., Green, A., Lucas, S.B., White, D., Stauffer, M.R., Ashton, K.E., Weber, W., and Clowes, R. (1994): Structure of a Paleoproterozoic continent–continent collision zone: a LITHOPROBE seismic reflection profile across the Trans-Hudson Orogen, Canada. Tectonophysics, 232: 143–160.

Lewry, J.F., Thomas, D.J., Macdonald, R., and Chiarenzelli, J. (1990): Structural relations in accreted terranes of the Trans-Hudson Orogen, Saskatchewan: telescoping in a collisional regime?; in Lewry, J.F. and Stauffer, M.R. (eds.), The Early Proterozoic Trans-Hudson Orogen of North America, Geol. Assoc. Can., Spec. Pap. 37, p75- 94.

Liu, Y., Chi, G., Bethune, K. M., & Dube, B. (2011). Fluid dynamics and fluid-structural relationships in the Red Lake mine trend, Red Lake greenstone belt, Ontario, Canada. *Geofluids*, *11*(3), 260-279.

Lucas, S.B., Green, A., Hajnal, Z., White, D., Lewry, J., Ashton, K., Weber, W., and Clowes, R. (1993): Deep seismic profile across a Proterozoic collision zone: surprises at depth. Nature (London), 363: 339–342.

Lucas, S.B., Stern, R.A., Syme, E.C., Reilly, B.A., and Thomas, D.J. (1996): Intraoceanic tectonics and the development of continental crust: 1.92-1.84 Ga evolution of the Flin Flon Belt, Canada; Geol. Soc. Amer. Bull., v108, no5, p 602-629.

Ludwig, K.R. (2003): User's manual for Isoplot 3.00 a geochronological toolkit for Excel. Berkeley Geochronological Center Special Publication 4, 71 p.

Mattinson, J. (2005): Zircon U-Pb chemical abrasion (CA-TIMS) method: Combined annealing and multi-step partial dissolution analysis for improved precision and accuracy of zircon ages. Chemical Geology 220, 47-66.

Maxeiner, R. O., Harper, C., Corrigan, D. and Macdougall, D. G. (2004): La Ronge-Lynn Lake Bridge Project: geology of the Southern Reindeer Lake area. Saskatchewan Industry and Resources. Open File Report 2003-1, 2 CD-ROM set and 3 maps.

Maxeiner, R.O. and Normand, C. (2009): Bedrock geology of the Keg-Trade lakes area (Churchill River), central Glennie Domain (parts of NTS 63M/05and 73P/08); in Summary of Investigations 2009, Volume 2, Saskatchewan Geological Survey, Sask. Ministry of Energy and Resources, Misc. Rep. 2009-4.2, Paper A-8, 23p

McEwan, B. (2013): Summary of Geological Mapping of the Santoy Mine area during the summer of 2012 internal report, 27p.

McInnes, W. (1913): The basins of the Nelson and Churchill rivers; Geol. Surv. Can., Mem. 30, 146p.

McNicoll, V.J., Delaney, G.D., Parrish, R.R., and Heaman, L.M. (1992): U-Pb age determinations from the Glennie Lake Domain, Trans-Hudson Orogen, Saskatchewan; in Radiogenic Age and Isotopic Studies: Report 6, Geol. Surv. Can., Pap. 92-2, p57-72.

Meyer, M.T., Bickford, M.E. and Lewry, J.F. (1992): The Wathaman Batholith: an Early Proterozoic continental arc in the Trans-Hudson Orogen, Can- ada; Geol. Soc. Am. Bull., v104, p1073-1085.

Morrelli, R.M. And MacLachlan, K. (2012): Saskatchewan Gold: Mineralization Styles and Mining History; Sask. Ministry of Energy and Resources, Rep 262, 171p

Padgham, W.A. (1966): The geology of the Wapawekka Narrows area (north half), Saskatchewan (73I-16-N); Sask. Dep. Miner. Resour., Rep.87, 113p.

Ramsay, J.G. (1967): Folding and Fracturing of Rocks; McGraw-Hill Book Co., New York, 565p.

Ramsay, J. G., Huber, M.I. (1983): The techniques of modern structural geology. In: Strain Analysis, vol. 1. London, Academic Press, London

Ramsay, J.G., Huber, M.I. (1987): The techniques of modern structural geology. In: Folds and Fractures, vol. 2. Academic Press, London.

Robert, F. and Poulsen, K.H. (2001): Vein formation and deformation in greenstone gold deposits; Chapter 5 in Richards, J.P. and Tosdal, R.M. (eds.), Structural Controls on Ore Genesis, Rev. Econ. Geol., v14, p111-155.

Robert, F., Poulsen, K.H., and Dubé, B. (1994): Structural analysis of lode gold deposits in deformed terranes; Geol. Surv. Can., Open File 2850, 140p.

Saskatchewan Geological Survey (2003): Geology, and mineral and petroleum resources of Saskatchewan; Sask. Industry and Resources, Misc. Rep. 2003-7, 173p.

Satterly, J. (1932): Pelican Narrows area, Saskatchewan; Geol. Surv. Can., Summ. Rep., pt C, p26-36.

Schneider, D.A., Heizler, M.T., Bickford, M.E., Wortman, G.L., Condie, K.C., and Perilli, S. (2007): Timing constraints of orogeny to cratonization: thermochronology of the Paleoproterozoic Trans-Hudson orogen, Manitoba and Saskatchewan, Canada; Precamb. Resear., v153, p65-95.

Schultz, D.J. (1996): The fluid history of the Seabee mesothermal gold deposit, northern Saskatchewan; unpubl. M.Sc. thesis, Univ. Saskatchewan, Saskatoon, 122p.

Sibson, R.H., Robert, F., and Poulsen, K.H. (1988): High-angle reverse faults, fluid-pressure cycling, and mesothermal gold-quartz deposits; Geol., v16, p551-555.

Sims, P.K., and Peterman, Z.E. (1986): Early Proterozoic Central Plains Orogen: a major buried structure in the north-central United States. Geology, 14: 488–491.

Stauffer, M.R. (1984): Manikewan: an early Proterozoic ocean in central Canada, its igneous history and orogenic closure; Precamb. Resear., v25, p257-281.

Stauffer, M.R. (1990): The Missi Formation: an Aphebian molasse deposit in the Reindeer Lake Zone of the Trans-Hudson Orogen, Canada; in Lewry, J.F. and Stauffer, M.R., (eds.), The Early Proterozoic Trans-Hudson Orogen of North America, Geol. Assoc. Can., Spec. Pap. 37, p75-94.

Streckeisen, A. L. (1976): To each plutonic rock its proper name. Earth Science Reviews, 12(1), 1-33.

Sun, M., Kyser, K., Stauffer, M., Kerrich, R., and Lewry, J. (1996): Constraints on the timing of crustal imbrication in the central Trans-Hudson Orogen from single zircon $^{207}Pb/^{206}Pb$ ages of granitoid rocks from the Pelican thrust zone, Saskatchewan. Canadian Journal of Earth Sciences, 33: 1638–1647.

Syme, E.C. and Bailes, A.H. (1993): Stratigraphic and tectonic setting of volcanogenic massive sulphide deposits, Flin Flon, Manitoba. Economic Geology, 88, 566–589.

Syme, E.C., Lucas, S.B., Zwanzig, H.V., Bailes, A.H., Ashton, K.E. and Haidl, F.M. (1998): Geology, NATMAP Shield Margin Project area of Flin Flon Belt, Manitoba/Saskatchewan; notes accompanying Geol. Surv. Can. Map 1968A, Man. Energy Mines Map A-98-2, Sask. Energy Mines Map 258A.

Tourigny, G. (2003a). Preliminary structural study of the gold-bearing shear zone system at the Seabee mine, northern Saskatchewan; in Summary of Investigations 2003, Volume 2, Saskatchewan Geological Survey, Sask. Industry and Resources, Misc. Rep. 2003-4.2, CD-ROM, Paper B-1, 11p.

Tourigny, G. (2003b): Structural geology of the Seabee shear zone system, Seabee gold mine (part of NTS 63M/12); 1:2000-scale preliminary geological map with Summary of Investigations 2003, Volume 2, Saskatchewan Geological Survey, Sask. Industry and Resources, Misc. Rep. 2003-4.2.

Tourigny, G., Chi, G., Yuhasz, C., Olson, R., Berger, J., and Soloman, J. (2004): Structural controls and temperature-pressure conditions of gold-bearing quartz vein systems at the Seabee mine, northern Saskatchewan; in Summary of Investigations 2004, Volume 2, Saskatchewan Geological Survey, Sask. Industry and Resources, Misc. Rep. 2004-4.2, CD-ROM, Paper A-2, 18p.

Tran, H.T. (1997): Structural relations and Thermotectonic History of the Medicine Rapids-Grassy Narrows Area, northern Saskatchewan, Canada; unpub. Msc. thesis, Univ. Regina, 197p.

Tran, H.T. (2001): Tectonic evolution of the Paleoproterozoic Wollaston Group in the Cree Lake Zone, northern Saskatchewan, Canada; unpub. Ph.D. thesis, Univ. Regina, 458p.

Van Schmus, W.R., Bickford, M.E., Lewry, J.F., and Macdonald, R. (1987): U-Pb zircon geochronology in the Trans-Hudson Orogen, northern Saskatchewan, Canada; Can. J. Earth Sci., v24, p407-424.

White, D. J., Thomas, M. D., Jones, A. G., Hope, J., Németh, B. and Hajnal, Z. (2005): Geophysical transect across a Palaeoproterozoic continent-continent collision zone: the Trans-Hudson Orogen. Canadian Journal of Earth Sciences, 42, 385–402.

Wilcox, K.H. (1991): Geological relationships in the Wood Lake area, Tabbernor fault Zone, Saskatchewan; in Summary of Investigations 1991, Saskatchewan Geological Survey, Sask. Energy Mines, Misc. Rep. 91-4, p135-143.

Wilcox, K.H. (1990): Bedrock geology and gold metallogenesis, Nielson Lake area, Tabbernor fault Zone; in Summary of Investigations 1990, Saskatchewan Geological Survey, Sask. Energy Mines, Misc. Rep. 90-4, p74-83.

Williams, D., Delaney, G.D., and Cutler, S.A. (1992): Beryl pegmatites in the 'Santoy Lake Area', Glennie Domain; in Summary of investigations 1992, Saskatchewan Geological survey, Sask. Energy Mines, Misc. Rep. 9

Appendix A

Descriptions of representative thin sections

Thin section # 4

Field context: This is an oriented thin section made perpendicular to an F_3 fold axis to display S_2-S_3 fabric relationships.

Description: The main S_2 foliation is defined by hornblende. The S_3 foliation overprints S_2, is axial planar, and defined by biotite. Plagioclase is commonly altered to sericite and quartz and K-feldspar occur intergrown to form myrmekite. K- feldspar has deformation lamellae and quartz displays subgrain formation with undulatory extinction and deformation bands. Average grain size ~ 0.1 mm with curved – irregular grain boundaries.

Mineralogy:
Hornblende: 20 %
K-feldspar (microcline): 48%
Quartz: 10 %
Plagioclase: 10 %
Biotite: 10 %
Apatite: 1 %
Zircon: 1%

Rock Name: Quartz Syenite

Photo:

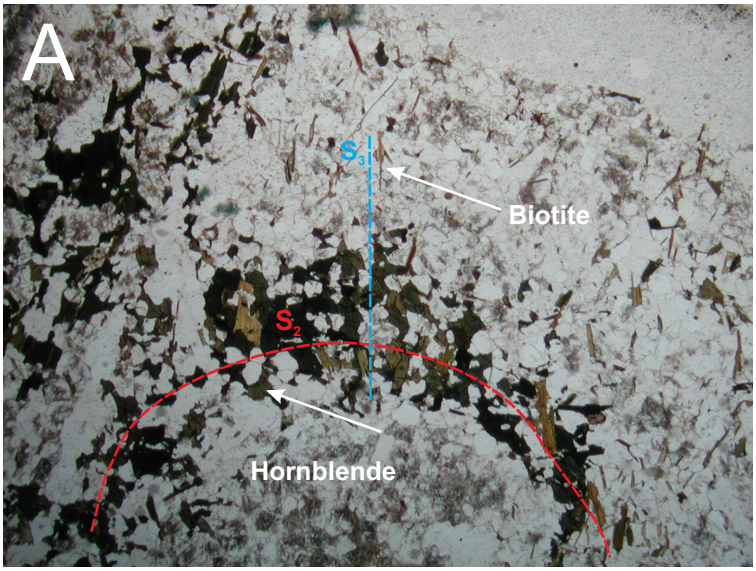

A: The S_3 foliation overprints S_2, is axial planar, and defined by biotite. The S_2 foliation is defined by hornblende.

Thin section # 5

Field context: This is thin section was taken within the Lizard Lake pluton. Sample contains F_3 folded calc-silicate alteration with highly strained fold limbs.

Description: Calc-silicate folded with S_2 foliation defined by hornblende. Mineralogy of the calc-silicate assemblage similar to thin section description 2A/2B. Lizard Lake pluton must predate calc-silicate assemblage associated with gold mineralization.

Mineralogy:

Quartz: 20 %
Plagioclase: 65 %
Hornblende: 10 %
Biotite: 5 %

Rock Name: Tonalite

SAN C12 012

Description: The sample is very well foliated with the foliation defined by biotite and chlorite as well as trace muscovite. Aveage grain size is ~ 0.25 mm with seriate to interlobate texture. Plagioclase has been altered to sericite. Calcite occurs dominantly as late fracture filling phase.

Mineralogy:
Plagioclase: 55 %
Quartz: 40 %
Chlorite/ Biotite: ~ 3 %
Muscovite: < 1 %
Sulphide minerals: < 1%
Calcite: < 1 %

Rock Name: Tonalite

SAN C12 GC 3: Thin section # 16

Field context: This thin section was collected from an ore zone adjacent dyke within 16L 463 ADR. This dyke is located several meters adjacent to the ore lens and was less altered and more suitable for geochronological analysis.

Description: This sample is well foliated with the foliation defined by lath shaped biotite which is variably altered to chlorite. Quartz veinlets are aligned parallel to the main foliation and display undulatory extinction and subgrain formation. Average grain size ranges from ~ 0.2 mm – 0.1 mm and display granoblastic textures. Plagioclase is altered around crystal margins to sericite.

Plagioclase: 70 %
Quartz: 20 %
Biotite: 5 %
Chlorite: 3%
Muscovite: 1 %
Sulphide minerals: (chalcopyrite, pyrite, pyrrhotite) < 1%
Accessory zircon, apatite, muscovite: < 1%

Rock Name: Tonalite

SAN C12 GC 3B: Thin section # 17

Field context: This thin section was collected from an ore zone adjacent dyke within 16L 463 ADR. This dyke is highly altered and was deemed unsuitable for geochronological analysis.

Description: This sample is weakly foliated with the foliation defined by chlorite. Grain sizes range from ~ 0.04 mm – 0.4 mm though average grain size is ~ 0.2 mm and display seriate to interlobate textures. Plagioclase is heavily altered to sericite, with alteration focussed along fracture surfaces. In this sample, there is also muscovite present.

Mineralogy:

Plagioclase: 60 %
Quartz: 35 %
Chlorite/ Biotite: ~ 3 %
Muscovite: 1 %
Sulphide minerals: < 1%

Rock Name: Tonalite

SAN C12 GC 4

Field context: This thin section was cut from the bulk sample sent for geochronological analysis of the Packman lake pluton.

Description: This sample is well foliated with the main foliation (S_2) defined by hornblende and S_3 foliation defined by biotite as in thin section #4 (see above). Opaque metallic mineral with triangular shaped exsolution patterns (Magnetite/illmenite?) is present as an accessory mineral. Biotite is lath shaped and largely euhedral while quartz grain boundaries are curved and migrating into K-feldspar crystals. Subgrains and deformation bands within the quartz and deformation twins within K-feldspar is also common

Microcline: 45 %
Hornblende: 25 %
Quartz: 15 %
Plagioclase: 6 %
Biotite: 5 %
Apatite: 1 %
Zircon: 1 %
Magnetite: 1 %

Rock Name: Syenogranite

Thin section # 38

Field context: This sample was collected for petrographic analysis of an ore zone adjacent dyke in 16L 490 ADR

Description: This sample is well foliated with the foliation defined by biotite and chlorite as well as minor muscovite. Plagioclase is altered to sericite. Calcite fills late fractures and partially replaces plagioclase in some instances. The average grain size is ~0.4 mm ranging from ~0.4 mm – 0.8 mm with inequigranular to polygonal textures.

Mineralogy:

Plagioclase: 83 %
Quartz: 10 %
Biotite/Chlorite: 5%
Muscovite: 1 %
Calcite: < 1 %
Titanite: < 1 %

Rock Name: Quartz Diorite

Thin section # 39

Field context: This sample was collected for petrographic analysis of an ore zone adjacent dyke in 16L 490 ADR

Description: This sample is well foliated with the foliation defined by hornblende and biotite. The hornblende is very irregular to anhedral while biotite forms euhedral-subhedral laths. Plagioclase is lightly altered to sericite. Rare biotite forms crosscutting main foliation. The average grain size is ~0.6 mm with inequigranular to interlobate textures.

Mineralogy:

Plagioclase: 85 %
Hornblende: 10 %
Biotite: ~ 5 %
Titanite: < 1 %

Rock Name: Diorite

Thin section # 46

Field context: This is a representative oriented thin section made from a heavily altered dyke within ore zone 16L 490 ADR.

Description: This sample has polygonal-equigranular texture and is very well foliated and is mainly defined by chlorite that has altered from biotite as well as hornblende. Plagioclase is extremely altered to sericite giving the hand sample a pinkish appearance. Highly irregular titanite is present however it has opaque inclusions (titanium oxides?). Grain size ranges from 0.1 - 0.4 mm with an average of approximately 0.3 mm.

Mineralogy:

Biotite/ Chlorite: 15 %
Plagioclase: 63 %
Hornblende: 20 %
Titanite: < 1 %
Epidote: < 1 %

Rock Name: Diorite

SAN C12 GC1: Thin section #15

Field context: This is a representative thin section made from the bulk sample of calc-silicate alteration sent for geochronological analysis of Titanite and Zircon.

Description: Diopside inclusions occur within the quartz veins, and quartz inclusions within the diopside, suggesting contemporaneous formation. Diopside crystals display evidence of deformation including undulatory extinction and subgrain formation. There is a small amount of biotite in this section parallel to the S_2 main foliation defined by hornblende. Plagioclase is commonly altered to sericite and crystals typically have polygonal grain boundaries though some are curved. Grain boundaries of quartz are highly irregular with the formation of subgrains evident. Gold was observed from the heavy mineral fraction collected from the Wilfley table however it was unfortunately not observed in thin section. Titanite within the sample is subhedral with associated apatite inclusions and occur within diopside phenocrysts.

Photos:

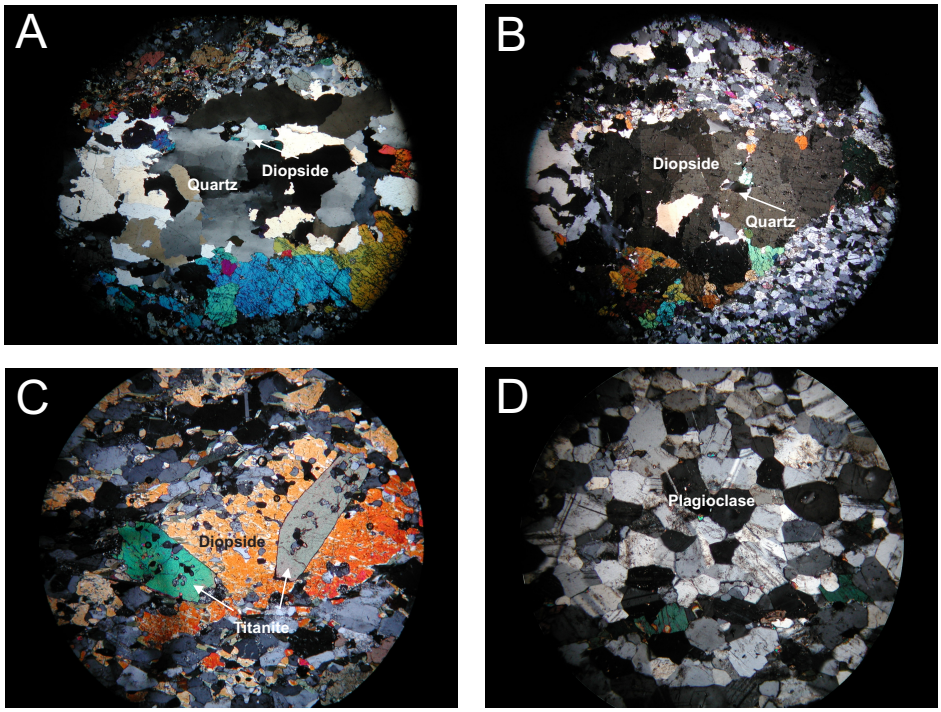

A: 1x MAG XPL FOV ~16mm. Diopside crystals within quartz vein. Quartz displays very irregular grain boundaries and subgrains. B: 1x MAG XPL FOV ~ 16mm. Quartz within diopside crystal. Diopside displays undulatory extinction and subgrain formation. C: 5x MAG XPL FOV ~3.5mm. Large subhedral titanite with apatite inclusions inside diopside crystal. D: 5x MAG XPL FOV ~3.5mm. Plagioclase crystals with polygonal-curved grain boundaries.

Appendix B

Relevant geochronologic ages in the Glennie domain

SAMPLE #	AGE	ERROR +	ERROR -	SYSTEM	INTERPRETED AGE	GEOCHRONOMETER	TECHNIQUE	EASTING	NORTHING	NAME	REFERENCE
HUD83-7	1881	6	6	U/Pb	Igneous Crystallization	Zircon	TIMS	588778	6099581	Palf Lake rhyolite	(Schmus et al., 1987)
HUD83-6	1893	35	35	U/Pb	Igneous Crystallization	Zircon	TIMS	566164	6108532	Carroll Lake gneiss	(Schmus et al., 1987)
HUD83-16	1852	12	12	U/Pb	Igneous Crystallization	Zircon	TIMS	566332	6171555	?Eyahpaise pluton (cut by, or gradational into)	(Schmus et al., 1987)
HUD83-14	1836	7	7	U/Pb	Igneous Crystallization	Zircon	TIMS	590908	6164351	unnamed, intrudes Eyahpaise pluton	(Schmus et al., 1987)
HUD83-13	1859	5	5	U/Pb	Igneous Crystallization	Zircon	TIMS	587969	6160430	Eyahpaise pluton	(Schmus et al., 1987)
HUD83-12	1850	9	9	U/Pb	Igneous Crystallization	Zircon	TIMS	592080	6158041	Wykes Lake pluton	(Schmus et al., 1987)
HUD83-11	1850	4	4	U/Pb	Igneous Crystallization	Zircon	TIMS	587308	6080843	unknown	(Schmus et al., 1987)
J87-1042	1773	4	4	U/Pb	Cooling	Titanite	TIMS	534401	6128302	Thomas Lake gneiss, Cartier Sheet	(Chiarenzelli et al., 1998)
J86-97	1774	12	12	U/Pb	Cooling	Titanite	TIMS	536760	6141552	Drope Lake gneiss, Cartier Sheet	(Chiarenzelli et al., 1998)
HUD84-31	1780	10	10	U/Pb	Cooling	Titanite	TIMS	548758	6140834	Drinking Lake gneiss, Cartier Sheet	(Chiarenzelli et al., 1998)
HUD84-22	1783	8	8	U/Pb	Cooling	Titanite	TIMS	529160	6149811	Mountain Lake granodiorite gneiss	(Chiarenzelli et al., 1998)
HUD84-22	1790	12	12	U/Pb	Cooling	Titanite	TIMS	529160	6149811	Mountain Lake granodiorite gneiss	(Chiarenzelli et al., 1998)
J87-1174	2410	1	1	U/Pb	Detrital	Zircon	TIMS	534825	6118783	Mylonitic biotite paragneiss, Hunter Bay Window	(Chiarenzelli et al., 1998)
J87-1174	2419	1	1	U/Pb	Detrital	Zircon	TIMS	534825	6118783	Mylonitic biotite paragneiss, Hunter Bay Window	(Chiarenzelli et al., 1998)
J87-1174	2530	1	1	U/Pb	Detrital	Zircon	TIMS	534825	6118783	Mylonitic biotite paragneiss, Hunter Bay Window	(Chiarenzelli et al., 1998)
J87-1174	2546	1	1	U/Pb	Detrital	Zircon	TIMS	534825	6118783	Mylonitic biotite paragneiss, Hunter Bay Window	(Chiarenzelli et al., 1998)
J87-1174	2627	2	2	U/Pb	Detrital	Zircon	TIMS	534825	6118783	Mylonitic biotite paragneiss, Hunter Bay Window	(Chiarenzelli et al., 1998)
J87-965	1770	2	2	U/Pb	Igneous Crystallization	Monazite	TIMS	543062	6133478	Iskwatikan Lake pegmatite	(Chiarenzelli et al., 1998)
J87-931	2454	289	102	U/Pb	Igneous Crystallization	Monazite	TIMS	536540	6135986	Iskwatikan Lake granitic gneiss	(Chiarenzelli et al., 1998)
J87-931	2466	32	25	U/Pb	Igneous Crystallization	Zircon	TIMS	536540	6135986	Iskwatikan Lake granitic gneiss	(Chiarenzelli et al., 1998)
J87-696	1774	24	24	U/Pb	Igneous Crystallization	Zircon	TIMS	548829	6140711	Drinking Lake pegmatite	(Chiarenzelli et al., 1998)
J87-17	1768	2	2	U/Pb	Igneous Crystallization	Monazite	TIMS	546958	6141587	Nistowiak Lake granite	(Chiarenzelli et al., 1998)
J87-1234	1837	7	6	U/Pb	Igneous Crystallization	Zircon	TIMS	545813	6145162	Nistowiak Lake window	(Chiarenzelli et al., 1998)
J87-1185	1765	1	1	U/Pb	Igneous Crystallization	Monazite	TIMS	526445	6116625	Hunter Bay Pegmatite	(Chiarenzelli et al., 1998)
J87-1161	2482	13	12	U/Pb	Igneous Crystallization	Zircon	TIMS	534186	6121592	Lac La Ronge granodioritic gneiss, Hunter Bay window	(Chiarenzelli et al., 1998)
J87-1042	1851	2	2	U/Pb	Igneous Crystallization	Zircon	TIMS	534401	6128302	Thomas Lake gneiss, Cartier Sheet	(Chiarenzelli et al., 1998)
J86-ILP	2492	19	17	U/Pb	Igneous Crystallization	Zircon	TIMS	539002	6136471	Iskwatikan Lake granodioritic gneiss	(Chiarenzelli et al., 1998)
J86-97	1852	18	10	U/Pb	Igneous Crystallization	Zircon	TIMS	536760	6141552	Drope Lake gneiss, Cartier Sheet	(Chiarenzelli et al., 1998)
J86-318	2942	5	5	U/Pb	Igneous Crystallization	Zircon	TIMS	541333	6141282	Mylonitic pegmatite, Nistowiak Thrust	(Chiarenzelli et al., 1998)
J86-318	2942	5	5	U/Pb	Igneous Crystallization	Zircon	TIMS	541333	6141282	Mylonitic pegmatite, Nistowiak Thrust	(Chiarenzelli et al., 1998)
HUD86-30	1889	9	8	U/Pb	Igneous Crystallization	Zircon	TIMS	587060	6172161	Laonil Lake intrusion, Wapassini Sheet	(Chiarenzelli et al., 1998)
HUD84-31	1847	6	5	U/Pb	Igneous Crystallization	Zircon	TIMS	548758	6140834	Drinking Lake gneiss, Cartier Sheet	(Chiarenzelli et al., 1998)
HUD84-22	1859	10	9	U/Pb	Igneous Crystallization	Zircon	TIMS	529160	6149811	Mountain Lake granodiorite gneiss	(Chiarenzelli et al., 1998)
DF	1770	15	15	U/Pb	Igneous Crystallization	Allanite	TIMS	545703	6140523	Nistowiak Lake Pegmatite	(Chiarenzelli et al., 1998)
J87-931	1774	280	411	U/Pb	Metamorphic	Monazite	TIMS	536540	6135986	Iskwatikan Lake granitic gneiss	(Chiarenzelli et al., 1998)

* Ages reported from the Saskatchewan Ministry of the Economy, Geological Atlas of Saskatchewan. (http://www.infomaps.gov.sk.ca/website/sir_geological_atlas/viewer.htm)

SAMPLE #	AGE	ERROR +	ERROR -	SYSTEM	INTERPRETED AGE	GEOCHRONOMETER	TECHNIQUE	EASTING	NORTHING	NAME	REFERENCE
J87-696	1762	1	1	U/Pb	Metamorphic	Monazite	TIMS	548829	6140711	Drinking Lake pegmatite	(Chiarenzelli et al., 1998)
J86-318	2302	35	35	U/Pb	Metamorphic	Zircon	TIMS	541333	6141282	Mylonitic pegmatite, Nistowiak Thrust	(Chiarenzelli et al., 1998)
J86-318	2302	35	35	U/Pb	Metamorphic	Zircon	TIMS	541333	6141282	Mylonitic pegmatite, Nistowiak Thrust	(Chiarenzelli et al., 1998)
J86-164	1806	10	10	U/Pb	Metamorphic	Zircon	TIMS	542029	6141970	Nistowiak Lake ferrodioritic gneiss	(Chiarenzelli et al., 1998)
J86-164	1806	10	10	U/Pb	Metamorphic	Zircon	TIMS	542029	6141970	Nistowiak Lake ferrodioritic gneiss	(Chiarenzelli et al., 1998)
J86-164	1837	20	20	U/Pb	Metamorphic	Titanite	TIMS	542029	6141970	Nistowiak Lake ferrodioritic gneiss	(Chiarenzelli et al., 1998)
J86-164	1837	20	20	U/Pb	Metamorphic	Titanite	TIMS	542029	6141970	Nistowiak Lake ferrodioritic gneiss	(Chiarenzelli et al., 1998)
J86-142	1840	15	15	U/Pb	Metamorphic	Zircon	TIMS	540215	6142385	Mylonitic gneiss, Nistowiak Lake	(Chiarenzelli et al., 1998)
J86-142	1840	15	15	U/Pb	Metamorphic	Zircon	TIMS	540215	6142385	Mylonitic gneiss, Nistowiak Lake	(Chiarenzelli et al., 1998)
HUD87-1	1785	1	1	U/Pb	Metamorphic	Monazite	TIMS	530350	6153189	Guncoat Thrust	(Chiarenzelli et al., 1998)
J86-ILP	1227	73	73	U/Pb	Pb Loss	Zircon	TIMS	539002	6136471	Iskwatikan Lake granodioritic gneiss	(Chiarenzelli et al., 1998)
J87-1232	2443	21	11	U/Pb	Protolith age	Zircon	TIMS	525290	6123945	, Sask Craton Garnetiferous tonalite gneiss	(Chiarenzelli et al., 1998)
J86-164	2428	13	12	U/Pb	Protolith age	Zircon	TIMS	542029	6141970	Nistowiak Lake ferrodioritic gneiss	(Chiarenzelli et al., 1998)
J86-164	2428	13	12	U/Pb	Protolith age	Zircon	TIMS	542029	6141970	Nistowiak Lake ferrodioritic gneiss	(Chiarenzelli et al., 1998)
J86-142	2804	14	12	U/Pb	Protolith age	Zircon	TIMS	540215	6142385	Mylonitic gneiss, Nistowiak Lake	(Chiarenzelli et al., 1998)
J86-142	2804	14	12	U/Pb	Protolith age	Zircon	TIMS	540215	6142385	Mylonitic gneiss, Nistowiak Lake	(Chiarenzelli et al., 1998)
J87-696	1840	28	28	U/Pb	Xenocryst	Zircon	TIMS	548829	6140711	Drinking Lake pegmatite	(Chiarenzelli et al., 1998)
J87-696	2441	11	11	U/Pb	Xenocryst	Zircon	TIMS	548829	6140711	Drinking Lake pegmatite	(Chiarenzelli et al., 1998)
Pelican Lake dyke	1737	2	2	U/Pb	Igneous Crystallization	Monazite	TIMS	621350	6106400	Flin Flon Domain Tabbernor Fault Dyke	(Elliott, 1995)
NLSZ tonalite	1833	2	2	U/Pb	Igneous Crystallization	Zircon	TIMS	619392	6105243	Flin Flon Domain Nielson Lake strain zone	(Elliott, 1995)
Nielson Lake pluton	1848	6	5	U/Pb	Igneous Crystallization	Zircon	TIMS	618034	6105272	Nielson Lake Pluton	(Elliott, 1995)
PCA-8822-378	1825	5	5	U/Pb	Cooling	Titanite	TIMS	570349	6095943	Maynard Creek granodiorite	(McNicoll et al., 1992)
PCA-8822-377	1819	7	7	U/Pb	Cooling	Titanite	TIMS	581845	6093108	Brownell Lake Pluton	(McNicoll et al., 1992)
PCA-8822-375	1830	10	10	U/Pb	Cooling	Titanite	TIMS	583595	6099833	Carroll Lake pluton	(McNicoll et al., 1992)
PCA-8822-376	1827	1	1	U/Pb	Detrital	Zircon	TIMS	574295	6094033	Wapawekka Lake Formation	(McNicoll et al., 1992)
PCA-8822-376	1848	1	1	U/Pb	Detrital	Zircon	TIMS	574295	6094033	Wapawekka Lake Formation	(McNicoll et al., 1992)
PCA-8822-376	1852	23	23	U/Pb	Detrital	Zircon	TIMS	574295	6094033	Wapawekka Lake Formation	(McNicoll et al., 1992)
PCA-8822-376	1856	2	2	U/Pb	Detrital	Zircon	TIMS	574295	6094033	Wapawekka Lake Formation	(McNicoll et al., 1992)
PCA-8822-376	1863	6	6	U/Pb	Detrital	Zircon	TIMS	574295	6094033	Wapawekka Lake Formation	(McNicoll et al., 1992)
PCA-8822-376	1864	2	2	U/Pb	Detrital	Zircon	TIMS	574295	6094033	Wapawekka Lake Formation	(McNicoll et al., 1992)
PCA-8822-376	1868	2	2	U/Pb	Detrital	Zircon	TIMS	574295	6094033	Wapawekka Lake Formation	(McNicoll et al., 1992)
PCA-8822-376	1868	2	2	U/Pb	Detrital	Zircon	TIMS	574295	6094033	Wapawekka Lake Formation	(McNicoll et al., 1992)
PCA-8822-376	1876	2	2	U/Pb	Detrital	Zircon	TIMS	574295	6094033	Wapawekka Lake Formation	(McNicoll et al., 1992)
PCA-8822-376	1889	2	2	U/Pb	Detrital	Zircon	TIMS	574295	6094033	Wapawekka Lake Formation	(McNicoll et al., 1992)
PCA-8822-378	1832	9	3	U/Pb	Igneous Crystallization	Zircon	TIMS	570349	6095943	Maynard Creek granodiorite	(McNicoll et al., 1992)
PCA-8822-377	1831	9	9	U/Pb	Igneous Crystallization	Zircon	TIMS	581845	6093108	Brownell Lake Pluton	(McNicoll et al., 1992)

* Ages reported from the Saskatchewan Ministry of the Economy, Geological Atlas of Saskatchewan. (http://www.infomaps.gov.sk.ca/website/sir_geological_atlas/viewer.htm)

SAMPLE #	AGE	ERROR +	ERROR -	SYSTEM	INTERPRETED AGE	GEOCHRONOMETER	TECHNIQUE	EASTING	NORTHING	NAME	REFERENCE
PCA-8822-375	1834	3	3	U/Pb	Igneous Crystallization	Zircon	TIMS	583595	6099833	Carroll Lake pluton	(McNicoll et al., 1992)
9022-94	1834	5	5	U/Pb	Igneous Crystallization	Zircon	TIMS	571340	6095942	Maynard Creek porphyry	(McNicoll et al., 1992)
9022-92	1838	2	2	U/Pb	Igneous Crystallization	Zircon	TIMS	589138	6169886	Pine Lake meta-rhyolite	(McNicoll et al., 1992)
9022-94	1864	2	2	U/Pb	Xenocryst	Zircon	TIMS	571340	6095942	Maynard Creek porphyry	(McNicoll et al., 1992)
8722-439	1766	1	1	U/Pb	Detrital	Zircon	TIMS	612315	6158605	Ourom Lake meta-arkose	Delaney et al., 1988)
8722-439	1848	1	1	U/Pb	Detrital	Zircon	TIMS	612315	6158605	Ourom Lake meta-arkose	Delaney et al., 1988)
8722-439	1848	2	2	U/Pb	Detrital	Zircon	TIMS	612315	6158605	Ourom Lake meta-arkose	Delaney et al., 1988)
8722-439	1850	2	2	U/Pb	Detrital	Zircon	TIMS	612315	6158605	Ourom Lake meta-arkose	Delaney et al., 1988)
8722-439	1853	2	2	U/Pb	Detrital	Zircon	TIMS	612315	6158605	Ourom Lake meta-arkose	Delaney et al., 1988)
8722-439	1860	9	9	U/Pb	Detrital	Zircon	TIMS	612315	6158605	Ourom Lake meta-arkose	Delaney et al., 1988)
8722-439	1861	2	2	U/Pb	Detrital	Zircon	TIMS	612315	6158605	Ourom Lake meta-arkose	Delaney et al., 1988)
8722-439	1862	2	2	U/Pb	Detrital	Zircon	TIMS	612315	6158605	Ourom Lake meta-arkose	Delaney et al., 1988)
8722-438	1850	1	2	U/Pb	Igneous Crystallization	Zircon	TIMS	607668	6154605	Wood Lake granodiorite	Delaney et al., 1988)
8822-378	1825	5	5	U/Pb	cooling age of pluton	titanite		570637	6095015	Maynard Creek granodiorite	(McNicoll et al., 1992)
8822-377	1819	7	7	U/Pb	Cooling age of pluton	titanite		581757	6093155	Brownell Lake Pluton	(McNicoll et al., 1992)
8822-378	1832	9	3	U/Pb	crystallization age of pluton	zircon		570637	6095015	Maynard Creek granodiorite	(McNicoll et al., 1992)
8822-377	1831	9	9	U/Pb	crystallization age of pluton	zircon		581757	6093155	Brownell Lake Pluton	(McNicoll et al., 1992)
W Santoy felsite	1882	4	4	Pb-evap	Igneous Crystallization	Zircon	Zircon Evaporation	599020	6170846	West Santoy Felsite	(Durocher et al., 1993)
W Santoy dyke	1870	7	7	Pb-evap	Igneous Crystallization	Zircon	Zircon Evaporation	599001	6170586	West Santoy Felsic Dyke	(Durocher et al., 1993)
W Santoy diorite	1886	5	5	Pb-evap	Igneous Crystallization	Zircon	Zircon Evaporation	596419	6171536	West Santoy Diorite	(Durocher et al., 1993)
Santoy Zone 6	1857	3	3	Pb-evap	Igneous Crystallization	Zircon	Zircon Evaporation	594633	6170636	Santoy Zone 6 Felsite	(Durocher et al., 1993)
Santoy Zone 3	1727	11	11	Pb-evap	Igneous Crystallization	Zircon	Zircon Evaporation	595795	6171906	Santoy Zone 3 pegmatite	(Durocher et al., 1993)
8930-GC2	1760	0	0	U/Pb	Igneous Crystallization	Zircon	TIMS	580464	6124801	Lueder Lake Batholith Aplite	(Delaney et al., 1990)
8930-GC2	1848	13	13	U/Pb	Igneous Crystallization	Zircon	TIMS	580464	6124801	Lueder Lake Batholith Aplite	(Delaney et al., 1990)
8930-GC1	1866	3	3	U/Pb	Igneous Crystallization	Zircon	TIMS	583782	6123461	Sadler Lake Rhyolite	(Delaney et al., 1990)
9030-02	1837	0	0	U/Pb	Detrital	Zircon	TIMS	571544	6134807	Sadler Lake psammopelite	(Heaman et al., 1991)
8930-GC2	1760	0	0	U/Pb	Igneous Crystallization	Zircon	TIMS	580464	6124801	Lueder Lake Batholith Aplite	(Heaman et al., 1991)
8930-GC2	1848	13	13	U/Pb	Igneous Crystallization	Zircon	TIMS	580464	6124801	Lueder Lake Batholith Aplite	(Heaman et al., 1991)
8930-GC1	1866	3	3	U/Pb	Igneous Crystallization	Zircon	TIMS	583782	6123461	Sadler Lake Rhyolite	(Heaman et al., 1991)
9030-02	1795	1	1	U/Pb	Metamorphic	Monazite	TIMS	571544	6134807	Sadler Lake psammopelite	(Heaman et al., 1991)
9030-01	1875	3	3	U/Pb	Igneous Crystallization	Zircon	TIMS	608574	6116088	Gee Lake rhyolite	(Heaman et al., 1992)
KM1001-002	1870	0	0	U/Pb	Detrital	zircon	SHRIMP	475091	6126997	Nemeiben Lake, Bell Bay	(Maxiener et al., 2012)
RM1001-5005	1838	6	6	U/Pb	Igneous Crystallization	zircon	SHRIMP	476878	6129381	Nemeiben Lake, Bell Bay	(Maxiener et al., 2012)
KA95-49	1859	10	10	U/Pb	Igneous Crystallization	Zircon	SHRIMP	644271	6194105	Kisseynew Scimitar Complex	(Ansdell and Stern, 1997)
KA95-49	1813	26	26	U/Pb	Metamorphic	Zircon	SHRIMP	644271	6194105	Kisseynew Scimitar Complex	(Ansdell and Stern, 1997)
Ourom dyke	1886	4	4	U/Pb	Inheritance	Zircon	TIMS	612623	6157907	(east) cuts Ourom Lake Group	(Heaman et al., 1999)
RM0901-9002	1864.4	2.1	2.1	U/Pb	Igneous Crystallization	Zircon	ID-TIMS	577991	6141272	Traill Bay Granodiorite	(Maxiener et al., 2010)

* Ages reported from the Saskatchewan Ministry of the Economy, Geological Atlas of Saskatchewan. (http://www.infomaps.gov.sk.ca/website/sir_geological_atlas/viewer.htm)